WWU
MÜNSTER

institut für
theoretische physik

Theoretische Physik

Dynamics of droplets on switchable pre-structured substrates

Inaugural-Dissertation
zur Erlangung des Doktorgrades
der Naturwissenschaften im Fachbereich Physik
der Mathematisch-Naturwissenschaftlichen Fakultät
der Westfälischen Wilhelms-Universität Münster

vorgelegt von

Moritz Stieneker

February 23, 2023

Dekan:	Prof. Dr. Michael Rohlfing
Erste Gutachterin:	PD. Dr. Svetlana V. Gurevich
Zweiter Gutachter:	Prof. Dr. Andreas Heuer
Tag der mündlichen Prüfung:	_____
Tag der Promotion:	_____

ABSTRACT

Liquids can form a wide variety of patterns on surfaces. To control this pattern formation, substrates on which a wettability pattern has been imprinted can be used. Meanwhile, some surface coatings can reversibly change their wettability. In this work, the influence of temporally switchable substrates on the dynamics of droplets of simple liquids is investigated using theoretical multiscale models with different complexity. In particular, it is shown that even comparatively simple models can reproduce most of the characteristics and may be suitable for practical applications.

In the first part of the thesis, the focus is on mapping the relevant parameters between a mesoscopic thin-film model and molecular dynamics simulations. To this end, the wettability parameters of the respective models are first numerically tuned in static equilibrium, because an analytical mapping of the wettability parameters from the construction of the models is not known in the literature. In the following step, the time scales have to be tuned. So far, only the magnitude of the time scales can be theoretically converted. In order to allow quantitative comparisons nevertheless, a numerical method is demonstrated, which can be easily transferred to other models. By means of the dynamics of a droplet on a switched substrate, the mapping of both microscopic and mesoscopic models is illustrated. The generality of the procedure is demonstrated by analyzing the dynamics of two coalescing droplets.

In the second part of the thesis, the droplet behavior on periodically switched homogeneous substrates is investigated. In particular, the influence of the switching frequency is in focus. In addition to molecular dynamics simulations and results of the thin-film model, the so-called molecular kinetic theory is used. This relates the contact line velocity to the deviation of the contact angle from the equilibrium contact angle and allows an analytical consideration without numerical simulations in the limiting case of small wettability differences. The comparison of the different models leads to a better understanding at which simplification level certain mechanisms no longer occur.

ZUSAMMENFASSUNG

Flüssigkeiten können unterschiedlichste Muster auf Oberflächen ausbilden. Um diese Musterbildung zu kontrollieren, können Substrate, denen ein Benetzbarkeitsmuster aufgeprägt wurde, verwendet werden. Mittlerweile gibt es einige Oberflächenbeschichtigungen, die reversibel ihre Benetzbarkeit verändern können. In dieser Arbeit wird der Einfluss von zeitlich schaltbaren Substraten auf die Dynamik von Tropfen bestehend aus einfachen Flüssigkeiten an Hand theoretischer Modelle mit unterschiedlicher Komplexität auf mehreren Skalen untersucht. Es wird dabei u.a. gezeigt, dass selbst vergleichsweise einfache Modelle die meisten Charakteristika reproduzieren können und für die praktische Anwendung geeignet sein können.

Im ersten Teil liegt der Fokus auf der Abbildung der relevanten Parameter zwischen einem mesoskopischen Dünnfilmmodell und Molekular Dynamik Simulationen. Dazu werden zunächst im statischen Äquilibrium die Benetzbarkeitsparameter der jeweiligen Modelle numerisch abgestimmt, weil eine analytische Abbildung der Benetzbarkeitsparameter aus der Konstruktion der Modelle aus der Literatur nicht bekannt ist. Im folgenden Schritt müssen die Zeitskalen abgestimmt werden. Bislang kann nur die Größenordnung der Zeitskalen theoretisch umgerechnet werden. Um quantitative Vergleiche dennoch zu ermöglichen wird ein numerisches Verfahren demonstriert, welches sich problemlos auf andere Modelle übertragen lässt. Anhand der Dynamik eines Tropfens auf einem einfach geschalteten Substrat wird die Abbildung beider Modelle veranschaulicht. Die Allgemeingültigkeit des Verfahrens wird durch die Analyse zweier koaleszierender Tropfen gezeigt.

Im zweiten Teil wird das Tropfenverhalten auf periodisch geschalteten homogenen Substraten untersucht. Insbesondere der Einfluss der Schaltfrequenz steht im Fokus. Neben Molekular Dynamik Simulationen und Ergebnissen eines Dünnfilmmodells wird die Molekular Kinetische Theorie herangezogen. Diese bringt die Kontaktliniengeschwindigkeit mit der Abweichung des Kontaktwinkels vom Gleichgewichtskontaktwinkel in Verbindung und ermöglicht im Grenzfall kleiner Benetzbarkeitsunterschiede eine analytische Betrachtung ohne numerische Simulationen. Der Vergleich der verschiedenen Modelle führt zu einem besseren Verständnis, ab welcher Vereinfachungsstufe bestimmte Mechanismen nicht mehr auftreten.

PUBLICATIONS

ARTICLES

The first two authors have contributed equally.

[1] M. Stieneker, L. Topp, S. V. Gurevich and A. Heuer. "Multiscale perspective on wetting on switchable substrates: mapping between microscopic and mesoscopic models." In: *Phys. Rev. Fluids* 8 (1 2023), p. 013902. DOI: 10.1103/PhysRevFluids.8.013902.

[2] L. Topp, M. Stieneker, S. V. Gurevich and A. Heuer. "Wetting dynamics under periodic switching on different scales: characterization and mechanisms." In: *Soft Matter* (2022). DOI: 10.1039/D2SM01023B.

TUTORIALS AND SOFTWARE

[3] M. Stieneker, S. Hartmann and S. Gurevich. *An oomph-lib interface to access pde2path problem structs*. 2021. DOI: 10.5281/zenodo.5810147.

[4] M. Stieneker and S. V. Gurevich. *Periodic orbit continuation in systems with external periodic forcing using pde2path*. 2022. DOI: 10.5281/zenodo.7071447.

[5] J. Suer, M. Stieneker, S. Gurevich and S. Hartmann. *Implementation of the thin-film equation on prestructured, switchable substrates using the oomph-lib library*. 2022. DOI: 10.5281/zenodo.5821537.

CONTENTS

1 INTRODUCTION

Historically, scientists had to develop empirical methods to approach hydrodynamic problems in the real world because knowledge of the fundamental equations was not sufficient [1]. Despite lacking theoretical modeling tools, engineering feats to control water played an important role, e. g. qanats, aqueducts and canals [2]. Today, theoretical modeling is vital for engineers and scientists, ranging from dams to microfluidic devices. The central equation in continuum hydrodynamic modeling is the Navier-Stokes equation which is based on the Euler equation for ideal liquids and gases [3, 4]. In contrast to the Euler equation, it considers viscosity. It can describe small-scale phenomena like the motion of a single bacteria or the water flow in the kitchen sink as well as large-scale phenomena like ocean currents and the jet stream in the atmosphere. The Navier-Stokes equation covers every kind of flow, from laminar to turbulent.

Approximations and simplified models are often necessary as computational power is still increasing fast but remains limited [5]. Due to the nature of turbulence being a multi-scale problem, approximations are vital [3]. However, not all modeling approaches for hydrodynamic problems are based on the Navier-Stokes equation. Namely, molecular dynamics [6, 7], lattice Boltzmann [8, 9] and kinetic Monte Carlo simulations are discrete models that incorporate the underlying materials' particle-based nature. Due to the underlying assumptions and approximations in models, each model has specific use cases. The discrete nature of molecular dynamics simulations allows to analyze the structure of molecular structures like proteins. With the help of coarse-graining, it is also capable of describing the bulk properties of fluids [10]. The lattice Boltzmann method is well suited to model fluid flow with complicated boundary conditions and multiphase interfaces [8]. With the help of stochastic transition rates between states of the underlying model system, the kinetic Monte Carlo models have been successfully applied to various diffusion and deposition problems [11]. The aforementioned applications of the methods are far from complete. However, they show the wide scope and indicate that the choice of a suitable model might not be straightforward. Choosing the right model for an application is always a balance between the level of detail required and the relevant scales one wants to describe.

The combination of models can extend the spatial and/or temporal scales without reducing the level of detail significantly. In principle,

there are no restrictions on how models can be combined. Although, in general, two approaches are used frequently. On one hand, a specific spatial subdomain can be modeled by another model. This might require a non-trivial coupling between the models. A successful implementation of such an approach can be seen in [12]. There, the spreading dynamics of drops were investigated by combining a molecular dynamics approach in the vicinity of the contact line with a continuum approach based on the Navier-Stokes equation for the main body of the drops. On the other hand, a system that contains alternating slow and fast dynamics like in a pulsed laser can benefit from a multiscale approach [13]. There, the phenomenological Haus master equation was used to bridge the slow dynamics so that the first principle model based on time-delayed equations could only be applied to temporal intervals with fast dynamics.

An inherent prerequisite for a multiscale approach based on the combination of two models is the knowledge of the boundaries of the involved models. In this thesis, the comparison between a molecular dynamics model and a continuum thin-film model is prevalent. This comparison is facilitated by a mapping between the various parameters within each model. It is demonstrated that the combination of these models is a fruitful basis for multiscale approaches for more involved topologies and/or liquid patterns. Even though the involved systems are rather simple and the complete interval of interest can be modeled with the molecular dynamics model, the savings of computational resources is significant. All the molecular dynamics computations have been performed with the help of the high-performance computing cluster PALMA. In contrast, the thin-film model simulations have been computed on ordinary desktop workstations. For parameter scans multiple workstations have been used in parallel.

For the aforementioned microfluidic devices, granular control of single droplets is necessary. Materials with varying wettability can be used to steer droplets across a surface. A rather vivid experiment was presented by Chaudhury and Whitesides [14]. They used polished silicon wafers treated with a diffusing vapor front of $Cl_3Si(CH_2)_9CH_3$ to make water run uphill. In the last century, theoretical understanding and technologies to fabricate new surfaces advanced. Today one can fabricate surfaces, which allow us to control their properties reversibly and externally, offering a vast potential to influence fluid dynamics. Ichimura, Oh and Nakagawa [15] could steer a droplet back and forth on a surface covered by a monolayer of calix[4]resorcinarene derivative with azobenzene units. The azobenzene units are photoresponsive and can change from cis- to trans-state and vice versa by illumination with light of an appropriate wavelength. The order of magnitude for the duration of the switching process is about ten seconds. Similar materi-

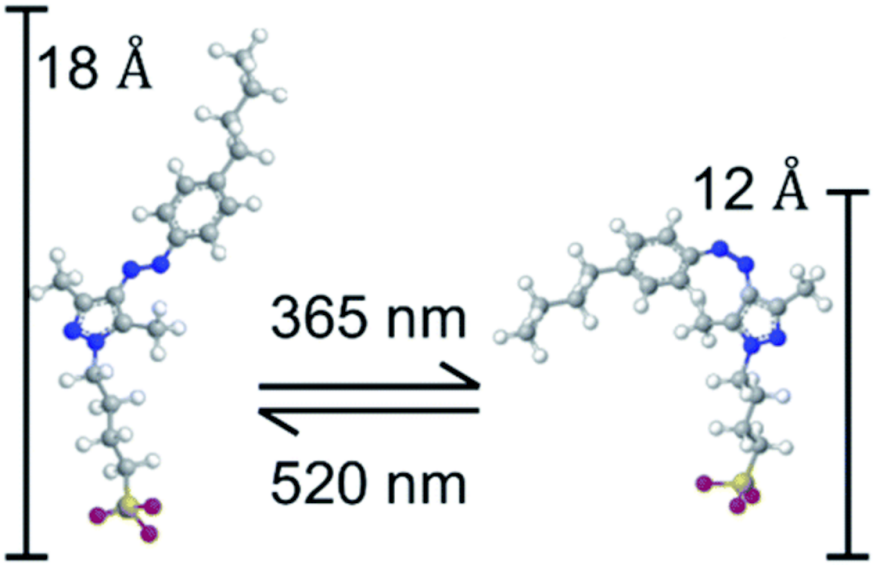

Figure 1.1: Structures of an arylazopyrazoles derivative used as a photoswitch in [21]. This surfactant allows for changes in the surface of up to $\Delta\gamma = 27 mN/m$. Reproduced from Ref. [21] with permission from the Royal Society of Chemistry.

als also show photoresponsive behavior [16–18]. To enlarge the contact angle difference between the switchable states, micro-structuring techniques can help [19, 20].

Part of the ongoing research is to reliably decouple the external stimulus for the wettability control from the current liquid pattern on a surface. For example, on an Al_2O_3 surface coated with arylazopyrazole phosphonic acids, the switching is only possible in one direction when there is a droplet on the surface. For the back direction, the droplet needs to be removed temporarily [22]. Fig. 1.1 visualizes how an arylazopyrazoles derivative changes its structure under irradiation. Inorganic materials like TiO_2 or ZnO [23–25] are another group of suitable materials that have the advantage of a large difference between the contact angles before and after switching. These materials can change from a hydrophobic to a hydrophilic state via UV radiation within minutes or hours. The other switching direction takes place on the order of weeks because the substrates have to be stored in the dark so that ambient oxygen can re-saturate the surface [23–25]. Experimental results are shown in Fig. 1.2 and demonstrate the application as an antifogging coating.

In this thesis, problems in the context of fluids on switchable substrates are analyzed with the help of multiscale analysis based on the combination of a microscopic molecular dynamics model and a thin-film model. The proposed mapping between these models enables quantitative comparisons between the models in the case of a single,

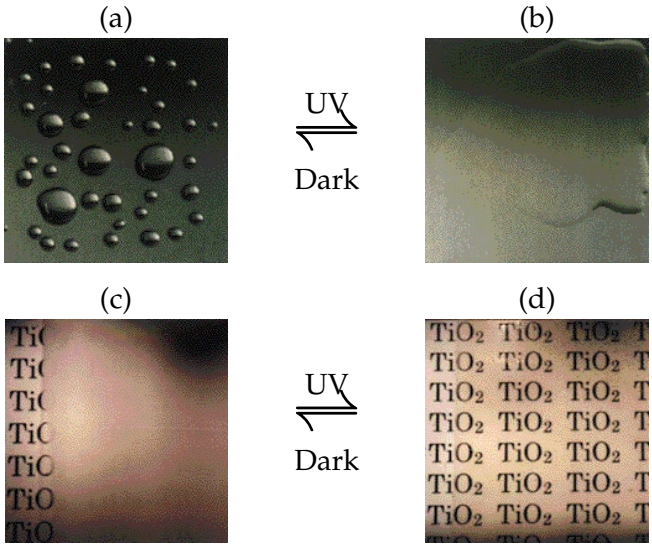

Figure 1.2: A hydrophobic TiO_2 surface (a) becomes hydrophilic under UV irradiation (b). This can be used as a surface coating to prevent the formation of fog on the surface (c) to make the text on a paper behind a coated glass visible (d). Reproduced from Ref. [23] with permission from Springer Nature.

instantaneous switch in wettability, the coalescence of two droplets and fast, periodically switched substrates. For experiments quantitative predictions are essential to successfully narrow down interesting parameter ranges. A quantitative agreement between two theoretical models is a promising step towards this goal.

The outline of this thesis is as follows: In Chapter 2 the models used throughout this thesis are explained. For the thin-film model, a particular focus is on the disjoining pressure and the mobility, which helps in understanding the incorporation of wettability into the model. Additionally, the fundamentals of the employed molecular dynamics model are explained. In such a particle-based model, the wettability needs to be accounted for differently. The required numerical methods to effectively simulate dynamic wetting with the aforementioned models are presented in Chapter 3. A focus is on the mathematical concepts behind the finite element method, which is used for the direct numerical simulations of the thin-film model.

Based on the foundation laid in Chapter 2 and Chapter 3, the mapping of the relevant parameters between a mesoscopic thin-film model and molecular dynamics simulations is explained as published in [26]. The presented approach allows mapping the wettability parameters of the respective models numerically. So far, an analytical mapping of the wettability parameters from the construction of the models is unknown in the literature. With the help of a relatively general

approach, the dynamics of the Molecular dynamics model and the thin-film model are compared for the relaxation of a single droplet and the coalescence of two droplets.
In Chapter 5, the droplet behavior on periodically switched homogeneous substrates is investigated. In particular, the influence of the switching frequency is considered. With the help of the molecular kinetic theory according to Blake and Haynes analytical predictions in the limiting case of small wettability differences are demonstrated.
Chapter 6 sums up the results and gives an outlook and possible follow-up research questions.

2 THEORY

The results presented in this thesis are based on two theoretical models: a mesoscopic thin-film (TF) and a microscopic molecular dynamics (MD) model. In this chapter, the models are introduced with a focus on the incorporation of a switchable wettability.

2.1 THIN-FILM MODEL

The governing thin-film equation is in its basic form a mesoscopic hydrodynamic description of the time evolution of height profiles $h = h(x, y, t)$ of films and drops of simple partially wetting liquids on flat solid substrates (corresponding to the two-dimensional plane (x, y)) [28–30]:

$$\partial_t h = \nabla \cdot \left(\frac{Q(h)}{\eta} \nabla [-\gamma \Delta h - \Pi(h)] \right). \tag{2.1}$$

Here, $Q(h)$ is the mobility, η the viscosity, γ the surface tension and $\Pi(h)$ the disjoining pressure. In this partial differential equation (PDE), the nabla operator is defined as $\nabla = (\partial_x, \partial_y)$ and, consequently, the Laplace operator is $\Delta = \nabla^2 = \partial_x^2 + \partial_y^2$. For the sake of simplicity, the following description is restricted to the one-dimensional case with $\nabla = \partial_x$ and $\Delta = \partial_x^2$. A detailed derivation of the thin-film equation based on the so-called lubrication approximation of the Navier-Stokes equation can be found in [30] and [31] among others. The thin-film equation (2.1) can further be derived from Onsager's variational principle if the long-wave approximation is applied and appropriate boundary conditions are used [32, 33].

The generalized pressure

$$P = -\gamma \Delta h - \Pi(h) \tag{2.2}$$

can be understood as the variation of a free energy $\mathcal{F}[h]$

$$P = \frac{\delta \mathcal{F}[h]}{\delta h} \tag{2.3}$$

with respect to the film height [28, 34–36]. As the free energy $\mathcal{F}[h]$ is a Lyapunov functional for any positive definite mobility $Q(h) \geq 0$, the equilibrium wetting state can be predicted for any mobility $Q(h)$. This is possible because the minimization of the free energy does not depend on the particular mobility form. The disjoining pressure and its influence on the dynamics are explained in details in Section 2.1.1.

Further, it is shown how substrates with a pre-structured or switchable substrate influence the disjoining pressure. Finally, the mobility's role and different mobility choices are discussed in Section 2.1.2. In addition, it is convenient to non-dimensionalize the PDE (2.1), which is presented in Section 2.1.3.

2.1.1 *Disjoining pressure*

Historically, Derjaguin could prove the existence of a disjoining pressure with experiments on thin films [37, 38]. He recognized that gradients in the disjoining pressure could lead to flow [39]. In his honor, the disjoining pressure is also called Derjaguin pressure. The disjoining pressure Π is related to the interface potential $\Phi(h)$ via

$$\Pi(h) = -\frac{\mathrm{d}\Phi(h)}{\mathrm{d}h}. \tag{2.4}$$

The interface potential $\Phi(h)$ is the liquid film's excess free energy per unit area, which vanishes in the limit of large film heights [34]. There can be a wide range of forces between surfaces and liquids contributing to the disjoining pressure [40]. In the partial wetting regime, the disjoining pressure usually contains a term related to long-ranged van der Waals forces between substrate and liquid as well as a short-ranged interaction term. The long-ranged van der Waals contribution to the disjoining pressure can be modeled by [30]

$$\Pi_{\mathrm{vdW}} = -\frac{H}{6\pi h^3}. \tag{2.5}$$

Here, H is the Hamaker constant, which can be measured to quantify van der Waals forces [41]. On the other hand, the terms related to the short-ranged forces can be modeled in various ways [30, 42–46]. Commonly, the short-ranged contribution Π_{sr} to the disjoining pressure is modeled with a polynomial ansatz [30, 42–45]

$$\Pi_{sr} \propto h^{-n} \quad \text{with} \quad n > 3 \tag{2.6}$$

or an exponential ansatz [30, 46]

$$\Pi_{sr} \propto \exp(-h). \tag{2.7}$$

In this thesis, a polynomial disjoining pressure of the form

$$\Pi(h) = \frac{B}{h^6} - \frac{A}{h^3} \tag{2.8}$$

is used with $A = H/6\pi$ and a constant B for the the short-ranged term [28, 29, 47, 48]. Depending on the coefficients A and B, different kinds of wetting regimes can be modeled using Eq. (2.8). Figure 2.1 illustrates the shape of the disjoining pressure in the different wetting regimes.

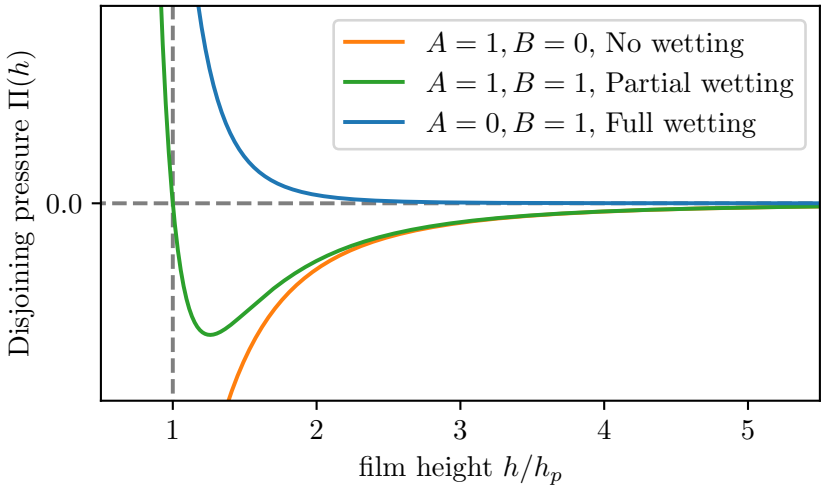

Figure 2.1: Disjoining pressures $\Pi(h)$ based on Eq. (2.8) for different wetting regimes: no wetting (orange), partial wetting (green) and full wetting (blue). The height is given in units of the precursor film height h_p, which is the film height that corresponds to the minimum of the interaction potential $\Phi(h)$ (see vertical gray dashed line).

In the partial wetting regime (cf. green curve in Fig. 2.1), the interface potential $\Phi(h)$ has a minimum at $\Pi(h_p) = 0$ leading to a precursor layer of height h_p. Consequently, there is no sharp contact line. A sharp contact line would lead to logarithmic energy dissipation through the no-slip boundary condition [49], and hence the contact line would not be able to move. Instead, a contact region exists due to the precursor layer, making moving contact lines possible. Other methods to obtain a moving contact line like introducing a slip length or a diffuse interface are outlined in [34]. Although the precursor film may appear as a mathematical artifact, it has been observed in various experiments [50–53].

Within the lubrication approximation the macroscopic equilibrium contact angle Θ_{eq} is related to the value of the interface potential $\Phi(h)$ evaluated at the precursor film height [28, 29, 31, 54] as

$$\Theta_{\mathrm{eq}} = \sqrt{\frac{-2\Phi(h_p)}{\gamma}}. \tag{2.9}$$

So far, the thin-film equation (2.1) is suitable for spatially and temporally homogeneous substrates. The disjoining pressure is the only term in Eq. (2.1) related to the interaction of the substrate and the liquid such that possible spatial and temporal inhomogeneities must be included there. In particular, Thiele and Knobloch modulated the exponential short-ranged term with a structure-function to model substrate heterogeneities and Konnur, Kargupta and Sharma varied

the long- and short-ranged terms independently based on material constants of the underlying substrate [55]. Another possibility is to modulate both interaction terms [28, 29, 47, 56, 57], which is applied here according to

$$\Pi(h,x,t) = \left(\frac{B}{h^6} - \frac{A}{h^3}\right)[1+\xi(x,t)], \tag{2.10}$$

where the function $\xi(x,t)$ can be used to model any spatial prestructure and temporal switching pattern. Note that this form does not influence the precursor film height h_p. Using Eq. (2.9) in conjunction with $h_p = \sqrt[3]{B/A}$ as well as Eq. (2.10) a macroscopic contact angle can be assigned to every position x and time t with

$$\Theta_{\mathrm{eq}}(x,t) = \sqrt{\frac{-2\Phi(h_p,x,t)}{\gamma}} = \sqrt{\frac{3A^{\frac{5}{3}}}{5\gamma B^{\frac{2}{3}}}(1+\xi(x,t))}. \tag{2.11}$$

This thesis mainly focuses on switchable substrates, which are inherently dynamic. A dynamic, time-dependent disjoining pressure $\Pi(h) = \Pi(h,t)$ means that the free energy $\mathcal{F}[h]$ is not a Lyapunov functional anymore because a Lyapunov functional no longer exists. Thus, the free energy is only guaranteed to decrease monotonously if the disjoining pressure is constant for some time. A piecewise autonomous disjoining pressure occurs when instantaneous switching is considered. This underlines the influence of the disjoining pressure on the dynamics even when it is time-dependent. In general, the main influence of the disjoining pressure stems from specifying stationary states and thus restricts possible paths in phase space.

The disjoining pressure is connected to the free energy $\mathcal{F}[h]$ via Eqs. (2.2) and (2.3). The free energy is a quantity that can be extracted from various microscopic models. In particular, Tretyakov et al. extracted the free energy from an MD model and successfully compared equilibrium states from the MD model to results from a continuum model based on the previously extracted free energy. Similar results can be obtained using density-functional theory (DFT) [59, 60]. The results from [59, 60] could be verified by a different method of extracting the disjoining pressure, namely using nudged elastic band calculations [61]. Improving other models is not the sole purpose of the free energy extraction. For example, Hughes, Thiele and Archer could link the extracted oscillatory disjoining pressure to the layered packing of molecules observable in experiments [60]. While more accurate free energies can improve mesoscopic models like the TF model shown in Eq. (2.1), the techniques to extract the free energy are not straightforward and some open questions remain, e. g. the role of the fictitious potential in DFT models [32].

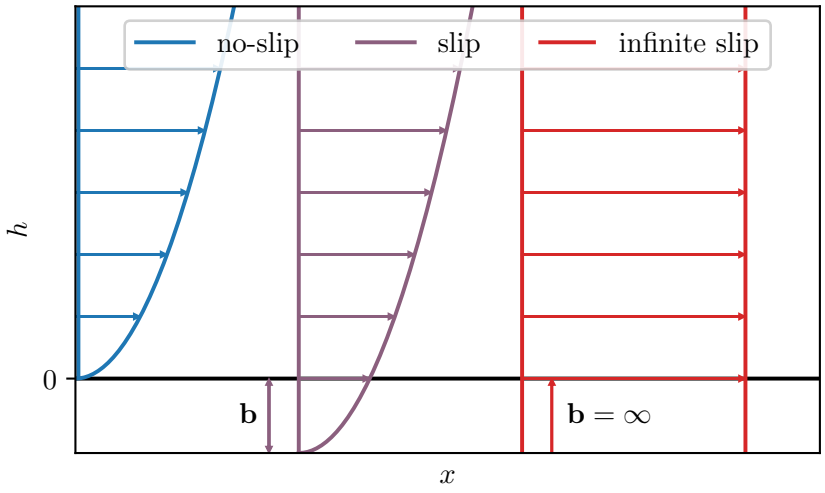

Figure 2.2: Visualization of possible boundary conditions at the substrate (black line at $h = 0$) and the corresponding slip length in different cases in the TF model. The arrows indicate the flow profile. This Figure is an adaptation of Figure 2 from [62].

2.1.2 *Mobility*

In the thin-film equation (2.1) the mobility $Q(h)$ is introduced. A no-slip boundary condition at the substrate leads to $Q(h)$ following a cubic relation [30]

$$Q(h) = \frac{1}{3}h^3. \tag{2.12}$$

As the name mobility implies, it has a decisive influence on the system dynamics. In this section, different choices for the function $Q(h)$ are discussed.

In particular, common choices for mobilities are [32, 62]

- no-slip: $Q(h) = \frac{1}{3}h^3$,
- weak-slip: $Q(h) = \frac{1}{3}h^3 + bh^2$,
- intermediate-slip: $Q(h) = bh^2$,

where the no-slip case is a special case of the weak-slip case with $b = 0$. The strong-slip case is missing from the list because this case cannot be expressed as a one-dimensional PDE like Eq. (2.1) [62]. The case of strong-slip also covers the lubrication model for free films [62]. The intermediate-slip case emerges when the order of magnitude of the slip length is between the strong and the weak-slip case. The effect of slip length on the flow profile is demonstrated in Fig. 2.2.
With constant mobility, the governing equation becomes the standard diffusion equation [32]. A combined mobility function $Q(h) = h^3 + c$ automatically switches between diffusive and convective transport

when going from the adsorption layer to a droplet or thick liquid film [32]. The influence of the constant c in such a model system was studied by Yin et al. [63]. Note that the precursor film in no-slip models can be connected to a slip length in models without a precursor film and vice versa [64].

There are indications that the mobility does not influence which transients are visited during the evolution but only the time spent in the transient states [28, 32, 63]. Honisch et al. provide visualizations showing the evolution along free energy plateaus [28]. However, these considerations on the impact of the mobility are only valid when dealing with static substrate properties. For example, imagine a substrate that changes wettability with a period T. There, the current state at the moment the substrate is switched has a significant impact on the further evolution.

For quantitative comparisons with experiments or other models, the mobility has to be sufficiently accurate if switching is involved. However, methods for extracting the mobilities from microscopic modes are so far lacking in the literature [32]. Microscopic models generally include stochastics which is an additional influence on the time scales. To differentiate what can be attributed to the mobility or stochastic effects studies on stochastic thin-film models can provide insights [65–67].

2.1.3 *Non-dimensionalization*

The complete evolution equation with the mobility from Eq. (2.12) and the disjoining pressure from Eq. (2.10) with dimensional variables reads

$$\partial_t h = \nabla \left[\frac{h^3}{3\eta} \nabla \underbrace{\left(-\gamma \Delta h - \left(\frac{B}{h^6} - \frac{A}{h^3} \right) [1 + \xi(x,t)] \right)}_{P} \right]. \tag{2.13}$$

For a systematic analysis, it is convenient to convert this equation to a non-dimensionalized form. This section follows the non-dimensionalization given in [26]. As mentioned earlier, the precursor film height h_p corresponds to the minimum interface potential or the zero of the disjoining pressure. The zero of the employed disjoining pressure is independent of the spatial and temporal modulation term $(1 + \xi(x,t))$ and is given as

$$\frac{A}{h_p^6} - \frac{B}{h_p^3} = 0 \quad \Rightarrow \quad h_p = \left(\frac{B}{A} \right)^{\frac{1}{3}}. \tag{2.14}$$

Combining Eq. (2.14) and Eq. (2.9) for the macroscopic contact angle yields the relations

$$A = \frac{5}{3}\gamma\Theta_{\mathrm{eq}}^2 h_p^2 \quad \text{and} \quad B = \frac{5}{3}\gamma\Theta_{\mathrm{eq}}^2 h_p^5 \tag{2.15}$$

for the constants A and B. Inserting these into the generalized pressure P as given in Eq. (2.2) gives

$$P = -\gamma\Delta h - \frac{5}{3}\gamma\Theta_{\mathrm{eq}}^2 h_p^2 \left(\frac{h_p^3}{h^6} - \frac{1}{h^3}\right)(1 + \xi(x,t)). \tag{2.16}$$

Then, the new scales

$$x \to x_0 \cdot \tilde{x}, \quad t \to t_0 \cdot \tilde{t}, \quad h \to h_0 \cdot \tilde{h}, \quad P \to P_0 \cdot \tilde{P} \tag{2.17}$$

are inserted into the dimensional thin-film equation (2.13). After dropping the tildes the evolution equation reads

$$\partial_t h = \nabla\left[\frac{h_0^2 t_0 P_0}{3\eta x_0^2}\, h^3 \nabla P\right], \tag{2.18}$$

$$P = -\frac{\gamma h_0}{x_0^2 P_0}\Delta h - \frac{5\gamma\Theta_{\mathrm{eq}}^2 h_p^2}{3P_0 h_0^3}\left(\frac{h_p^3}{h_0^3}\frac{1}{h^6} - \frac{1}{h^3}\right)(1 + \xi(x_0 x, t_0 t)). \tag{2.19}$$

The scales x_0, h_0, t_0 and P_0 can be chosen freely. Here, the parameter h_0 is used as a reference height, e. g. an experimentally measured droplet size. Then, the thin-film equation can be simplified by solving

$$\frac{h_0^2 t_0 P_0}{3\eta x_0^2} = 1, \tag{2.20}$$

$$\frac{\gamma h_0}{x_0^2 P_0} = 1, \tag{2.21}$$

$$\frac{5\gamma\Theta_{\mathrm{eq}}^2 h_p^2}{3P_0 h_0^3} = \frac{5}{3}\Theta_{\mathrm{eq}}^2 \chi^2, \tag{2.22}$$

where $\chi = h_p/h_0$ is introduced. Solving this system of equations for the scales eliminates most of the prefactors. Keeping the term $\frac{5}{3}\Theta_{\mathrm{eq}}$ ensures that all the spatial dimensions are scaled similarly. The solution is

$$x_0 = h_0, \quad t_0 = \frac{3\eta h_0}{\gamma}, \quad P_0 = \frac{\gamma}{h_0}. \tag{2.23}$$

With these scales, the thin-film equation can finally be written as

$$\partial_t h = \nabla\left[h^3 \nabla\left(-\Delta h - \frac{5}{3}\Theta_{\mathrm{eq}}^2 \chi^2 \left(\frac{\chi^3}{h^6} - \frac{1}{h^3}\right)(1 + \xi(x,t))\right)\right]. \tag{2.24}$$

In this form, the temporal modulation of the disjoining pressure $\xi(x,t)$ is expressed in the dimensionless units. A more detailed derivation of the non-dimensionalization is presented by Engelnkemper [31].

2.2 MOLECULAR DYNAMICS MODEL

This thesis was developed in the framework of Schwerpunktprogramm 2171 of the DFG in collaboration with the Institute of Physical Chemistry. The underlying MD simulations were performed by Leon Topp with the particle simulation toolkit HOOMD [68]. This section gives a short overview of the employed Lennard-Jones model. In the employed canonical ensemble, the particle number N, volume V and temperature T are kept constant. Thus, it is also referred to as the NVT ensemble. For temperature control, the dissipative particle dynamics thermostat is used [69, 70].

Particles interact via the Lennard-Jones potential

$$V(r_{lj}) = 4\epsilon_{lj}\left(\left(\frac{\sigma_{lj}}{r_{\mathrm{lj}}}\right)^{12} - \left(\frac{\sigma_{lj}}{r_{\mathrm{lj}}}\right)^{6}\right) \tag{2.25}$$

with the distance r_{lj} and interaction strength ϵ_{lj} between particle l and j. σ_{lj} is the mean of the two interacting particles' diameter σ_l and σ_j. Here, equally sized particles with diameter σ are used and the potential is truncated incorporating a shift at the cut-off radius $r_c = 2.5\sigma$. For the interaction strength ϵ_{lj}, the geometric mean of the self-interaction parameters is used, which yields $\epsilon_{lj} = \sqrt{\epsilon_l \epsilon_j}$.

Two types of particles are considered: Solid substrate particles (subscript s) and fluid particles on top of the substrate (subscript f). The particles' diameters of both types are assumed to be equal, i. e. $\sigma_f = \sigma_s = \sigma$. The fluid particles can either be in the liquid or gas phase. Their self-interaction strength is set to $\epsilon_f = 1$. Hence, the wettability of the surface is varied with ϵ_s, which relates to the interaction strength between fluid and solid particles ϵ_w[1]. It is possible to induce wettability patterns on surfaces by spatially varying ϵ_w. Note that ϵ_w is changed temporally for switchable substrates. Spatial and temporal variations can be combined to model switchable wettability pre-structures. To simulate $N = 4 \cdot 10^4$ fluid particles, a constant time step of $\tau = \sigma\sqrt{M/\epsilon_f}/200$ is used, where $M = 1$ is the particle mass. Each simulation setup is averaged over 50 trajectories to create sufficient statistics. A common procedure for extracting the droplet shape as applied here is to extract the density field first and determine the liquid gas interface with the help of a crossing criterion [71–73].

Here, the droplet shape possesses transversal symmetry along the z-axis (see axis locations in Fig. 2.3) . Therefore, knowing the height h

1 The subscript w stands for wettability as it is strongly linked to wettability. Note that this quantity is not *the* wettability, as wettability is not a quantifiable property.

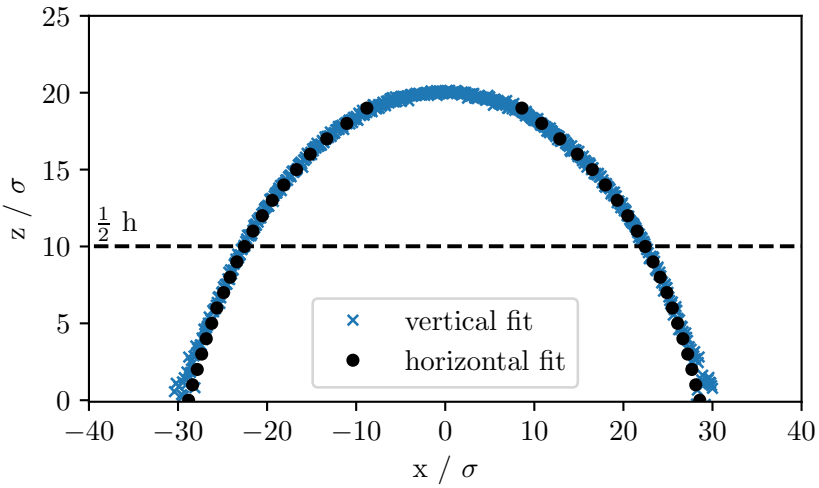

Figure 2.3: Visualization of the crossing criterion to extract the MD droplet shape from the simulation data. Blue crosses mark the interface position using the crossing criterion vertically. The black dots are based on the horizontal crossing criterion.

dependent on the position x is sufficient to describe the droplet shape. For every position x_i the density $c(z)$ is fitted with the function

$$c(z) = \frac{1}{2}(c_l + c_g) - \frac{1}{2}(c_l - c_g)\tanh\left(\frac{2(z - z_i)}{d_i}\right), \tag{2.26}$$

where c_l and c_g are the densities in the liquid and gas phases, respectively, and z_i is the z coordinate of the interface at x_i. The fit parameter d_i is the width of the interface region. The fit function from Eq. (2.26) holds for fits along the z-direction. For the orthogonal x-direction, the interface position is calculated analogously. Fig. 2.3 visualizes the differences between both procedures. In the contact region, the fit along the z-direction is less accurate than the fit along the x-direction due to fewer particles in the liquid phase along the fitted line. Similarly, the horizontal fits cannot be used to resolve droplet peaks accurately. For the horizontal fits, a bin size of 1σ was used to avoid layering effects in the contact region. A smaller bin width of 0.1σ is chosen for the vertical fits. Both procedures are combined for the final height profile $h(x)$, which is used for comparisons with the TF model (horizontal fits for $z < h_{\max}/2$ and vertical fits for $z > h_{\max}/2$).

2.2.1 *Surface tension and viscosity*

For comparisons with experiments and other models, it is advantageous to extract macroscopic quantities from MD data. To calculate the surface tension γ a slab of liquid placed in the xy-plane was simulated in its vapor phase. The dimension of the system was 50 σ x 50 σ x

100 σ and the number of fluid particles was $N = 4 \cdot 10^4$. The normal p_n and tangential part p_t of the pressure tensor were calculated for each slab of the system binned with a step of 1 σ in z-direction. Then, the surface tension can be obtained via [74]

$$\gamma = \int \mathrm{d}z \; p_n(z) - p_t(z). \tag{2.27}$$

The resulting value $\gamma = (0.477 \pm 0.005) \; \epsilon_f/\sigma^2$ is comparable to values from the literature for a similar system [71].
The shear viscosity η was calculated according to the Green-Kubo relation [75, 76]

$$\eta = \frac{V}{k_B T} \int_0^\infty \langle \; p_{\alpha\beta}(0) \cdot p_{\alpha\beta}(t) \; \rangle dt \tag{2.28}$$

where $\langle \; p_{\alpha\beta}(0) \cdot p_{\alpha\beta}(t) \; \rangle$ is the auto-correlation function (ACF) over the non-diagonal elements of the pressure tensor $p_{\alpha\beta}$. For the calculation of the pressure tensor, a simulation setup with dimensions $25\sigma \times 25\sigma \times 25\sigma$ and a fluid density of 0.785 σ^{-3} was used. This density corresponds to the density inside a droplet in the simulations. The ACF was calculated and averaged over the xy-, xz- and yz-component of the pressure tensor. For 100 trajectories the averaged ACF was obtained for 5 blocks of $4 \cdot 10^4$ time steps. Then, the value of η was obtained by averaging over the 500 integrated ACFs resulting in a value of $\eta = 2.14 \pm 0.08 \; \sqrt{M\epsilon_f}/\sigma^2$ which is comparable with values from the literature [77].

3 NUMERICAL METHODS

In the framework of this thesis, the TF model Eq. (2.1) described in Section 2.1 is solved numerically with the object-oriented, open-source finite-element library OOMPH-LIB [78]. A tutorial on how to use OOMPH-LIB for the simulations of simple liquids on possibly pre-structured and switchable substrates with a TF model is available on Zenodo [79]. In particular, the tutorial explains how to reproduce the results of Grawitter and Stark [80] with the TF model and complement their findings based on the boundary element method. Section 3.2 goes through the numerical details of the corresponding simulations.

To avoid lengthy parameter sweeps numerical path continuation can be used to search parameter space more systematically. The continuation package PDE2PATH[81] has been applied successfully for a variety of nonlinear problems [57, 82–84]. With version 2.5 of PDE2PATH, the continuation of periodic orbits in autonomous systems became possible. Since version 2.8 periodic orbit continuation is also available for non-autonomous systems so that it can be directly applied to systems with external forcing, e. g. a film described by Eq. (2.1) on a switchable substrate. The basics of the tutorial [85] looking at such a system are explained in Section 3.3. PDE2PATH is implemented in MATLAB [86] and consequently makes use of MATLAB structs to store data. With the help of the MATLAB Engine API available since version R2018b, an interface to extract PDE2PATH data from a MATLAB struct and start direct numerical simulations with OOMPH-LIB was realized and is available on Zenodo [87]. The numerical backbone for OOMPH-LIB and PDE2PATH is the finite element method (FEM) which is explained in the following.

3.1 FINITE ELEMENT METHOD

Analytical solutions to the thin-film model as represented by Eq. (2.1) are only possible in very limited edge cases. For disjoining pressures with no temporal and spatial dependence $\Pi = \Pi(h)$ a homogeneous film $h(x,t) = h_0$ is a stationary solution. In the case of a vanishing disjoining pressure $\Pi(h) = 0$, i. e. a system solely under the influence of the Laplace pressure, a parabolic profile is a stationary solution because it fulfills

$$-\gamma Q(h)\frac{\partial^3 h}{\partial x^3} = 0. \tag{3.1}$$

This equation results from a single integration of Eq. (2.1). The integration constant corresponds to a net flux into or out of the domain, which is zero for the considered horizontal domains. To go beyond these stationary edge cases numerical techniques are required. Note that these edge cases might be relevant as easy-to-exploit initial conditions to apply the toolkit of continuation and bifurcation analysis. However, continuation software require numerical techniques as well, e.g. PDE2PATH implements the FEM.

This section explains the FEM with a particular focus on the specific implementation in OOMPH-LIB[1]. A great advantage of the FEM is the flexibility to represent different topologies and boundary conditions [88]. In many engineering disciplines, FEM has become a standard tool. This is also due to the fact that it is integrated into many commercial CAD programs to accelerate virtual product development [88]. Exemplary applications are linear elastomechanics, nonlinear strength calculation or heat conduction [88]. The focus of the library OOMPH-LIB is on solving spatially extended physical problems. Many such problems benefit from the weaker mathematical requirements for the solutions obtained with the FEM [89, 90]. This is due to the weak formulation, which is explained in Section 3.1.1. A detailed introduction to the FEM from a mathematical perspective can be found in [91, 92]. For readers more interested in the implementation and comparisons to similar methods like spectral methods Ref. [93] is an appropriate resource. The engineering perspective is highlighted in [88]. An early standard work for the FEM is [90]. The different perspectives on the topic were combined to form an introduction aimed at physicists.

3.1.1 *Weak formulation*

The weak formulation plays an essential role in the FEM. It can be used for PDEs of second order. However, PDEs of higher order can be reformulated easily as systems of second order PDEs by introducing additional auxiliary variables. Here, the central equations are demonstrated with the help of the TF equation (2.1). Note that the FEM is only used to discretize the spatial part of a PDE. For the temporal integration, any implicit time stepping scheme can be used. First, the PDE (2.1) is transformed into the residual form

$$\mathcal{R}(x, h(x)) = \nabla \cdot \left(\frac{Q(h)}{\eta} \nabla [-\gamma \Delta h - \Pi(h)] \right) - \partial_t h = 0. \tag{3.2}$$

Explicit dependencies of $\mathcal{R}(x, h(x))$ on partial derivatives are not given to make the equations clearer. The position x can principally be a

1 OOMPH-LIB provides a short introduction to the FEM paired with implementation specifics on the website `https://oomph-lib.github.io/oomph-lib/doc/intro/html/index.html`, last retrieved February 3, 2023.

vector quantity. For the conceptual understanding, a one-dimensional problem is sufficient and particularly the visualizations benefit. A strong solution to the problem is a function $h(x)$ which satisfies

$$\mathcal{R}(x, h(x)) = 0 \quad \forall x \in D \quad \text{and} \quad h|_{\partial D} = g, \tag{3.3}$$

for a given domain D and its boundary ∂D. Here, Dirichlet boundary conditions are assumed. Neumann boundary conditions $\partial_x h|_{\partial D} = g$ or periodic boundary conditions are also conceivable. Boundary conditions for variational problems are explained in detail in [91]. The function $h_w(x)$ is called a weak solution if the boundary condition

$$h_w|_{\partial D} = g \tag{3.4}$$

is satisfied and the so-called weighted residual

$$r = \int_D R(x, h_w(x)) \phi^{test} \mathrm{d}x \tag{3.5}$$

vanishes for any test function ϕ^{test} that satisfies the boundary condition

$$\phi^{test}|_{\partial D} = 0. \tag{3.6}$$

While it may seem that the weak solution $h_w(x)$ solves the problem only in an averaged sense. It should be emphasized that the expression Eq. (3.5) however, must hold for any test function. Fig. 3.1 (a) shows a test function ϕ^{test} that would yield a vanishing residual for the given residual function $\mathcal{R}(x, h_w(x))$. In Fig. 3.1 (b), however, it is demonstrated how to construct a test function so that the residual no longer vanishes if $\mathcal{R}(x, h_w(x))$ deviates from zero. In the example in Fig. 3.1 (b) the residual function $\mathcal{R}(x, h_w(x))$ is only nonzero in two subdomains D_1 and D_2. The shown test function ϕ^{test} would be enough to determine that $h_w(x, t)$ cannot be a weak solution. This is not a rigorous mathematical proof that the weak and the strong solution coincide if a strong solution exists. Such a proof can be found in [91, 92] among others. Figure 3.1 only provides an intuitive access to the concept of the weak formulation.

3.1.2 *Method of mean weighted residuals*

The method of mean weighted residuals is an umbrella term for many methods with the aim to minimize some residual function $\mathcal{R}(x, h(x))$ [93]. Such methods allow the approximation of solutions to variational problems by transforming a continuous, variational problem into a discrete problem. The first step is to split the weak solution into

$$h_w(x) = h_p(x) + h_h(x), \tag{3.7}$$

where $h_h(x, t)$ has to satisfy the homogeneous boundary condition

$$h_h(x)|_{\partial D} = 0 \tag{3.8}$$

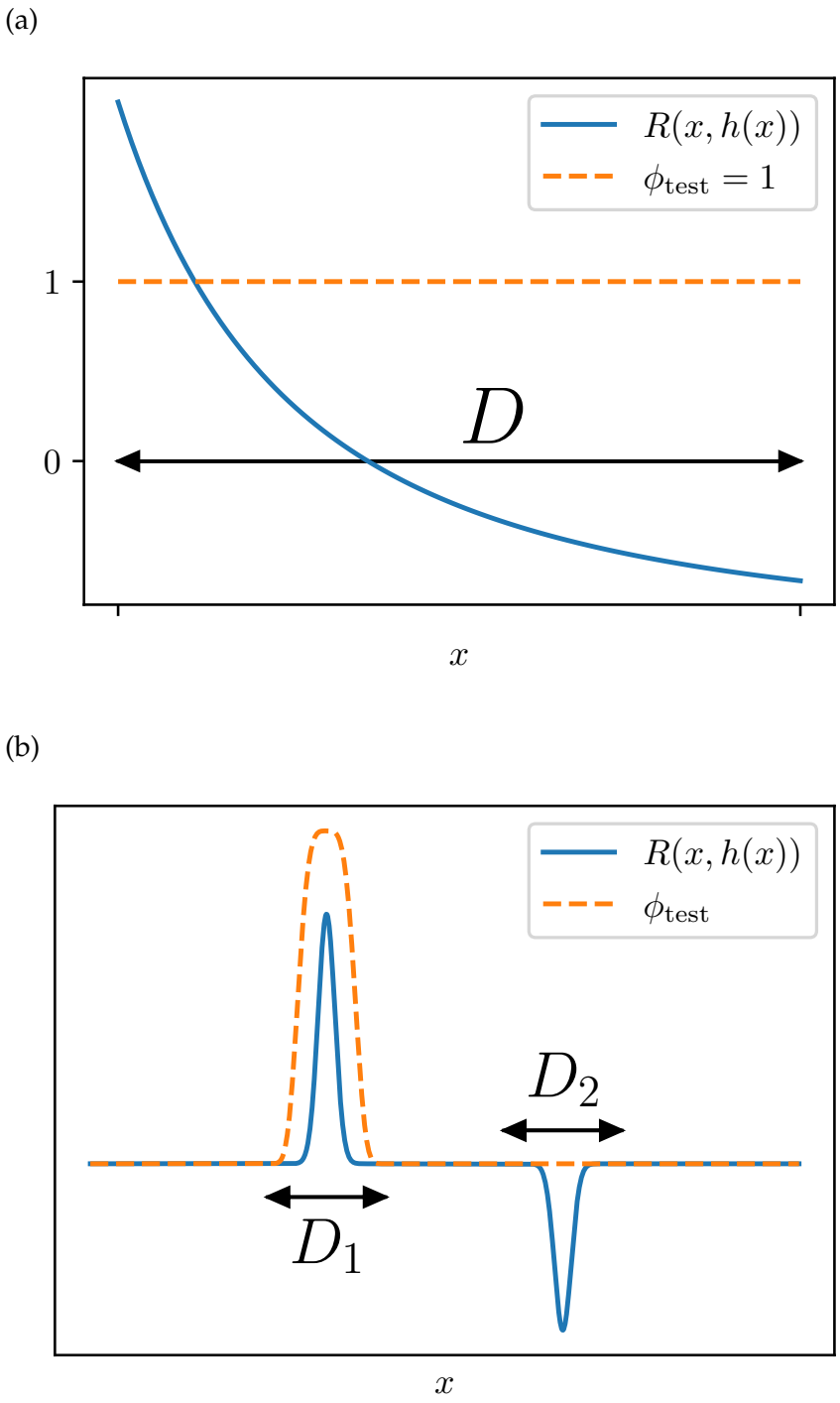

Figure 3.1: a) An example of a residual function $\mathcal{R}(x, h_c(x))$ based on a solution candidate $h_c(x)$ which would yield a vanishing residual according to Eq. (3.5) for the constant test function $\phi^{test} = 1$. For the sake of the example the requirement Eq. (3.6) is neglected here. (b) Example of a constructed test function ϕ^{test} which yields a nonzero residual for a residual function $\mathcal{R}(x, h_c(x))$ which is only nonzero in the two subdomains D_1 and D_2.

and $h_p(x,t)$ is an arbitrary function that needs to satisfy the Dirichlet boundary conditions

$$h_p(x)|_{\partial D} = g. \tag{3.9}$$

analogously to the classical problem in Eq. (3.3). Then $h_w(x)$ can be expanded according to

$$h_w(x) = h_p(x) + \sum_{j=1}^{\infty} H_j \psi_j(x). \tag{3.10}$$

into a complete basis $\{\psi_j\}$ of the underlying function space $\mathcal{H}_0$. The properties of adequate function spaces are discussed in Section 3.1.4 so that their definitions do not distract from the main concept of the method of mean weighted residuals. The factors H_j in Eq. (3.10) are the evolution coefficients. The choice of the basis functions $\{\psi_j\}$ is free in general. The expression (3.10) can be inserted into Eq. (3.5), which results in the condition

$$r = \int_D R\left(x, h_p(x) + \sum_{j=1}^{\infty} H_j \psi_j(x)\right) \phi^{test} \mathrm{d}x = 0. \tag{3.11}$$

Since the functions $\psi_j(x)$ form a complete basis, the test functions ϕ^{test} can also be expanded into the same basis according to

$$\phi^{test}(x) = \sum_{k=1}^{\infty} \Phi_k \psi_k(x). \tag{3.12}$$

Thus, the condition that the residual must vanish for any test function becomes the condition that the residual must vanish for all possible evolution coefficients Φ_k. If the same basis is used for the solution $h_w(x)$ and the test function ϕ^{test}, it is usually referred to as a Galerkin method [93]. Note that the name Galerkin method is occasionally used synonymously for the more general method of mean weighted residuals. Substituting ϕ^{test} by the evolution Eq. (3.12) in Eq. (3.11) gives

$$r = \sum_{k=1}^{\infty} \Phi_k r_k(H_1, H_2, H_3, \dots) = 0 \tag{3.13}$$

with

$$r_k(H_1, H_2, H_3, \dots) = \int_D R\left(x, h_p(x) + \sum_{j=1}^{\infty} H_j \psi_j(x)\right) \Phi_k \mathrm{d}x. \tag{3.14}$$

In practice, the expansion into the basis functions is stopped after N terms. The N unknown coefficients can then be determined via the algebraic equations

$$r_k(H_1, H_2, H_3, \dots, H_N) = 0 \quad \text{with} \quad k = 1, 2, \dots, N. \tag{3.15}$$

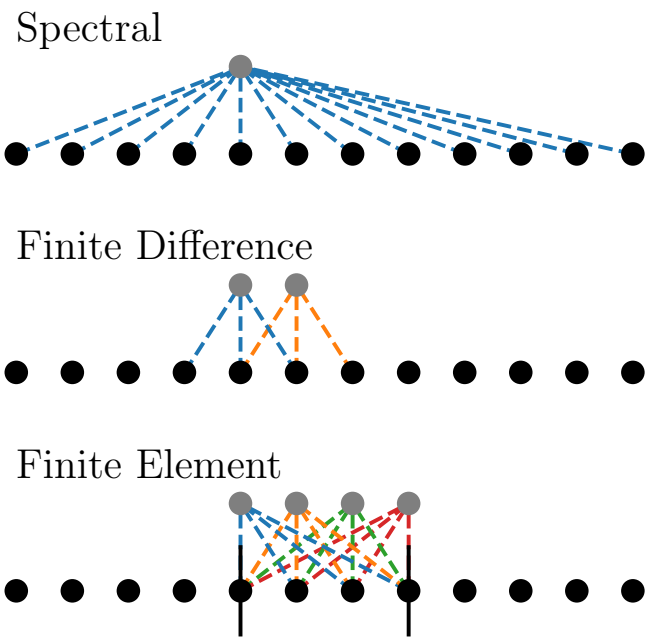

Figure 3.2: Visualization of how different methods approximate derivatives. Spectral methods use high-order polynomials or trigonometric polynomials for the whole domain, finite difference methods use multiple overlapping low-order polynomials and finite element methods use polynomials that overlap only on a subdomain. Such a subdomain is often referred to as an element and gave the method its name. Boundary nodes are part of more than one element and facilitate the coupling between elements. This figure is based on a similar figure in [93].

The convergence to the exact solution for $N \to \infty$ needs to be proved for the choice of basis functions. Mathematically rigorous proofs can be found in [92].
There are many methods relying on the method of mean weighted residuals. Figure 3.2 visualizes how the derivative at a certain node depends on other nodes for spectral methods, the finite difference method and the FEM. Spectral methods employ high-order polynomials or trigonometric polynomials like Chebyshev polynomials [93]. In the case of finite differences, delta functions are used as basis functions [94]. In the case of the FEM, the basis functions are localized on certain subdomains which led to its denotation.

3.1.3 *Implementation of the thin-film equation in oomph-lib*

In principle, the weak formulation and the Galerkin method can be applied to PDEs of arbitrary order. This could require additional constraints for the test and basis functions as well as additional boundary conditions [91]. However, it is always possible to reduce a higher-order PDE to a system of equations of lower order. In the case of the TF equation, the weak formulation of the system of equations on a one-dimensional domain D can be written as

$$\mathcal{R}_1(x, h_w, u_w) = \int_D \left[\partial_x \left(\frac{Q(h_w)}{\eta} \partial_x u_w \right) - \partial_t h_w \right] \phi_2^{test} \, \mathrm{d}x, \tag{3.16}$$

$$\mathcal{R}_2(x, h_w, u_w) = \int_D \left[-\gamma \partial_x^2 h - \Pi(x, t, h_w) - u_w \right] \phi_2^{test} \, \mathrm{d}x. \tag{3.17}$$

Here, the variable u_w is defined via Eq. (3.17). In this special case, it corresponds to the generalized pressure according to Eq. (2.2). In general, a physical interpretation of such a helper variable is not required.
With the help of integration by parts, the order of the highest derivative can be reduced by one. Integration by parts yields

$$\begin{aligned} \mathcal{R}_1 = \int_D \left[-\frac{Q(h_w)}{\eta} (\partial_x u_w) \partial_x \phi_1^{test} - \partial_t h_w \phi_1^{test} \right] \mathrm{d}x \\ + \frac{Q(h_w)}{\eta} (\partial_x u_w) \phi_1^{test} \Big|_{\partial D}, \end{aligned} \tag{3.18}$$

$$\begin{aligned} \mathcal{R}_2 = \int_D \left[\gamma (\partial_x h_w) \partial_x \phi_2^{test} - \left(\Pi(x, t, h_w) + u_w \right) \phi_2^{test} \right] \mathrm{d}x \\ - (\partial_x h_w) \phi_2^{test} \Big|_{\partial D}. \end{aligned} \tag{3.19}$$

The residual boundary terms of the partial integration in Eqs. (3.16) and (3.18) vanish due to Eq. (3.6). Without the constraint (3.6) the homogeneous Neumann boundary condition $\partial_x h_w = 0|_{\partial D}$ and $\partial_x u_w = 0|_{\partial D}$ would have been enforced implicitly.

To apply the Galerkin method h_w and u_w need to be expanded into basis functions according to

$$h_w(x) = \sum_{j=1}^{N} H_j \psi_j(x) \quad \text{and} \quad u_w(x) = \sum_{l=1}^{N} U_l \psi_l(x) \tag{3.20}$$

with the expansion coefficients H_j and U_l for the finite number of basis functions N. In combination with the expansion of the test functions ϕ^{test} according to Eq. (3.12), this leads to the following $2N$ algebraic equations for the unknown coefficients

$$r_k^{(1)} = \sum_{l=1}^{N} \int_D \left[-\frac{1}{\eta} Q\left(\sum_{j=1}^{N} H_j \psi_j(x) \right) \left(\partial_x U_l \psi_l(x) \right) \partial_x \psi_k - \partial_t H_l \psi_l(x) \psi_k \right] \mathrm{d}x, \tag{3.21}$$

$$r_k^{(2)} = \sum_{l=1}^{N} \int_D \left[\gamma \left(\partial_x H_l \psi_l(x) \right) \partial_x \psi_k - \left(\Pi(x, t, \sum_{j=1}^{N} H_j \psi_j(x)) + U_l \psi_l(x) \right) \psi_k \right] \mathrm{d}x. \tag{3.22}$$

This might seem like a tedious calculation as many integrals of the form

$$\int_D \psi_l \psi_k \mathrm{d}x \quad \text{or} \quad \int_D (\partial_x \psi_l)(\partial_x \psi_k) \mathrm{d}x \tag{3.23}$$

have to be computed. However, these terms are symmetric because test and basis functions are the same and the integration by parts eliminated asymmetric terms of the form $\psi_l \partial_x^2 \psi_k$. For linear test and basis functions the integration can be computed in constant time using Gaussian quadrature [92]. Additionally, the basis functions are localized, i. e. for most choices of l and k the integral vanishes. This leads to sparse matrices that can be solved faster than full matrices. The localization allows the nonlinearities introduced by the mobility Q and the disjoining pressure Π to be treated with the approximation that the nonlinearities only act on the coefficients, i. e.

$$Q(h_w) = h_w^3 = \left(\sum_{j=1}^{N} H_j \psi_j(x) \right)^3 \approx \sum_{j=1}^{N} H_j^3 \psi_j(x). \tag{3.24}$$

The linear system is solved using a direct numerical solver. Note that OOMPH-LIB provides an interface to use an arbitrary linear solver.

3.1.4 *Shape functions and function spaces*

Previously, the mathematical details were skipped. Here, the most important details that should keep a physicist from inappropriate usage of the FEM are clarified. One of the previous implicit assumptions in the previous sections was that the occurring integrals have to exist. This imposes restrictions on the function spaces suitable for the test and basis functions. The integrals in Eqs. (3.21) and (3.22) are finite and well-behaved if the test and basis functions are restricted to functions whose zeroth and first derivative are square-integrable over the domain D. The associated function space is usually denoted by $\mathcal{H}^1(D)$, which belongs to the Sobolev spaces $\mathcal{H}^i(D)$. The space $\mathcal{H}^i(D)$ refers to all the functions where all derivatives from zeroth to i-th

order are square-integrable over the domain D. Mathematically, this can be expressed as

$$\phi(x) \in \mathcal{H}^1(D) \quad \Leftrightarrow \quad \int_D \left(\phi(x)^2 + \left(\frac{\partial \phi(x)}{\partial x} \right)^2 \right) \mathrm{d}x < \infty, \tag{3.25}$$

$$\phi(x) \in \mathcal{H}^i(D) \quad \Leftrightarrow \quad \int_D \left(\phi(x)^2 + \sum_{k=1}^{i} \left(\frac{\partial^k \phi(x)}{\partial x^k} \right)^2 \right) \mathrm{d}x < \infty. \tag{3.26}$$

For $x \in \mathcal{R}^n$, the partial derivative in Eq. (3.25) needs to be substituted by the sum over the square of all partial derivatives $\sum_{l=1}^{n} \left(\partial_{x_l} \phi(x) \right)^2$. In some cases, it can be advantageous if the test functions vanish on the boundary ∂D. This function space is denoted $H_0^i(D)$ and is a subset of $H^i(D)$. For Dirichlet boundary conditions, this helps boundary terms from partial integrations to vanish. In general, the choice of the underlying functions space is problem dependent.
For the problem at hand, the TF equation, $H^1(D)$ is the function space of choice. This allows piecewise linear functions as the test and basis functions. Figure 3.3 visualizes hat functions on a one-dimensional domain. In the example, all elements consist of two nodes except for element 2. There, the resolution of the mesh is finer to demonstrate the concept of mesh adaption, i. e. it is possible to increase the resolution locally. The refinement is usually automated based on an error estimator. The default error estimator in OOMPH-LIB is the Z2 error estimation. This is based on the idea that the flux is discontinuous due to the discretization. By comparing the magnitude of the discontinuity to the difference to an improved estimation for the flux, which is calculated patch-wise, the error can be estimated[2] [78].
For hat functions, the coefficients in Eq. (3.20) can directly be interpreted as the solution functions value at the node and piecewise linear interpolation in between nodes is directly given. Additionally, the function $h_p(x)$ defined in Eq. (3.7) which has to fulfill the boundary condition $h_p|_{\partial D} = g$ is trivially defined via

$$h_p(x) = g\psi_1(x) + g\psi_N(x) \tag{3.27}$$

in the one-dimensional case. It can also be proven that the discretized solution converges to the continuous solution for $N \to \infty$ [91]. Instead of increasing the mesh resolution higher-order basis functions can also be used to increase the accuracy. This would directly provide higher-order interpolation between the nodes as an additional benefit. The example in Fig. 3.4 demonstrates that the FEM can be used for arbitrary domain shapes. To keep the error consistent over the whole domain the automatic mesh adaption can be applied. Figure 3.4 shows

2 A detailed explanation for the error estimation can be found at `https://oomph-lib.github.io/oomph-lib/doc/the_data_structure/html/classoomph_1_1Z2ErrorEstimator.html`, last retrieved February 3, 2023.

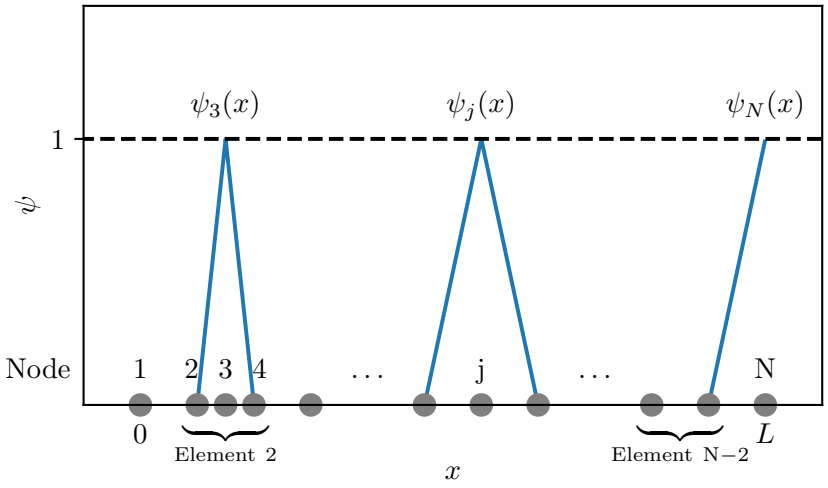

Figure 3.3: Piecewise linear base functions on a one-dimensional mesh with a spatially refined second element. Except for the refined element, all elements consist of two nodes.

that the resolution along the boundaries and especially along kinks in the boundary needs to be increased to keep the error margin consistent. On 3D domains, tetrahedral elements are the common elements but parallelepipeds and prisms are possible as well [91]. In general, any shape is possible as long as the union of all elements corresponds to the domain [92].

3.2 OOMPH-LIB

OOMPH-LIB is a C++ library that can be compiled as a python module with the help of BOOST.PYTHON. The benefits for reproducibility of doing so are explained in Appendix A along with other simple means to improve reproducibility. OOMPH-LIB is based on the finite element method as explained in the previous section. For the time stepping a a second-order backwards differentiation method (BDF2) is employed. Here, often one-dimensional domains are considered. However, the source code referenced in tutorials or supplementary material of the publications discussed in Chapters 4 and 5 is prepared for two-dimensional domains.
There is no fixed spatial resolution used for the simulations. If spatial differentiation of order 1 or 2 is required in the analysis of the solution, the minimum resolution was 164 elements per spatial unit. If no differentiation is needed, spatial resolution can be reduced by an order of magnitude. For all simulations, an adaptive time step was used.
Often a well-defined equilibrium state is required as an initial state. Such an equilibrium state can be achieved by simulating with an adaptive time step until a certain time step threshold is reached.

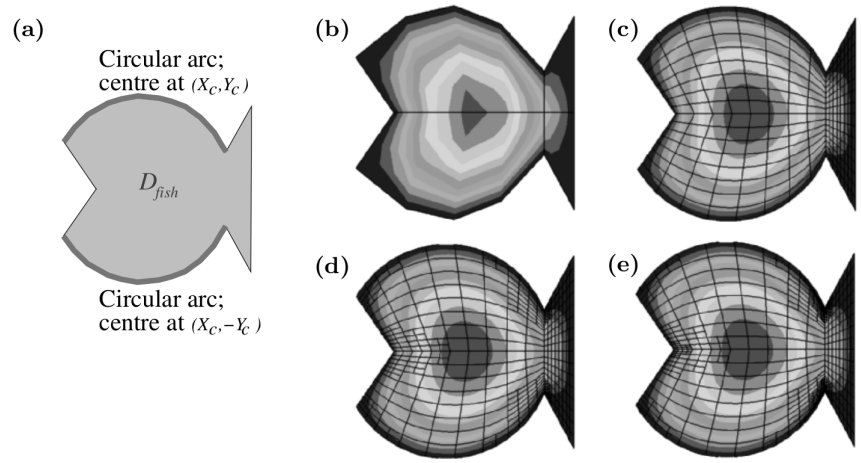

Figure 3.4: Solution of a 2D Poisson equation in a fish-shaped domain. Figure (a) shows the problem sketch; Figs. (b)-(e) show contours of the computed solution, obtained on the meshes that are generated by OOMPH-LIB's automatic mesh adaption procedures. This figure is a reprint from [78] with permission from Springer Nature.

Naturally, for periodically switched substrates the simulation would continue infinitely in general. Hence, the equilibration is performed on a substrate with a constant wettability pre-structure. This time is then defined as $t = 0$.

3.3 CONTINUATION OF PERIODIC ORBITS

The full source code to reproduce the proof of concept for the method demonstrated here is available on Zenodo [85]. It is shown that PDE2PATH can be used to start the continuation of an arbitrary periodic orbit in non-autonomous systems, where the periodicity is introduced through the non-autonomous terms. The initial data can be obtained via direct numerical simulation, analytical calculation or even experimental data if the noise is low enough and the respective model system is accurate enough.
The alternative would be to start from a known steady state and introduce a new parameter λ which modulates the non-autonomous term. After a continuation from $\lambda = 0$ to $\lambda = 1$, the main continuation of interest could be started. However, there is no guarantee that such a continuation is straightforward. It is not even guaranteed that the desired solution at $\lambda = 1$ can be reached by the continuation from $\lambda = 0$.

In the demo [85], the initial data consists of plain text files for every equidistant time step. The data was extracted from a simulation of the TF model performed within OOMPH-LIB. The periodic switching was simulated for multiple periods to exclude the effects of transients. Similar to the continuation of periodic orbits arising from Hopf bifurcation

points two essential PDE2PATH functions need to be adapted when going from steady state continuation to periodic orbit continuation. First, the branch output function has to be adapted to periodic orbits. Here, it is convenient to introduce a measure with a well-defined value should the continuation reach a steady state. For a droplet on a periodically switched substrate, the difference between the maximum and minimum droplet height during a full period is a reasonable candidate, because it is zero when a stationary state is reached. The implementation in MATLAB can look as follows:

```
np = p.nu / p.nc.neq;
maximum = max(max(p.hopf.y(1:np,:)));
maximum_difference = maximum - min(max(p.hopf.y(1:np,:)));
```

Here, `np` is the number of spatial discretization points computed from the total number of discretization points `p.nu` and the number of equations `p.nc.neq`. The array `p.hopf.y` stores the system information for the complete periodic orbit. Note that the evolution equation (2.24) is of fourth order and needs to be rewritten as a system of two equations of the second order. In MATLAB the expression `max(p.hopf.y(1:np,:))` does not compute the maximum value of the complete array. Instead, it computes the maximum value columnwise. The second function needing adaption is the function providing the constraints and auxiliary conditions. A volume or mass constraint for steady state continuation implemented like

```
% Mass matrix needed for (riemann) integrals
M = p.mat.M0 / p.vol;
constraint = sum(M * h) - h0;
```

has to be rewritten such that the constraint applies to every time step and the cumulative deviation from the mean height `h0` in this case is minimized.

```
constraint = 0;
for i = 1:length(p.hopf.t)
    h = p.hopf.y(1:np, i);
    % Add difference to mean height at every time step
    constraint = constraint + (sum(M * h) - h0);
end
```

This example can be used as a guideline for extending constraints and auxiliary conditions from steady state continuation to periodic orbit continuation.

The function describing the right-hand side of the system does not need modification. The major difference to the continuation of periodic orbits in autonomous systems is the Goldstone mode in time. For autonomous systems the solution is translationally time-invariant, i. e. a translation by some time τ is still a solution. Thus, PDE2PATH

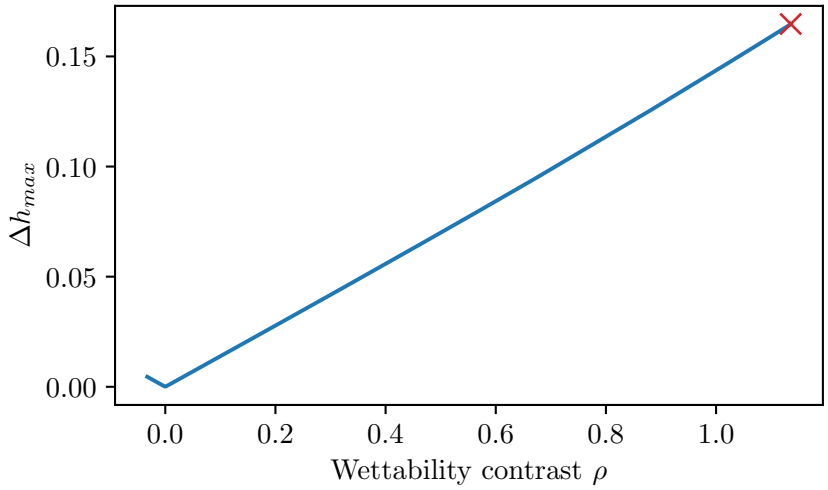

Figure 3.5: Bifurcation diagram for a continuation in the wettability contrast ρ for the TF model from Eq. (2.1) with the wettability modulation according to Eq. (3.28). The starting point for the continuation was the point marked with a red cross. Note that the initial data was created with a value of $\rho = 1$ and the red cross only corresponds to a value of $\rho > 1$ due to the initial Newton solver.

introduces a constraint to avoid continuation along this Goldstone mode. To disable this `p.hopf.pc = 0` can be set.
The resulting bifurcation diagram of an exemplary continuation run is shown in Fig. 3.5. There, the modulation of the disjoining pressure according to Eq. (2.10) is set to be

$$\xi(x,t) = \rho_0 + \rho\delta_\rho f(t)g(x) \tag{3.28}$$

with the base wettability ρ_0, the wettability contrast ρ, the wettability difference δ_ρ, a temporal modulation function $f(t)$ and a spatial modulation function $g(x)$. The parameter $\delta\rho$ is redundant and only normalizes the wettability contrast ρ to the interval $[-1,1]$. Note that the functions $f(t)$ and $g(x)$ need to be continuous and sufficiently smooth for PDE2PATH to work. Thus, instantaneous switching is impossible to realize. In this example the form

$$f(t) = \tanh\left(\frac{t-\frac{T}{4}}{s_t}\right)\tanh\left(\frac{t-\frac{3T}{4}}{s_t}\right) \tag{3.29}$$

is used with the period T and the smoothness of the transition between the extreme wettabilities s_t. In the limit $s_t \to 0$, Eq. (3.29) is a step function. Similarly, the spatial modulation

$$g(x) = \tanh\left(\frac{x+x_A}{s_x}\right)\tanh\left(\frac{x-x_A}{s_x}\right) \tag{3.30}$$

is a step function for a vanishing transition smoothness s_x. In Fig. 3.6 the wettability modulation is visualized and the parameter values are

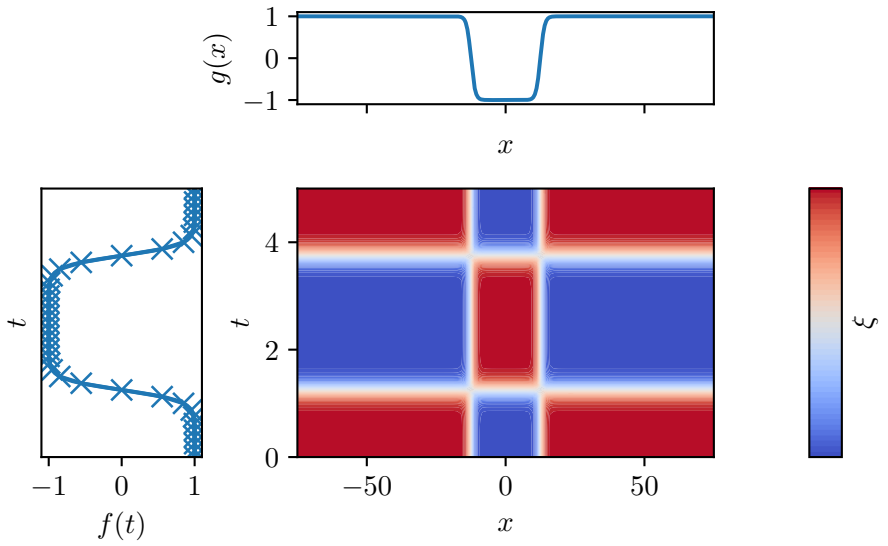

Figure 3.6: Visualisation of the wettability modulation used in [85] also shown in Eq. (3.28). Blue corresponds to a high wettability and red to a lower wettability. The temporal modulation $f(t)$ is shown on the left. The crosses mark the $n_t = 40$ discretization points used. The spatial modulation is shown at the top. There, the $n_x = 512$ equidistant discretization points are not shown. The parameters are $\rho_0 = 0.92$, $\delta_\rho = 1.04$, $x_A = 12.5$, $s_x = 1.5$, $T = 5$, $s_t = 0.2$ with the domain size $L = 150$.

given. In principle, it would be possible to start at $\rho = 0$ in this case as this state corresponds to a steady state. However, the aim was to demonstrate that an arbitrary input from simulations can be used as an initial state. The bifurcation diagram is continued for $\rho < 0$ for a while. This was used to check if the bifurcation diagram mirrors the symmetry of ρ correctly, which it does. At $\rho = 0$ the system is translationally invariant in space. In general, the demo problem is not translationally invariant. An inhomogeneity in the wettability was introduced to avoid the constraint necessary for spatial translational invariance.

The proof of concept for this method can be considered a success. However, for further applications, some things have to be kept in mind. The strength of the attractor of the periodic orbit can be small compared to steady state solutions. This can be a problem, especially in the first correction step from the initial data. Higher discretization in space and time and small continuation step sizes improve this at the cost of computational time.

4

MAPPING BETWEEN MICROSCOPIC AND MESOSCOPIC SCALES

For non-equilibrium relaxation dynamics of a liquid droplet on a switchable substrate, the interplay of different length and time scales plays a decisive role, which needs to be understood. This chapter presents a method to map the microscopic information from a molecular dynamics simulation to a mesoscopic scale, reflected by a thin-film model. After a discussion of the mapping procedure, the relaxation of a liquid droplet upon switching the wettability of the substrate is analyzed. Further, it is shown that a nearly identical mapping procedure can be used to describe two coalescing droplets. This procedure is a first step to extend the mapping from the equilibrium case to non-equilibrium wetting dynamics, thus allowing for quantitative multi-scale analysis.

This is a timely topic as current research on materials promises significant advances to improve switching reliability, enlarge the possible change in contact angle and increase the feasible switching frequency. Switchable substrates can change their wettability when an external stimulus like a change in pH value or illumination with light of a defined wavelength occurs. Prominent examples for such surfaces are inorganic materials like TiO_2 or ZnO [23–25] which have the advantage of a large difference between the contact angles before and after switching. Since the switching process from the hydrophilic to the hydrophobic case for these substrates is rather slow, another class of substrates is of great interest, namely substrates coated with a self-assembled monolayer (SAM) consisting of molecules with azobenzene or other photoresponsive moieties [16–18]. The azobenzene moiety can be switched with UV light from a trans to a cis state which has a lower wettability while the reverse process can be induced by illumination with blue light. These surfaces adapt much faster at the disadvantage of lower contact angle differences. However, with the help of microstructuring, a higher change in contact angle can be achieved [19, 20].

Switchable substrates promise rich non-equilibrium behavior and an additional mechanism to control pattern formation, which can be employed in addition to static pre-structures. In particular, it was demonstrated that it is possible to guide the movement of a droplet reversibly by applying a light gradient [15, 18], i. e. changing the wettability close to the droplet. Recent theoretical work by Grawitter and

Stark [80] investigated how droplets can be steered with the help of spatio-temporal wettability patterns using the macroscopic boundary element method. This is relevant especially for the development of lab-on-a-chip devices [95]. Theoretical models play a key role to gain an improved understanding of the non-equilibrium behavior on switchable substrates. In particular, to study microscopic phenomena atomistic simulation methods like molecular dynamics have become an established approach [96–98]. On larger length and time scales mesoscopic thin-film descriptions have been successfully applied for a variety of different wetting systems, see the reviews [30, 34, 99]. While microscopic MD simulations can incorporate more details of the specific interactions between liquid and substrate, continuum mesoscopic models cannot resolve microscopic details but are able to address much larger length and time scales. Furthermore, continuous mesoscopic models allow the tool kit of bifurcation analysis to be applied for the investigation of instabilities. This offers analytical insights which are often not possible in discrete, microscopic models. Bifurcation analysis combined with parameter sweeps, which are computationally cheaper compared to microscopic models, can then indicate interesting parameter regimes and time scales to analyze in the microscopic model for a more detailed investigation. This helps avoid computational costs for simulations in irrelevant regimes.

Thus, combining different microscopic and continuum descriptions seems natural and has been done by Wu, Fichthorn and Borhan [12], among others. There, the spreading dynamics of drops on solid surfaces were investigated by solving the Navier–Stokes equations in a continuum domain comprised of the main body of the drop together with MD simulations in a particle domain in the vicinity of the contact line. Another example of the combination of models across length and time scales is the work by Zhang, Borg and Reese who combined MD with volume of fluid simulations to study droplet spreading on surfaces [100]. Also, Hadjiconstantinou supplied both, a continuum and MD method for the flow of two immiscible fluids in a channel [101]. In Ref. [29] kinetic Monte Carlo simulations and a thin-film continuum model were combined to comparatively study the Plateau-Rayleigh instability of ridges formed on pre-structured substrates. It was shown that the evolution of the occurring instability qualitatively agrees between the two models.
The combined approach with an MD and a TF model presented in this chapter is closely based on the following publication:

[1] M. Stieneker, L. Topp, S. V. Gurevich and A. Heuer. "Multiscale perspective on wetting on switchable substrates: mapping between microscopic and mesoscopic models." In: *Phys. Rev. Fluids* 8 (1 2023), p. 013902. DOI: 10.1103/PhysRevFluids.8.013902.

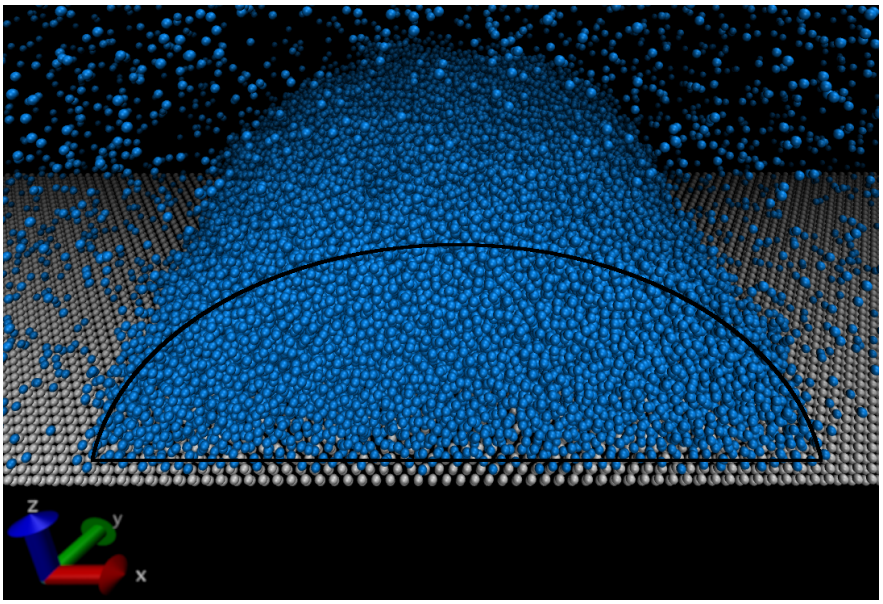

Figure 4.1: Snapshot from an MD simulation showing fluid particles (blue) forming a cylindrically shaped droplet placed on two layers of an fcc(111) surface.

4.1 THEORETICAL PRELIMINARIES

Figure 4.1 shows a snapshot from an MD simulation. The theoretical background for the MD model is explained in Section 2.2. For the analysis, the non-dimensionalized form of the TF Eq. (2.24) as derived in Section 2.1.3 is used. In the MD model, there is no equivalent precursor film, so the parameter χ corresponding to the ratio of the precursor film height to the chosen reference film height h_0 has to be chosen small. A value of $\chi = 0.01$ is used in the following because smaller values of χ do not change the contact region significantly and would lead to increased computational efforts and numerical problems. Note that for different values of the wettability parameter ρ the ratio of the precursor film height h_p to the maximum droplet height $h_{\max}$ does change for constant volume.

It should be noted that temperature does not enter directly into the TF model. However, indirectly the temperature enters the TF model through the surface tension γ, the viscosity η and the particular shape of the disjoining pressure, which determines the wetting regime. In particular, the minimum of the interface potential (the integral of the disjoining pressure) is directly connected to the contact angle in the mesoscopic picture as a known disjoining pressure is sufficient to determine the equilibrium state [28, 34]. Direct temperature dependence can be incorporated in thin-film models, e. g. Davidovitch, Moro and Stone have shown that higher temperatures lead to faster

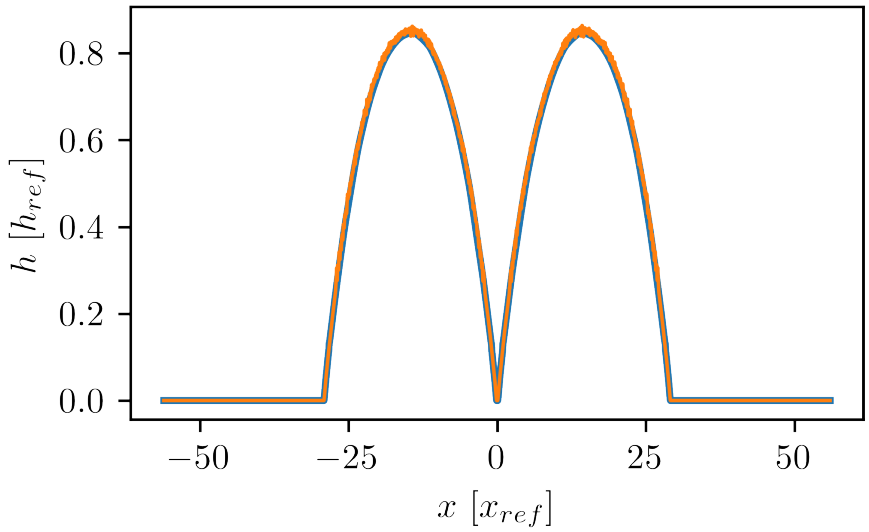

Figure 4.2: Comparison of the height profile directly extracted from the MD model and the height profile after a LOWESS filter was applied to the parts of the MD data, where $h > 20h_p$.

spreading [65]. Here, this would be incorporated via a lower viscosity.

In general, one can use profiles from the MD model as an initial profile to start simulations in the TF model. As the MD model exhibits noise this requires small time steps in the simulation to reach a smooth profile. In some circumstances, the time steps in the employed adaptive time stepping algorithm can get so small, that rounding errors of the machine can influence the results. To avoid such behavior, a filter to the MD data is applied before the simulations in the TF model are started. The averaging of 50 trajectories does not make the height profile sufficiently smooth. Figure 4.2 shows the difference between the filtered and the unfiltered data. For data points with a height above 20 times the precursor film height, the LOWESS (Locally Weighted Scatterplot Smoothing) filter from the python package STATSMODEL [102] is applied to the height profile. This excludes the contact region from the filter because the noise in the contact region is comparatively low (see Fig. 2.3).

4.2 HOW TO COMPARE SCALES

To compare the scales in the case of a static droplet, a mapping between ϵ_w and ρ responsible for the wettability in their respective models is necessary. For dynamic comparisons, the time scales need to be mapped as well. In the first part of this section, the mapping in the static, equilibrium case is described. In the second part, the mapping

of the time scales is described.

The relation of the liquid-solid interaction strength to the contact angle has been the focus of research for quite some time, e. g. Sullivan [103] came up with a qualitative theory based on a van der Waals model in 1981. This is closely related to the research on wetting transitions substantially advanced by [104–107]. Pandit, Schick and Wortis [104] investigated the wetting transition within a lattice-gas model for different interaction strengths and interaction ranges. Within the framework of a systematic van der Waals theory (mean-field model), critical wetting can also be observed [105]. Such critical wetting is non-generic as shown first by Dietrich and Schick [106]. Despite the efforts in this field, there is no way to compute the relation between the interaction strength ϵ_w and the wettability parameter ρ without doing involved numerics. Even if possible, theories often only promise qualitative agreements [103], which is insufficient for the aim of a quantitative agreement in the dynamics of microscopic and mesoscopic models. For an even better agreement of the equilibrium droplet shapes, one could try to extract the exact shape of the disjoining pressure Π. As mentioned in Section 2.1.1, the disjoining potential can in principle be extracted from MD simulations, lattice density functional theory (DFT), and continuum DFT [58–61]. However, the extraction of wetting potential is tricky and some open questions remain [61].

Here, a different approach is chosen and the interaction strength ϵ_w from the MD model is mapped to the parameter ρ from the TF model so that according to an appropriate criterion both models show the same droplet shape. Since the volume is fixed, the shape of the static droplet is characterized by just one parameter such as the height or the contact angle. Consequently, ρ is used for a reliable, yet, empirical static mapping. This allows taking the next step of a quantitative comparison not only of statics but also of dynamics.

Contact angles are hard to define and measure consistently in microscopic and mesoscopic models. The definition of the contact angle can have a strong influence and at the nanoscale the contact angle can depend on the droplet size [108]. Indeed, in the mesoscopic TF model the contact region is not represented accurately due to the lubrication approximation [34]. Additionally, the contact line is hard to define due to the necessarily smooth transition to the precursor film. Consequently, it is not clear how results based on a contact angle mapping can be interpreted reliably. Figure 4.3 shows two mapped equilibrium profiles based on the mapping described in the following to give an idea, of how the lubrication approximation (blue curve) influences equilibrium droplet shapes in the contact region.

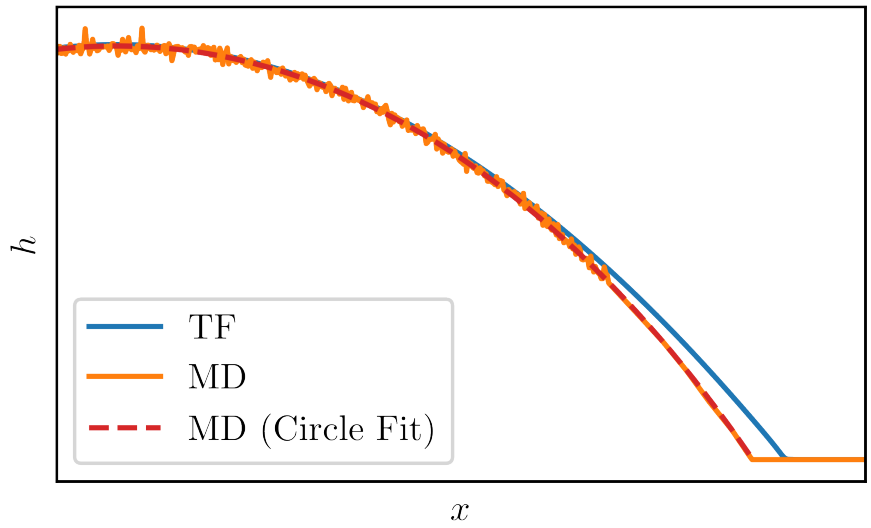

Figure 4.3: Spatially rescaled height profiles of a static droplet from the MD and TF model corresponding to $\epsilon_w = 0.762$ and a circle fit to the height profile from the MD model.

Instead of the contact angle, the *the relative full width at half maximum* rFWHM is introduced, which is defined as the height of the droplet divided by its width at half of the height. This parameter is not sensitive to the droplet shape in the contact region while being sensitive to the overall shape. The measure rFWHM can be regarded as a computationally cheap way to estimate the curvature and thus is closely related to the contact angle. Another advantage of the rFWHM is that one can straightforwardly analyze the temporal evolution. If one measures the contact angle by fitting the droplet shape with a circular cap, the quality of the fit varies because dynamic droplets do not necessarily have a circular cap shape and thus the error margin of the measured contact angle changes.

Figure 4.4 shows the dependence of the rFWHM on the parameters ϵ_w and ρ responsible for the wettability in their respective models which is determined by a parameter scan where a single droplet is equilibrated on a homogeneous substrate. The rFWHM shows an approximately linear dependence on the interaction parameter squared ϵ_w^2 so that a linear fit is employed to avoid a computationally costly parameter sweep with a higher resolution in ϵ_w. The lower computational cost in the TF model makes a detailed parameter sweep possible so that linear interpolation can be used to compute the rFWHM for arbitrary values of ρ and vice versa. Combining both results yields a reliable, numerical mapping between ϵ_w and ρ as can be seen in Fig. 4.5. Additionally, Fig. 4.5 shows the mapping for different reduced temperatures. At higher temperatures, a defined interaction strength ϵ_w is mapped to a lower value of ρ, which corresponds to a lower

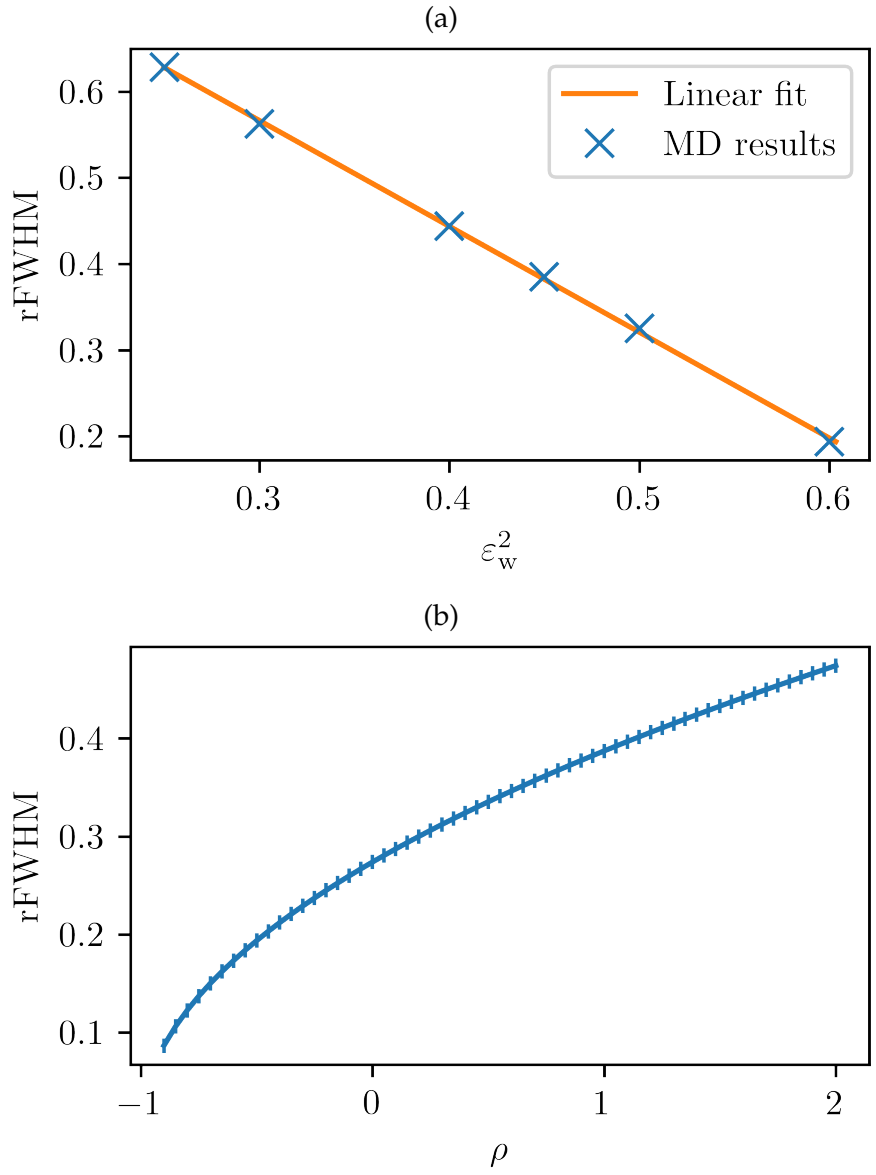

Figure 4.4: Dependence of the rFWHM on the parameters responsible for the wettability in the MD model (a) and the TF model (b). The linear fit shown in (a) and an interpolation of the data shown in (b) is the base for the mapping between ϵ_w and ρ in Fig. 4.5.

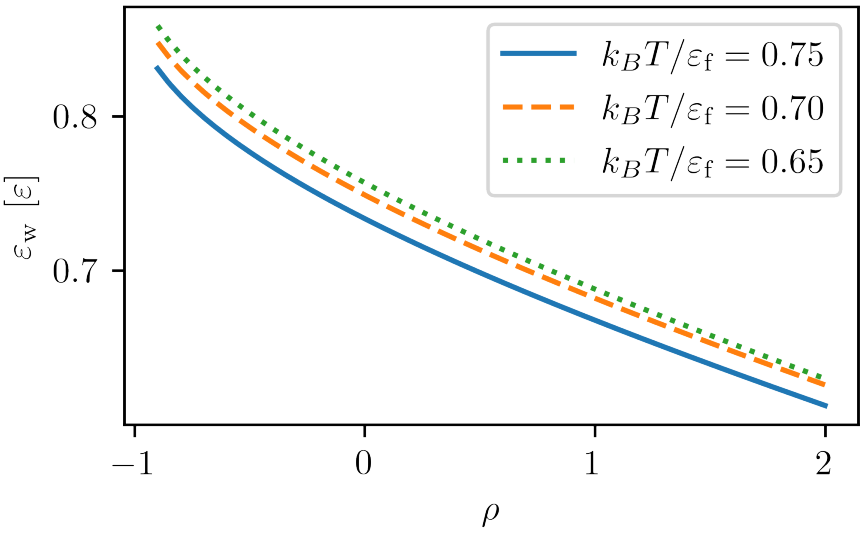

Figure 4.5: Resulting mapping from the parameter ρ modulating the disjoining pressure in the thin-film picture to the interaction strength between solid and liquid ϵ_w in the MD model. The mapping is shown for multiple reduced temperatures. $k_BT/\epsilon = 0.75$ is the value used for all the simulations within this chapter.

contact angle. This explains how the disjoining pressure can capture the temperature dependence implicitly in the TF model.

For the mapping of the spatial scales, the x- and z-coordinates can be simply normalized with the maximum height h_{ref} of the droplet in the corresponding model at a certain wettability. Here, the maximum height of a droplet on a surface with a wettability corresponding to $\epsilon_w = 0.632\ \epsilon$ in both models is used to scale the film height and the $x-$coordinates ($h_{ref} = x_{ref}$). In principle, the scaling height can be chosen arbitrarily as long as it corresponds to the same height in both models, i. e. droplet height at a certain wettability. A comparison of static droplet shapes from both models can be seen in Fig. 4.3. Both profiles match well for heights of $h > 0.4\,h_{\max}$. As anticipated, there is some deviation in the contact region due to the lubrication approximation in the TF model. Note that the reduced noise strength in the contact region is due to the crossing criterion shown in Fig. 2.3.

To achieve a relatively generic approach for the mapping of the time scales, the measure K defined as

$$K = \frac{\int_{h>0.4h_{\max}} x^2 h \, \mathrm{d}x}{\left(\int_{h>0.4h_{\max}} h \, \mathrm{d}x\right)^2} \tag{4.1}$$

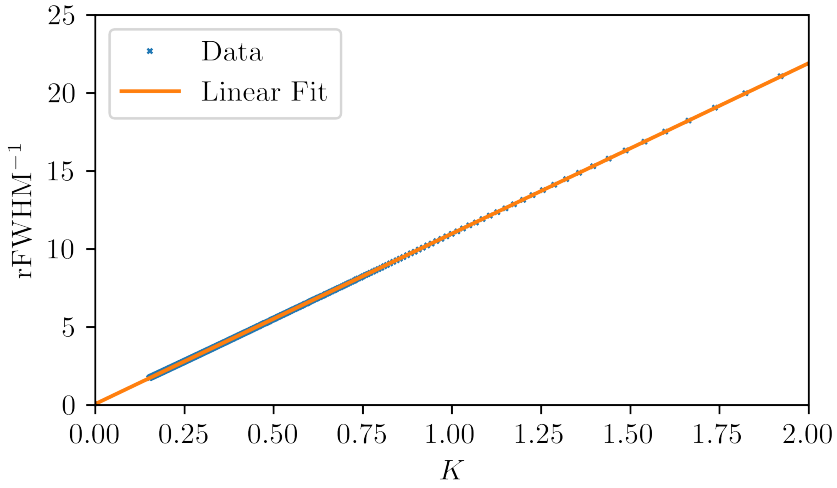

Figure 4.6: K vs. rFWHM^{-}1 under the assumption of circularly shaped droplets and a linear fit to the data. The fit parameters are shown in Eq. (4.3).

is computed for the profiles in the TF and the MD model. To compensate for small differences of K present in the static droplet profiles the measure K is normalized between 0 and 1 via

$$K_{norm} = \frac{K - K(t=0)}{K(t=\infty) - K(t=0)}. \tag{4.2}$$

Small errors would propagate to the dynamic mapping otherwise. Note that $K(t=\infty)$ is determined as an average over $\Delta t = 20 \cdot 10^4\ \tau$ to minimize the influence of noise. In contrast to the rFWHM, this choice of K has the advantage that it can be applied to different use cases like a droplet adapting to a new surface wettability or the coalescence of two droplets as shown later. For a situation with two droplets, the rFWHM cannot be defined reasonably. An important condition for the measure K is the monotony, which cannot be guaranteed generally. However, an alternative suitable measure can be found for every situation. However, it might get arbitrarily complicated.

Interestingly, it is possible to calculate the rFWHM from K in the case K is calculated for a system with a single droplet with the numerically obtained formula

$$\text{rFWHM} = \frac{1}{0.0614 + 10.92K}. \tag{4.3}$$

This is a result of a numerical computation shown in Fig. 4.6 under the assumption of a circular shape.

To exclude systematic errors originating from the lubrication approximation and its effect on the contact region only regions with

$h > 0.4\,h_{\max}$ are considered in Eq. (4.1). Note that the threshold value $0.4\,h_{\max}$ only has a small influence as long as the major part of the contact region is not accounted for. Physically K can be understood as a measure of the variance or spread of the liquid. However, the physical interpretation is not relevant for the mapping and K can be substituted by any measure with monotonous evolution for the situation under investigation.

To match a time in the MD model to a time in the TF model, the deviation $\Delta = |K_{\mathrm{MD}} - K_{\mathrm{TF}}|$ is minimized for every time step in the MD model This results in a mapping $t_{\mathrm{MD}} \mapsto t_{\mathrm{TF}}$. The mapping in this direction is more convenient as the MD model is a first principle model and uses a constant time step in contrast to the TF model.

In the following, the mapping technique is applied to two different cases to demonstrate its applicability and versatility. The first example is a liquid ridge on a homogeneous, switchable substrate. As a second example, the coalescence of two ridges is considered. The second example underlines that the mapping method can be applied universally and does not require additional simulations or measurements, where one had to worry about initial conditions influencing the measurement of a characteristic time.

4.3 SINGLE SWITCH ON A HOMOGENEOUS SUBSTRATE

In this section, the mapping procedure presented in Section 4.2 is applied to the dynamics of a one-dimensional ridge on a switchable substrate. The procedure for the simulations is as follows: The ridge is equilibrated at either high or low wettability ($\epsilon_{HW} = 0.762\,\epsilon$ and $\epsilon_{LW} = 0.632\,\epsilon$, respectively) before the wettability is instantaneously switched to the other wettability at $t = 0$.

Figure 4.7 (a) and Fig. 4.7 (b) show the results of the mapping approach for switching towards higher and lower wettability, respectively. In both cases, the data points of the mapping hardly deviate from a linear fit. Only the first two matched time steps deviate from the linear fit. This is possibly due to initial inertial effects in the MD model, which are not present in the TF model [30, 34]. Consequently, a linear fit of the mapping does not go directly through the origin. As expected, deviations between the MD model and the TF model exist in the contact region, corresponding to regions of the droplets with small heights. As a consequence, the mapping is becoming worse for very high wettabilities because the contact region is more extended. A cut-off for large times needs to be introduced because eventually changes in the droplet profile between time steps are dominated by noise in

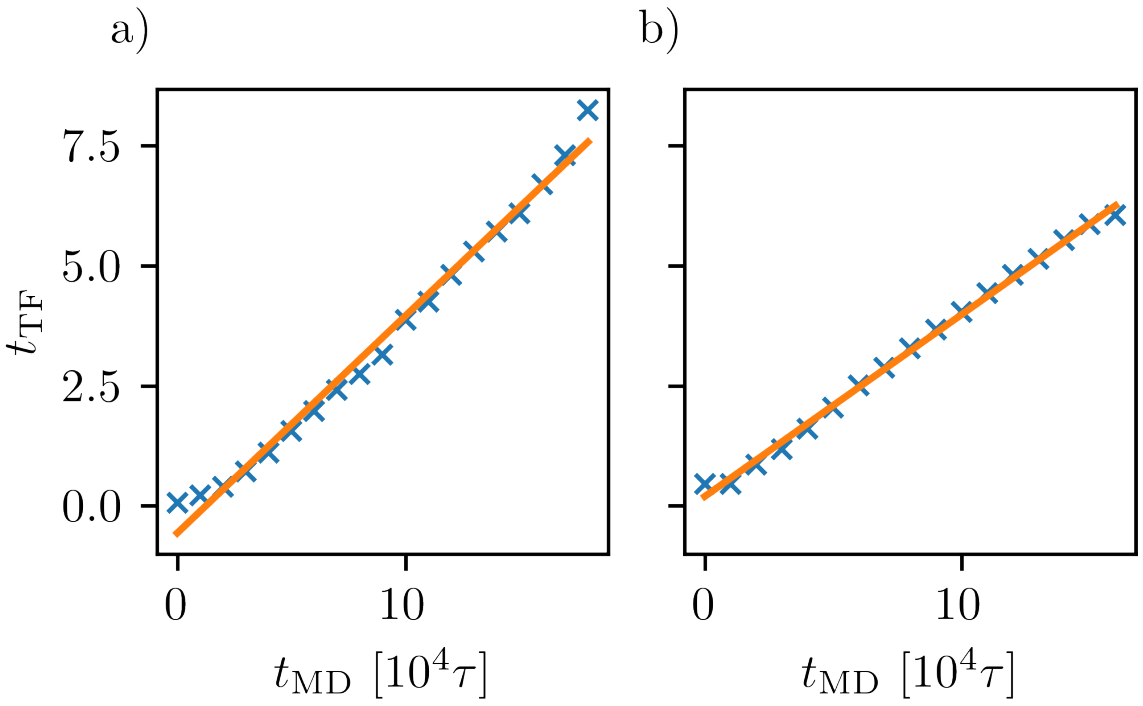

Figure 4.7: Result of the mapping approach applied to (a) the switching from ϵ_{LW} to ϵ_{HW} (blue data points and orange linear fit) and (b) from ϵ_{HW} to ϵ_{LW}.

the MD model and matched times are not meaningful anymore.

The space-time representations in Figs. 4.8 and 4.9 show the evolution of the film profile $h(x, t)$ as the ridge adapts to the new wettability. Figure 4.9 compares the MD and TF model results when switching from high to low wettability. The inverse switching direction is shown in Fig. 4.8. In both Figures, the color map indicates the film's height. The results from both models look very similar in this representation. Besides the noise in the MD model, the offset for the switch towards higher wettability accounts for the only general difference. This offset is a consequence of the previously described effect of the initial assimilation. To better grasp how well the models compare, the change of the height in time at three distinct points in space is shown in Fig. 4.10. These three points in space are marked and labeled in Figs. 4.8 and 4.9 with a red line and roman numerals. For the direct comparison between the models, times from the TF model are converted into MD units τ.

For both switching directions, the evolution of the height at points I and II are in close agreement between the models. The situation is however a bit different for point III. Only for maximum profile heights reached at this position the agreement is close. For smaller heights, you can see differences. This behavior can easily be explained

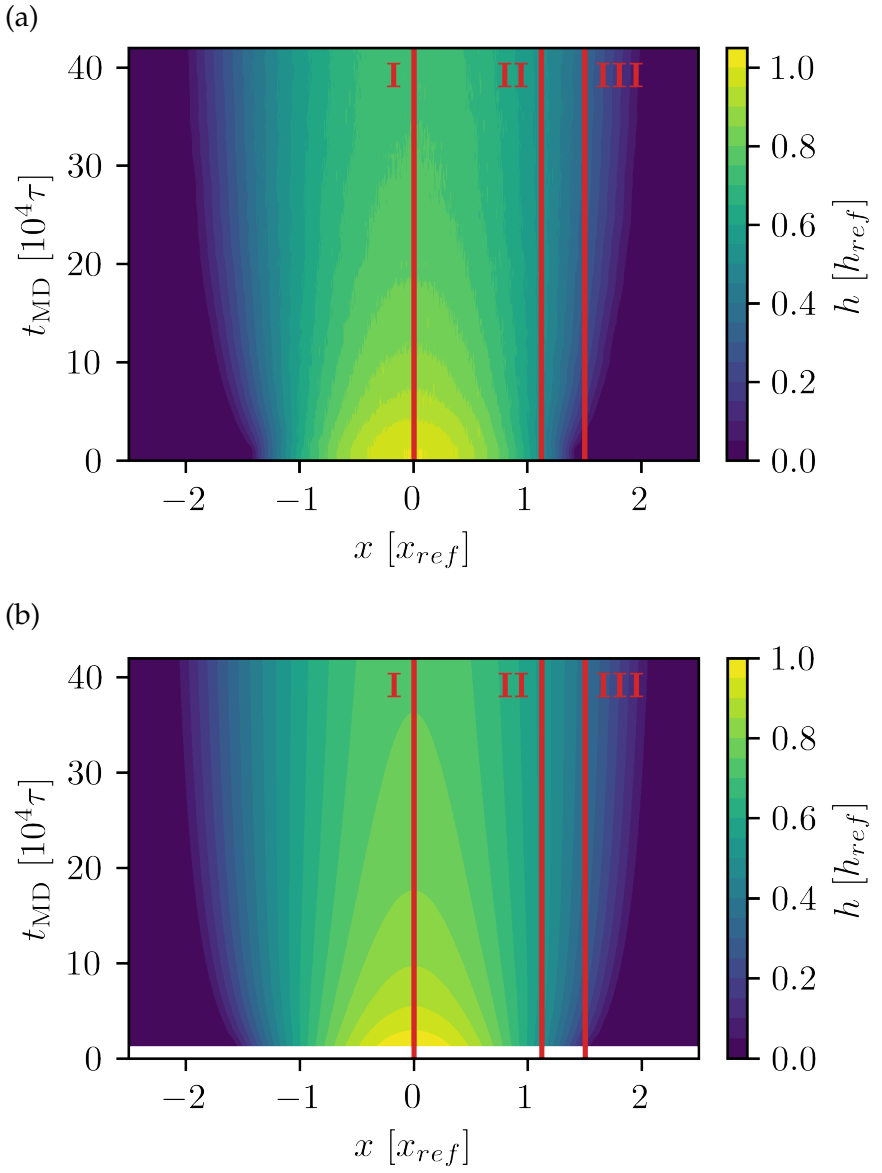

Figure 4.8: Space-time plots showing the evolution of the height profile after a change in wettability from $\epsilon_{LW} = 0.632\ \epsilon$ to $\epsilon_{HW} = 0.762\ \epsilon$ in the (a) MD model and the (b) TF model. Red vertical lines labeled I, II and III indicate at which positions the height profile evolution is shown in Fig. 4.10.

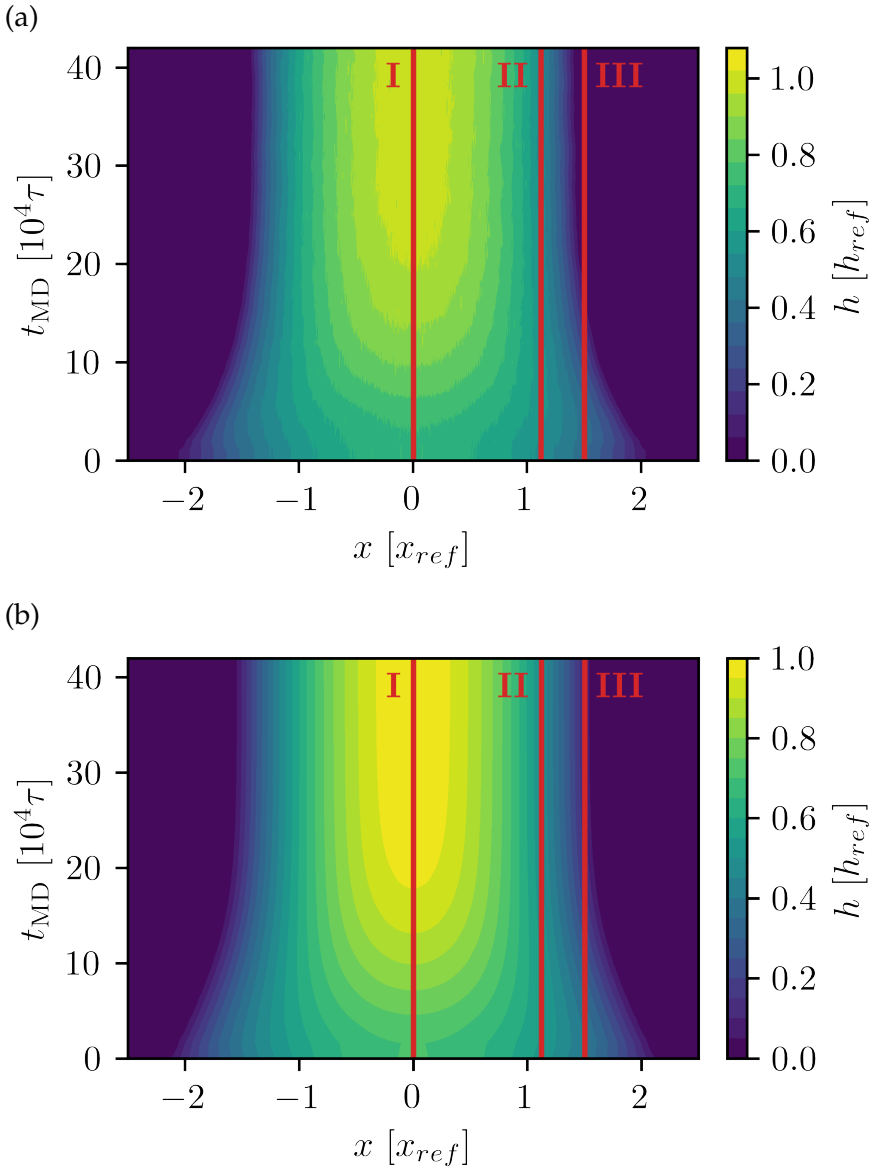

Figure 4.9: Space-time plots showing the evolution of the height profile after a change in wettability from $\epsilon_{HW} = 0.762\,\epsilon$ to $\epsilon_{LW} = 0.632\,\epsilon$ in the (a) MD model and the (b) TF model. Red vertical lines labeled I, II and III indicate at which positions the height profile evolution is shown in Fig. 4.10.

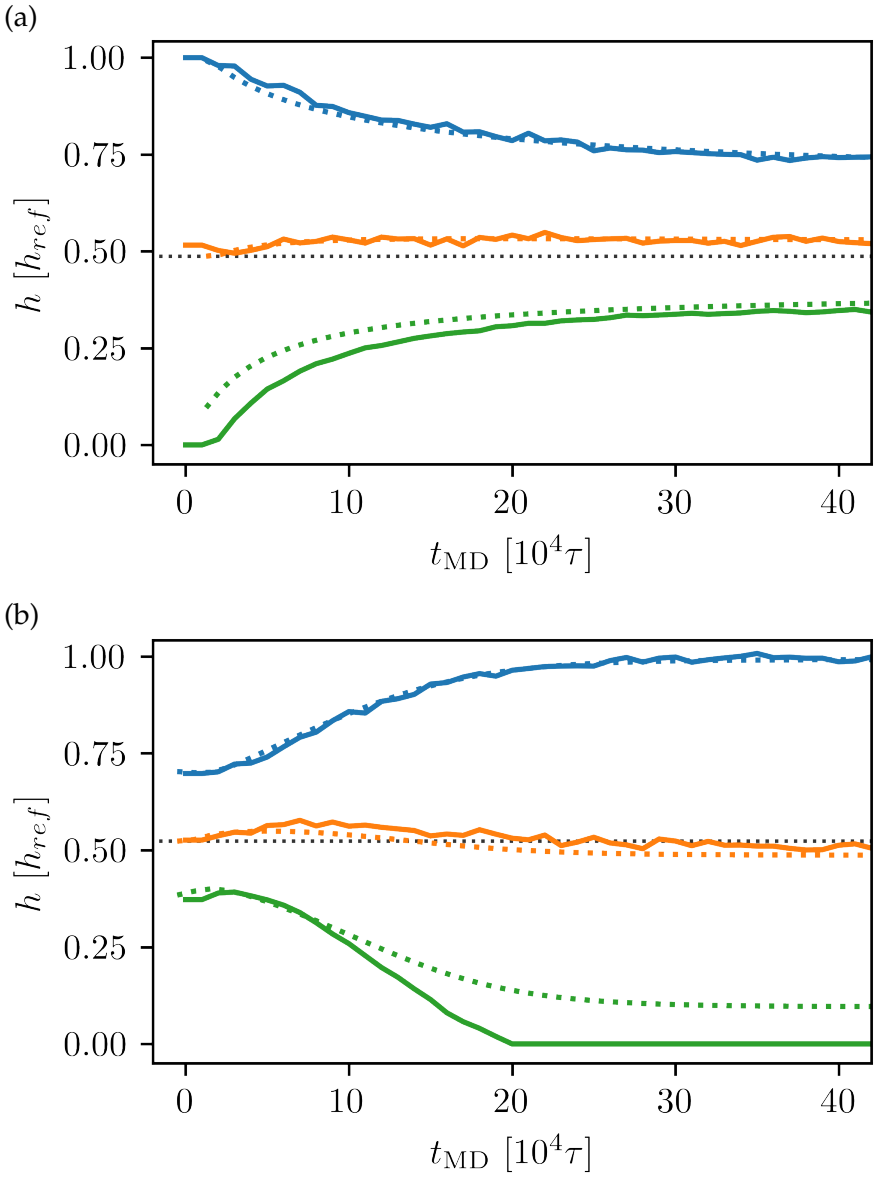

Figure 4.10: Three characteristic height profiles along the marked lines I (blue), II (orange) and III (green) as shown in Figs. 4.8 and 4.9. The height profiles extracted from the MD model are presented with solid lines. The dotted lines are TF results with the temporal scaling obtained using our mapping approach. The height h is given relative to the maximum height. The black dotted line indicates the initial height in the TF model for slice II to emphasize the non-monotonous behavior for the height profile at this position. (a) the wettability is switched from low to high, (b) the wettability is switched in the opposite direction.

since already static ridges from both models do not match well in the region located close to the contact line (cf. Fig. 4.3). The reason is the underlying lubrication approximation in the TF model, which results in higher film heights in the contact region compared to the MD model.

One can also find a position, where the height profile behaves non-monotonically. In particular, for point II the film height increases first and then decreases to its equilibrium value. This effect occurs for both switching directions, although it is more pronounced when switching from high to low wettability. The dotted black lines in Fig. 4.10 are a guide to the eye to better see the non-monotonous behavior. In general, it is not surprising to find this non-monotonical behavior since this occurs also in the Gaussian solution of the heat equation or Fick's second law. However, finding such a distinct behavior in both models confirms that the parameters are chosen in such a way, that both models show consistent behavior, as this behavior could also be present at a different film height, a different position or a different point in time.

Table 4.1 shows resulting time scale ratios (corresponding to the slope of the linear fit) for the switching process between different wettabilities. Note that the value of R, in general, could depend on the initial and the final wettability. The data in Table 4.1 does not indicate that there is a dependence on the initial wettability at least not within the error margin. The error margin is approximately 10% if you consider the influence of the cutoff for the fit. Notably, the time scale ratio R shows a tendency to decrease if the wettability increases. However, the resulting deviations are quite small (less than a factor of two in the considered range of wettabilities). Furthermore, a linear time mapping is observed for all wettabilities. This shows that indeed the droplet evolution, seen in the MD simulations, is well reflected by the TF.

Note, that the magnitude of the scaling factors can be expected by comparing the time scales from TF and MD simulations. Since the time scale of the TF simulations is $t_0 = \frac{3\eta h_0}{\gamma}$ (cf. Section 2.1.3) this would result in a value of $t_0 \approx 3.9 \cdot 10^4\,\tau$ by plugging in the values $h_0 = 14.40\,\sigma$ and $\eta = (2.14 \pm 0.08)\sqrt{M\epsilon}/\sigma^2$ and $\gamma = (0.477 \pm 0.005)\,\epsilon/\sigma^2$ obtained from the MD system (cf. Section 2.2.1).

4.4 COALESCENCE OF TWO RIDGES

As a second test case for the quality of the mapping procedure between the MD and TF models, the coalescence of two ridges on a homogeneous substrate is investigated. To get an input geometry a ridge on a surface with a wettability of $\epsilon_w = 0.707\,\epsilon$ is equilibrated in an MD simulation. A copy is then translated in x-direction in such a way, that it has a distance of 0.5 σ from the primary ridge at the

Table 4.1: Comparison of time scale ratios for different wettabilities and wettability differences computed with our mapping approach.

ϵ_{LW} [ϵ]	ϵ_{HW} [ϵ]	$R_{f_{\mathrm{HW}\to\mathrm{LW}}}$ [τ]	$R_{f_{\mathrm{LW}\to\mathrm{HW}}}$ [τ]
0.632	0.671	$2.98 \cdot 10^4$	$2.70 \cdot 10^4$
0.671	0.707	$2.95 \cdot 10^4$	$2.45 \cdot 10^4$
0.707	0.742	$2.13 \cdot 10^4$	$2.15 \cdot 10^4$
0.632	0.762	$2.64 \cdot 10^4$	$2.21 \cdot 10^4$

contact line. To maintain the particle density the MD system (and thus the surface) was further extended in the x-direction by a factor of two. From this MD input geometry, the positions for the liquid-vapor-transition of the two ridges were calculated and used as the input data for the TF simulations.

The spatial rescaling from the single switch experiments can be employed without further issues. The result of the temporal mapping can be seen in Fig. 4.14. One can observe that in this case the relation between both models cannot be reasonably fitted with a single linear function. Instead, a piece-wise linear function is well suited to represent the data. In Fig. 4.14 the colors of the linear fits match the data points used for fitting. The intersection of the linear functions is at $t_{\mathrm{MD}} = t_c = 18.1 \cdot 10^4\,\tau$. The red, dotted lines in Fig. 4.14 visualize corresponding times exemplarily.

In particular, the time t_c (black dashed line) corresponds to the time at which there is no longer a local minimum in the height profiles, i.e. the time at which the merging process of both droplets is completed. After t_c is reached, the droplet still contracts further. The time scale ratios are $R_{f_{coal,1}} = 3.64 \times 10^4\,\tau$ in the first part and $R_{f_{coal,2}} = 1.71 \times 10^4\,\tau$ in the second part.

The temporal mapping shown in Fig. 4.14 is based on the evolution of the measure K_{norm} defined in Eqs. (4.1) and (4.2). For the coalescence, the evolution of K and the normalized version K_{norm} is shown in Fig. 4.11. One can see only slight differences in the absolute values of K in addition to initial, small deviations between the models. Most likely this is related to the MD input data used in the TF model. Note that K does not decrease monotonically for a brief time around $t = 0$. This is reflected in Fig. 4.14 by the first few points which do not agree with the linear fit as well as the data points for later times. Figure 4.12 shows the evolution of K_{norm} on a logarithmic scale. The logarithmic scale is able to visualize that a single linear fit of the mapped times is not sufficient. This is not obvious only looking at Fig. 4.11.

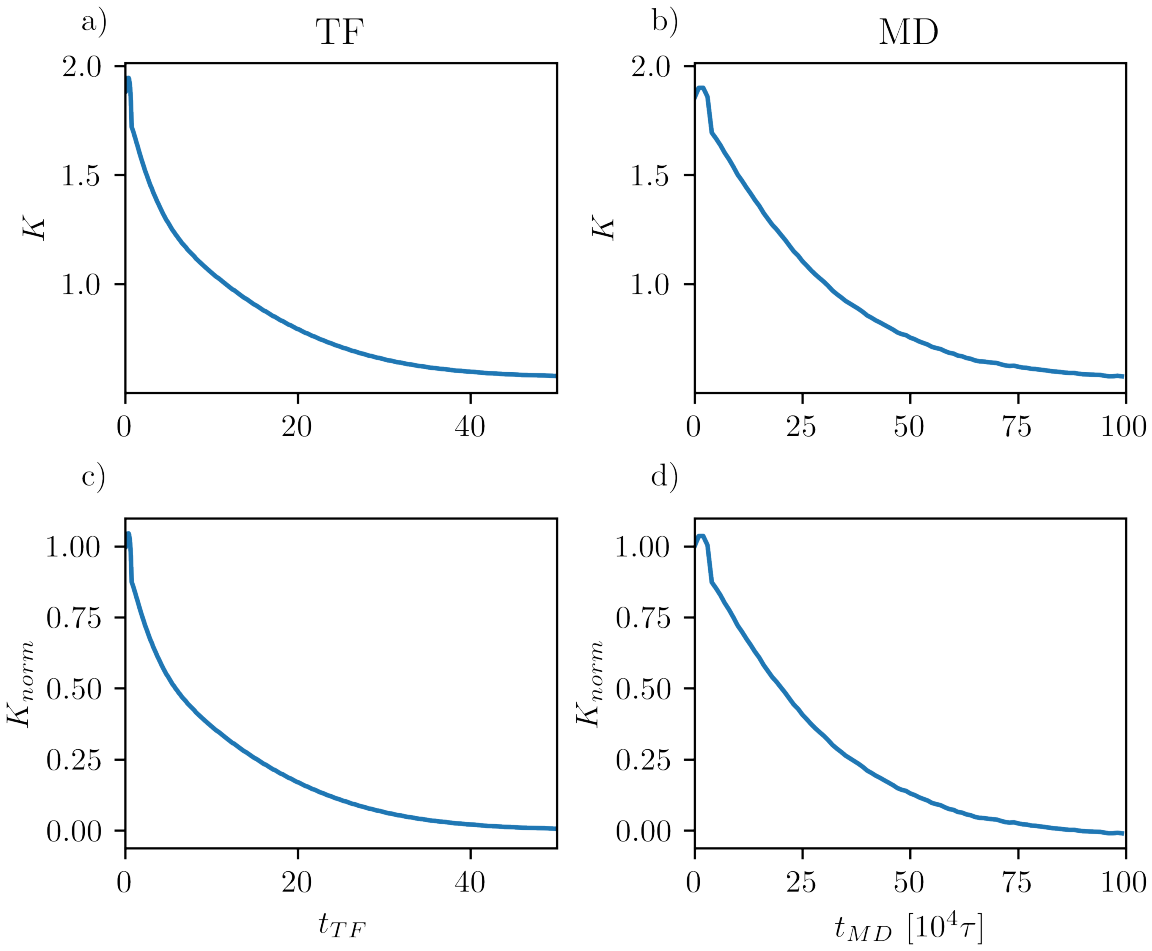

Figure 4.11: Evolution of K and K_{norm} for the TF (see. (a), (c)) and the MD model (see (b), (d)) during the simulations of coalescence, which builds the base for Fig. 4.14.

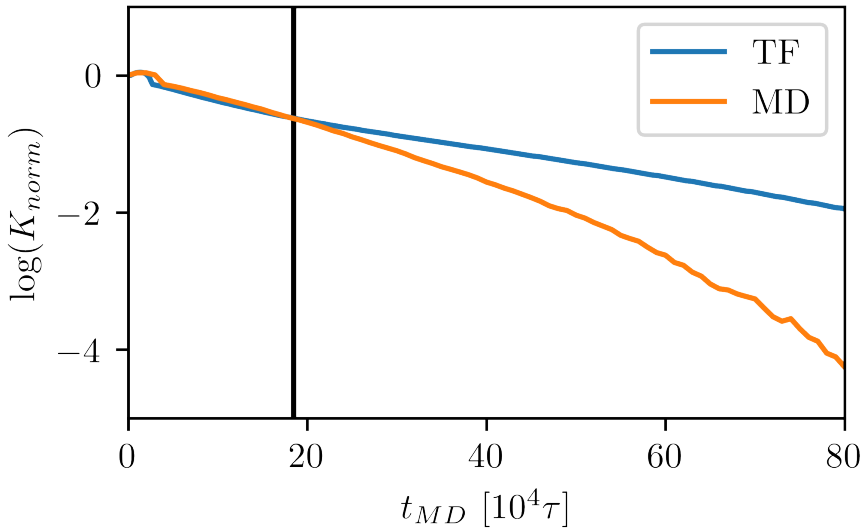

Figure 4.12: Evolution of K_{norm} on a logarithmic scale for the coalescence simulations. t_{TF} was scaled by the initial slope of the matched times. The solid black lines correspond to the intersection of the two linear fits of the matched time.

To illustrate the temporal mapping shown in Fig. 4.14, Fig. 4.13 directly compares two matched height profiles. The deviation at the contact region is expected as a consequence of the lubrication approximation. The magnitude of the deviation is comparable to the deviations shown in Fig. 4.3. The matched profiles in (b) correspond to times close to the critical time t_c, where both linear fits intersect in Fig. 4.14. Again, the mapping approach can be used to check the similarity of both approaches in the space-time plot; see Fig. 4.15. Furthermore, in Fig. 4.16 the evolution of the height profile at three distinct points is highlighted. The results match very well except for the anticipated difference at the contact region.
Note that the value of $R_{f_{coal,2}} = 1.71 \times 10^4\,\tau$ deviates not much from the value of $2.1 \times 10^4\,\tau$ which is observed for a single switch in Table 4.1 for the final wettability $\epsilon_w = 0.707\,\epsilon$. About the significant deviations for $R_{f_{coal,1}}$ one can only speculate. Possibly, the choice of the mobility in the TF approach does not fully reflect the processes in the initial coalescence regime. Figure 4.16 shows that the deviations between the MD and the TF profile are higher for $t \in [0, t_c]$, especially for $x = 0$. This could indicate that the path in phase space does not agree as well as in the case of a single switch and the disjoining pressure might need improvement.

It is also possible that an initial solution in the TF model directly taken from the MD model encourages these deviations because the differences in the contact region lead to an initial state in the TF model, which is farther away from the equilibrium state than the

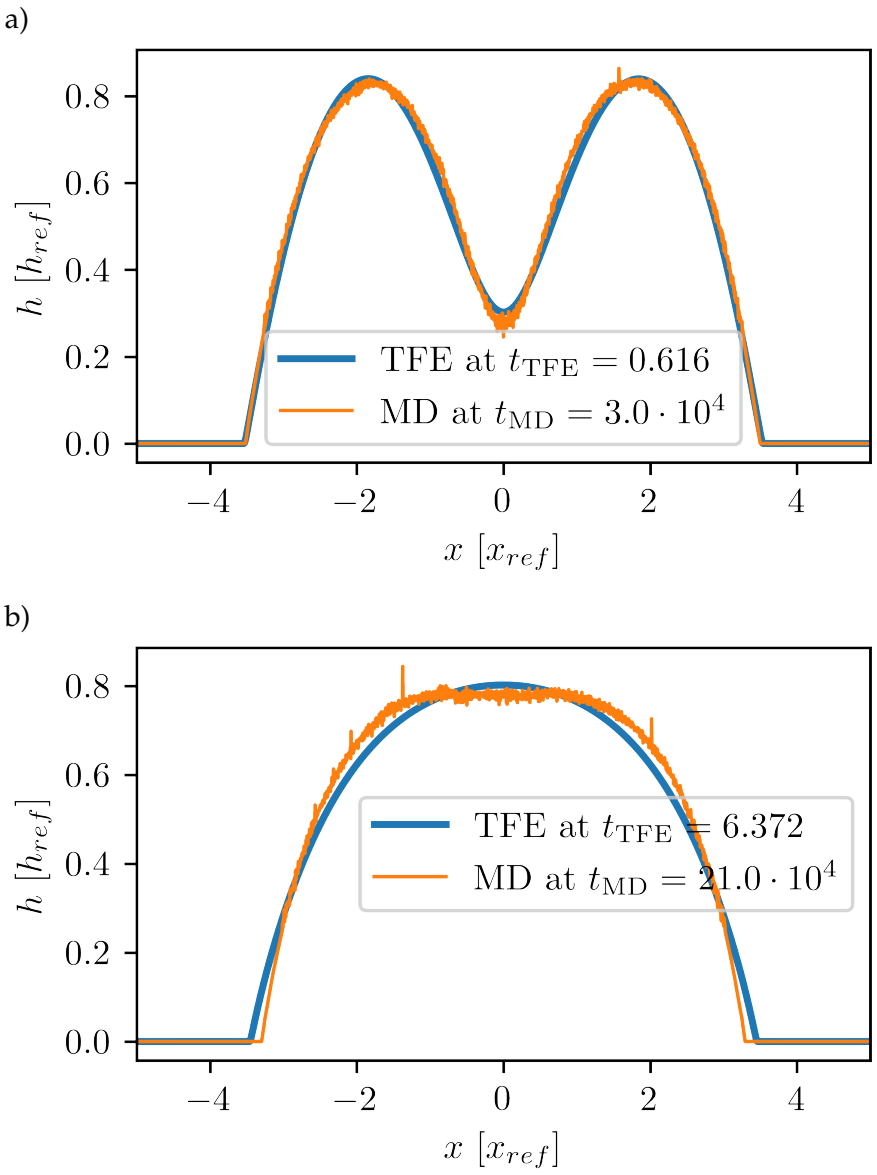

Figure 4.13: Two examples of a height profile from MD simulations matched to a height profile from the TF model taken from the coalescence simulation shown in Fig. 4.15.

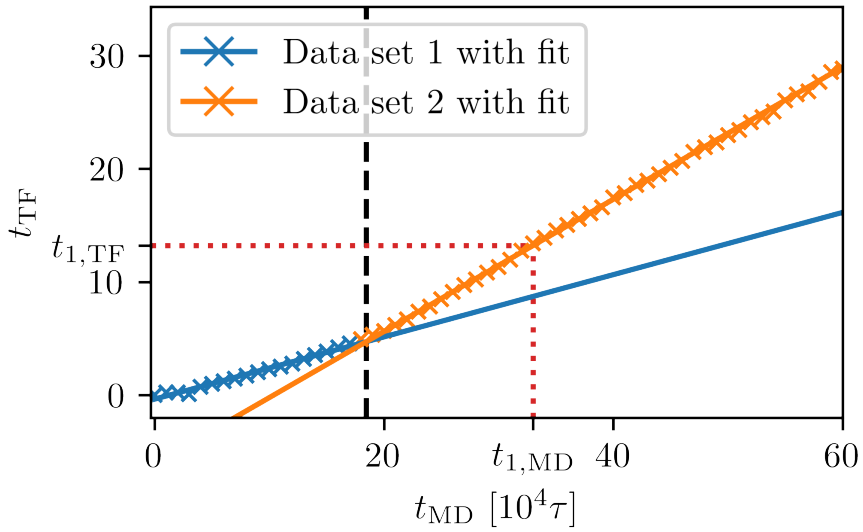

Figure 4.14: Result of the temporal mapping for the coalescence of two ridges. Data points of the matched profiles are shown as crosses. Only the crossed data points in matching colors are considered for the corresponding fit shown as a solid line. Two distinct time scales can be observed, both fitted with a linear function. The slopes are $a_1 = (2.64 \pm 0.10) \cdot 10^{-5}\ \tau^{-1}$ and $a_2 = (5.892 \pm 0.030) \cdot 10^{-5}\ \tau^{-1}$. This corresponds to timescale ratios of $R_{f_{coal,1}} = 3.79 \cdot 10^4\ \tau$ and $R_{f_{coal,2}} = 1.70 \cdot 10^4\ \tau$ respectively. The black dashed line marks the intersection of the two linear fits at $t_{\mathrm{MD}} = t_c = 18.1 \cdot 10^4\ \tau$.

initial state in the MD model. Consequently, the evolution could be artificially accelerated until the droplets have merged. However, additional simulations with initial droplet profiles taken from droplets equilibrated within the TF model at the same peak distance were not able to confirm this hypothesis and essentially the same results were obtained.

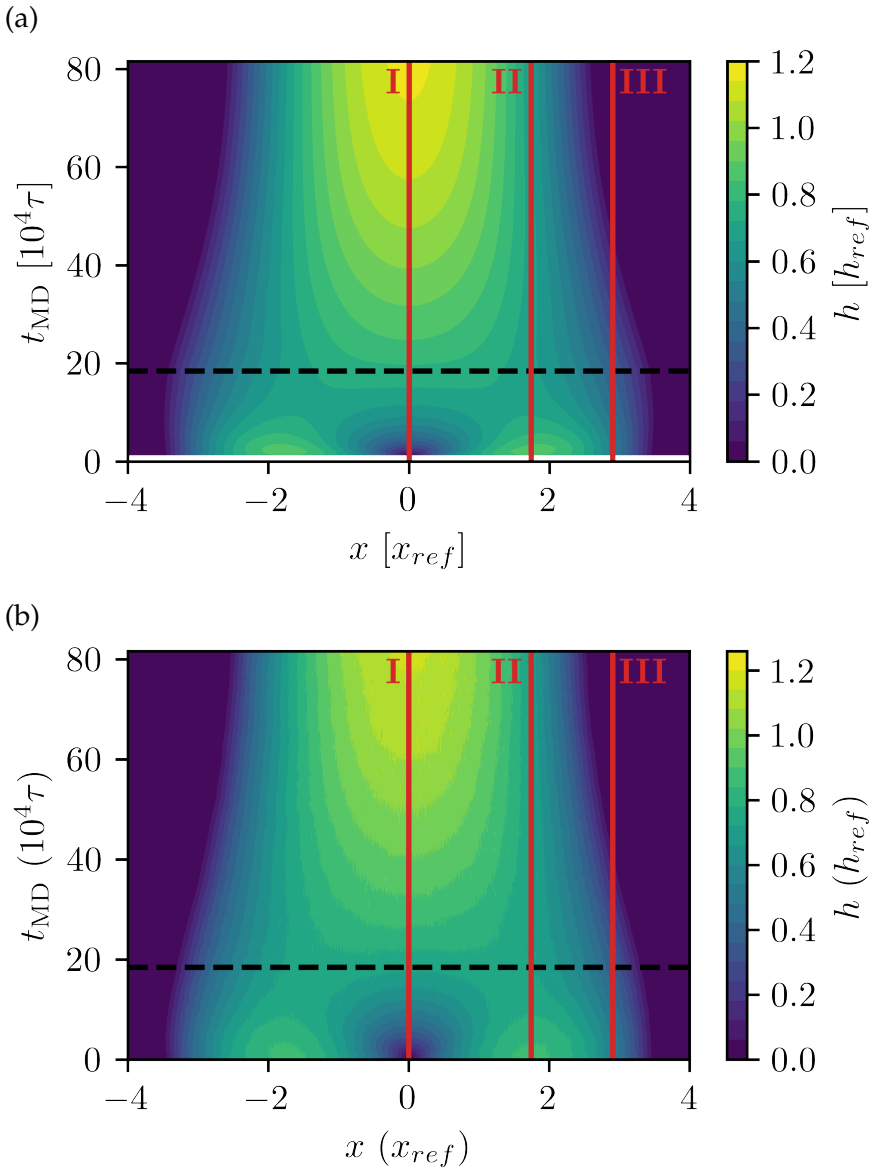

Figure 4.15: Space-time plots showing the coalescence of two ridges in the TF and the MD model in (a) and (b) respectively. The black dashed line is where the TF time scale is split and the linear fits in Fig. 4.14 intersect. The height is scaled just as in Section 4.3.

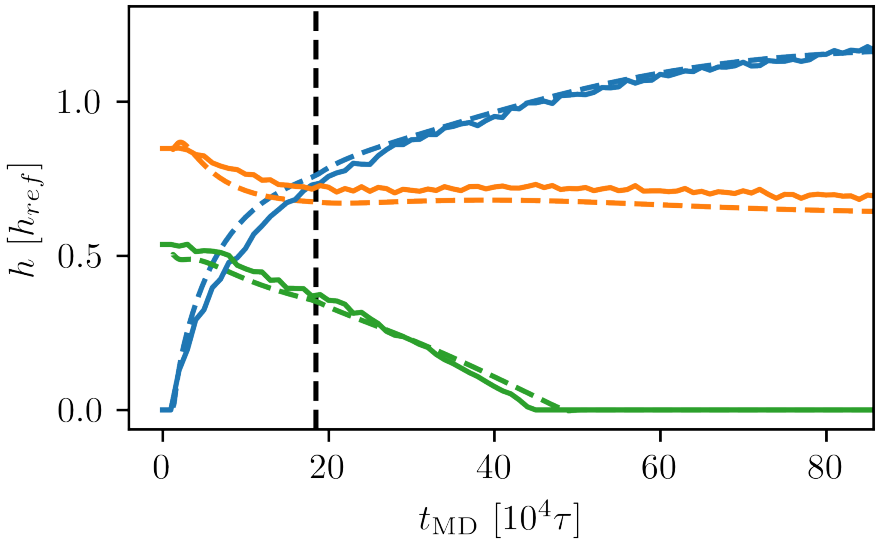

Figure 4.16: Three characteristic height profiles along the marked lines I (blue), II (orange) and III(red) as shown in Fig. 4.15. The height profiles extracted from the MD model are represented with solid lines, whereas the height profiles from the TF model are dashed. The scaling is the same as in Fig. 4.15. The dashed vertical line marks the time step, where the scaling factor is changed from $R_{f_{coal,1}}$ to $R_{f_{coal,2}}$.

4.5 CONCLUSION

In this chapter, a first step toward the quantitative comparison between the microscopic MD and the mesoscopic TF model for the dynamics of liquid droplets was presented. In a first step, the parameters responsible for the substrate wettability in the respective models are mapped for equilibrium droplets via the rFWHM. Thereby, a mapping between the spatial quantities is achieved. In the second step, the general approach for the mapping of the time scales based on matching the quantity K, which depends on the droplet shapes, is applied. The applicability of the presented approach is shown thoroughly for two examples, a droplet on a homogeneous, switchable substrate and the coalescence of two droplets. It has been demonstrated, that intermediate steps in the evolution are in good agreement. This implies, that the same path in phase space is taken in both models. This can be attributed to the reliable mapping of the parameters ϵ_w and ρ responsible for the wettability in their respective models.
Note that the presented mapping can always be applied, as long as one stays within the limits of the TF models, i. e. low contact angle and concept of a precursor film. If one keeps the limits in mind, computational resources can be saved, because it enables one to accurately find the parameter range of interest in the TF model and perform simulations on the mesoscopic scale, while still featuring the same quantitative non-equilibrium time evolution. The other direction is also possible,

e. g. some interesting behavior is found within the TF model and the MD model can provide microscopic insights into the dynamics. The presented approach is not specially tailored to the employed thin-film model. An application of the presented mapping approach for a continuum model, which allows for larger contact angles (e. g. macroscopic boundary element method [80]), is also possible. Mapping to continuum models additionally promises fruitful results with the help of bifurcation analysis, which can help predict onsets of instabilities or explore large parameter spaces systematically along stable branches.

The time mapping for the switching simulations indicates that the resulting mapping does not depend on the initial wettability to a very good approximation. This is indeed a promising result, confirming the ability of the TF approach to reproduce the microscopic results. Interestingly, two relevant deviations from a very simple mapping behavior could be observed. First, the factor R between both time scales slightly depends on the final wettability. Second, in the case of coalescence, a non-linear relation between time scales was found. These observations suggest that, e.g., the mobility or the disjoining pressure may need to be adapted for an even closer agreement. However, since the equilibrium properties are fully matched in this approach, the deviations are always of order unity.

So far a standard choice of mobility and disjoining pressure (cf. Refs. [28, 29] among others) was used and the most important characteristics of the disjoining pressure were matched to the MD model, i. e. the minimum of the interface potential was correct, the precursor film height was chosen adequately, and the wetting regime was correctly mirrored by the employed disjoining pressure. In the future, this approach could be extended to a thin-film model with a fine-tuned disjoining pressure. Literature provides ample opportunities to extract the disjoining pressure directly from microscopic models, which enables comparisons between models in the static case [58–61, 109–112]. In contrast to the calculation of the disjoining pressure, one needs to consider dynamics to be able to extract information about the mobility from MD models. Here, a cubic mobility was used, which can be derived from no-slip boundary conditions. A precise mobility extracted from microscopic models promises to improve the TF description of an MD model. However, it is not clear yet how this can be done.

To sum up, a generic approach for the mapping of two models on different scales was presented. The mapping procedure has virtually no requirements for the involved models, which makes it a versatile approach if characteristic times or other quantities necessary for a temporal mapping are not easily and reliably accessible.

5

WETTING DYNAMICS UNDER PERIODIC SWITCHING

In the previous chapter, a step toward quantitative comparisons of a microscopic MD model and a mesoscopic MD model has been made. As an example of the procedure, the adaptation of a single droplet to a new substrate wettability and the coalescence of two droplets was analyzed. In general, the spreading and relaxation of a droplet are well studied in simple topologies with simple liquids [97, 113, 114]. Even on chemically heterogeneous substrates [115] or porous substrates [116], droplet spreading can be described accurately. Literature on coalescence is also readily available [117, 118].

In this chapter, the behavior of a droplet on a homogeneous substrate, which is switched between two wettabilities for a large range of switching frequencies, is characterized. A particular focus is on the dependence of the wetting behavior on the switching frequency. Results via particle-based molecular dynamics simulations and a continuum thin-film model are found to be consistent. With the help of a simple model called the molecular kinetic theory of wetting (MKT) [27] analytical calculations give additional insights into the underlying mechanisms. The MKT already proved successful in the case of dynamic wetting [97, 119, 120]. The materials enabling switchable substrates have been developed only recently and opened up this direction of research. Examples of surfaces with such properties can be found in [16, 17, 20, 23–25]. Multi-scale approaches are especially suited to describe such problems theoretically due to the inherently involved multiple time scales.

This chapter is organized as follows: In Section 5.1 theoretical preliminaries add to the theoretical background in Chapter 2. In particular, the differences in the mapping approach compared to the previous chapter are explained. The Section 5.2 describes the basics of the MKT, while also introducing approximations and notations used in the subsequent analytical description. For a quantitative comparison to the MKT relevant input parameters need to be extracted from other models as presented in Section 5.3. First, a single switch is examined in Section 5.4 before the dynamics of a droplet on a periodically switched substrate obtained from the three methods (MD, TF, MKT) are compared in Section 5.5. The results are then summarized in Section 5.6.

This chapter is closely based on the following publication:

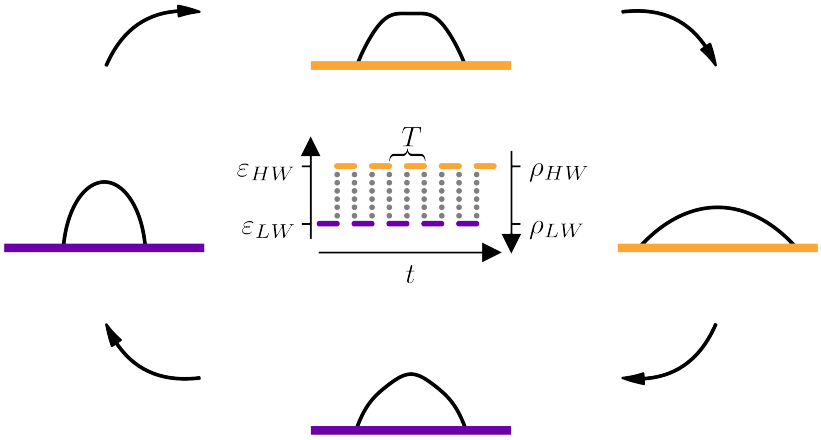

Figure 5.1: Schematic of the periodic switching procedure. The droplet states, shown on the left and the right, respectively, correspond to the situation directly before switching to the other wettability (from violet to orange or vice versa). For very long switching periods T, they are the respective equilibrium states, otherwise, they are non-equilibrium states. The top and bottom droplets express intermediate non-equilibrium states after the switching process. The central panel shows, how the parameters, responsible for the substrate's wettability in MD and TF models, change with time (HW: high wettability; LW: low wettability).

[1] L. Topp, M. Stieneker, S. V. Gurevich and A. Heuer. "Wetting dynamics under periodic switching on different scales: characterization and mechanisms." In: *Soft Matter* (2022). DOI: 10.1039/D2SM01023B.

5.1 THEORETICAL PRELIMINARIES

The same simulation setup as presented in Chapter 4 is used here as well. The schematic in Fig. 5.1 visualizes the resulting behavior when periodic switching is applied. To measure contact angles for equilibrium as well as non-equilibrium height profiles a variety of methods is available. One common method is to perform a circular fit to the data and obtain the contact angle from the tangent at the contact line [72, 73]. Directly computing the tangent at a specific height is also used commonly [71]. For the MD simulations, a circular fit is used to compute contact angles in this chapter.

In the TF model, the contact region exhibits a smooth transition to the precursor film and there is no sharp contact line. Also, the underlying lubrication approximation makes droplets in the TF model deviate from a strict spherical cap shape. Thus, contact angle measurements

in the TF model are finicky. Even the method for the measurement can make a difference [108]. Instead of direct contact angle measurements, the *relative full width at half maximum* (rFWHM) is used, which is the width at half maximum in relation to the drop height. This measure can be determined stably and does not depend on the contact region. Based on the assumption of a circular cap shape the rFWHM can be related to the contact angle. Starting from the relation

$$r^2 = \left(\frac{\sigma}{2}\right)^2 + \left(r - \frac{h}{2}\right)^2, \tag{5.1}$$

which holds for a spherical cap, where h is the height, r the radius of the droplet and σ the width at half height the radius r can be expressed as

$$r = \frac{1}{4h}(\sigma^2 + h^2). \tag{5.2}$$

Further, basic trigonometry yields

$$\cos(\theta) = 1 - \frac{h}{r} \tag{5.3}$$

with the contact angle θ. By inserting Eq. (5.2) into Eq. (5.3) one gets

$$\cos(\theta) = 1 - \frac{h}{\frac{1}{4h}\left(\sigma^2 + h^2\right)} \tag{5.4}$$

and finally

$$\cos(\theta) = 1 - \frac{4}{\frac{1}{\mathrm{rFWHM}^2} + 1}. \tag{5.5}$$

is obtained with the definition rFWHM = h/σ. Note that the result of Eq. (5.5) can be reproduced by a circle fit with an appropriately chosen fitting range and that the same method could be used for the MD data. However, due to the inherent noise, the use of a circular fit increases the accuracy without involving a systematic shift. In experiments a fit dependent on the whole droplet profile is common for similar reasons [121, 122].

Comparable to the procedure from Chapter 4 the mapping between the MD and the TF model is done in two steps. The first step to obtain an invertible mapping $\epsilon_w \mapsto \rho$ is identical to Chapter 4. To avoid confusion between these parameters in the following only the relevant ϵ_w values are mentioned and mean the corresponding ρ value when showing TF results. In the second step, the time scales are determined by the relaxation of $\cos\theta(t)$ for a switching process from ϵ_1 to ϵ_2. As the relaxation of $\cos\theta$ does not necessarily have an exponential shape, the time evolution is fitted with a stretched exponential function

$$f(t) = f_\infty + (f_0 - f_\infty)\exp\left(-\left(\frac{t}{\tau_0}\right)^\beta\right). \tag{5.6}$$

Then, the relaxation time of $f(t)$ is defined as

$$\tau_{rel} = \frac{\tau_0}{\beta}\Gamma\left(\frac{1}{\beta}\right) \tag{5.7}$$

where Γ is the gamma function. Like this, the normalized times scaled by the relaxation time τ_{rel} can be compared.

5.2 MOLECULAR KINETIC THEORY OF WETTING

The MKT expresses how the deviation of a non-equilibrium contact angle to its equilibrium value gives rise to a contact line velocity of the droplet, which promotes the approach to equilibrium [27]. It accounts for the jumping processes of particles in the contact line region of a moving droplet. This yields an equation that relates the velocity of the three-phase contact line v_{cl} to the time-dependent cosine of the contact angle $\cos(\theta(t))$

$$v_{cl} = \frac{\gamma}{\zeta}(\cos(\theta_{eq}) - \cos(\theta(t))). \tag{5.8}$$

Here, γ is the surface tension, ζ a friction coefficient and θ_{eq} the equilibrium contact angle. In general, the ratio γ/ζ can be obtained by measuring the contact line velocity in dependence of the contact angle. On a deeper level, for the particle-based model, the values of γ and ζ can be separately estimated from additional MD simulations. Note that the MKT approach accounts for jumping processes in the contact line region but not for hydrodynamics. This should be considered especially when comparing MKT results to TF results where hydrodynamic effects play an important role. However, in general, it is possible to compare MKT and TF data on an empirical level but deviations between both approaches can be expected. It is also possible to combine the MKT approach with the hydrodynamic equations as shown in the model by Petrov and Petrov [123].

To derive analytical expressions based on the MKT Eq. (5.8) the equation needs to be reformulated. For a circular cap the trigonometric relation

$$r = \sqrt{2A}\frac{\sin(\theta)}{\sqrt{(2\theta - \sin(2\theta))}} = \sqrt{2A}f(\theta) \tag{5.9}$$

between the half chord length r, the central angle θ of a circular segment and the area of the circular segment A holds. Here, r is the radius of a droplet on a surface and θ is the contact angle. With the help of Eq. (5.9), the contact line velocity can be expressed as

$$v_{cl} = \frac{dr}{dt} = \sqrt{2A}\frac{df}{d\theta}\frac{d\theta}{dt} = -\sqrt{2A}\frac{df}{d\theta}\frac{1}{sin(\theta)}\frac{d\cos(\theta)}{dt} \tag{5.10}$$

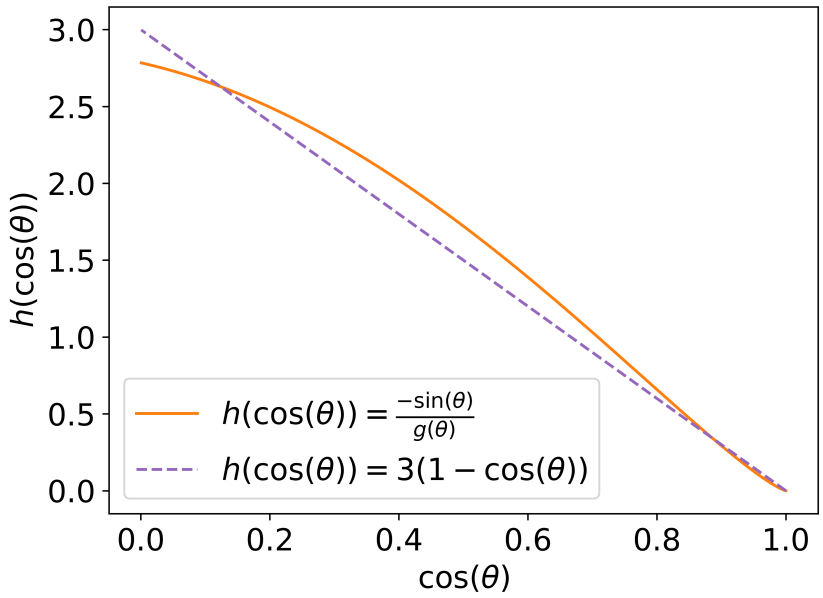

Figure 5.2: The expression $\frac{-\sin(\theta)}{g(\theta)}$ in comparison with $3(1-\cos(\theta))$ plotted versus $\cos(\theta)$.

where

$$g(\theta) = \frac{df}{dt} = \frac{\cos(\theta)}{\sqrt{2\theta - \sin(2\theta)}} - \frac{\sin(\theta)(1-\cos(2\theta))}{\sqrt{2\theta - \sin(2\theta)^3}}. \tag{5.11}$$

With the help of Eq. (5.10) the MKT equation (5.8) can be rewritten as

$$\frac{d}{dt}\cos(\theta) = -k_1 \frac{\sin(\theta)}{g(\theta)}(\cos(\theta_{eq}) - \cos(\theta)) \tag{5.12}$$

with $k_1 = \frac{k_0}{\sqrt{2A}}$. This is now an ordinary differential equation for the cosine of the contact angle, which can be compared to other models easily. As can be seen in Fig. 5.2 $\frac{-\sin(\theta)}{g(\theta)}$ can be approximated as $3(1-\cos(\theta))$ reasonably well. Thus, Eq. (5.12) can be rewritten for intermediate changes in contact angles as

$$\frac{d}{dt}\cos(\theta) = k_2(1-\cos(\theta))(\cos(\theta_{eq}) - \cos(\theta)) \tag{5.13}$$

with $k_2 = 3k_1 = 3\frac{\gamma}{\zeta}/\sqrt{2A}$. For small changes in contact angle, this can be even further reduced to

$$\frac{d}{dt}\cos(\theta) = k_3(\cos(\theta_{eq}) - \cos(\theta)) \tag{5.14}$$

where $k_3 = k_2(1-\cos(\theta_{eq}))$ since $\cos(\theta)$ can be substituted by the constant $\cos(\theta_{eq})$. In Figures 5.3 and 5.4 the two approximations and the solution from Eq. (5.12) are plotted for a single switching event

and periodic switching. Fig. 5.4 shows nicely that the approximation $\cos(\theta) \approx \cos(\theta_{eq})$ collapses for higher contact angle differences. The approximation for intermediate contact angles in Eq. (5.13) agrees with Eq. (5.12) for both contact angle differences as shown in Figs. 5.3 and 5.4 reasonably well.

5.2.1 *Analytic description of the single switching process*

So far the differential equations have only been solved numerically. In this section, an analytical expression is derived to describe the evolution of $\cos(\theta)$ upon a single instantaneous switch in wettability, i. e. an instantaneous change in $\cos(\theta_{eq})$. For the analytical solution x and x_{eq} substitute $\cos(\theta)$ and $\cos(\theta_{eq})$ for better readability. After separation of variables Eq. (5.13) can then be written as

$$\frac{dx}{(1-x)(x-x_{eq})} = -k_2 dt. \tag{5.15}$$

With the help of the relation

$$\frac{1}{(1-x)(x-x_{eq})} = \frac{1}{1-x_{eq}}\left[\frac{1}{1-x} + \frac{1}{x-x_{eq}}\right] \tag{5.16}$$

the solution for the differential equation

$$-\ln(1-x) + \ln(x-x_{eq}) = -k_2(1-x_{eq})t + C \tag{5.17}$$

with the integration constant $C = -\ln(1-x_0) + \ln(x_0 - x_{eq})$ is obtained. Note that with the abbreviated notation $k_3 = k_2(1-x_{eq})$ holds analogously to Eq. (5.14). After applying the exponential function on both sides Eq. (5.17) reads

$$\frac{x-x_{eq}}{1-x} = \frac{x_0 - x_{eq}}{1-x_0}\exp(-k_3 t), \tag{5.18}$$

which can be solved for $x(t)$. After a short calculation, one obtains

$$x(t) = \frac{x_{eq} + \epsilon(t)}{1+\varepsilon(t)} \tag{5.19}$$

with

$$\varepsilon(t) = \frac{x_0 - x_{eq}}{1-x_0}\exp(-k_3 t). \tag{5.20}$$

For the normalized relaxation function $y(t) = (x(t) - x_{eq})/(x_0 - x_{eq})$ this yields

$$y(t) = \frac{(1-x_{eq})\exp(-k_3 t)}{1 - x_0 + \exp(-k_3 t)(x_0 - x_{eq})}. \tag{5.21}$$

(a)

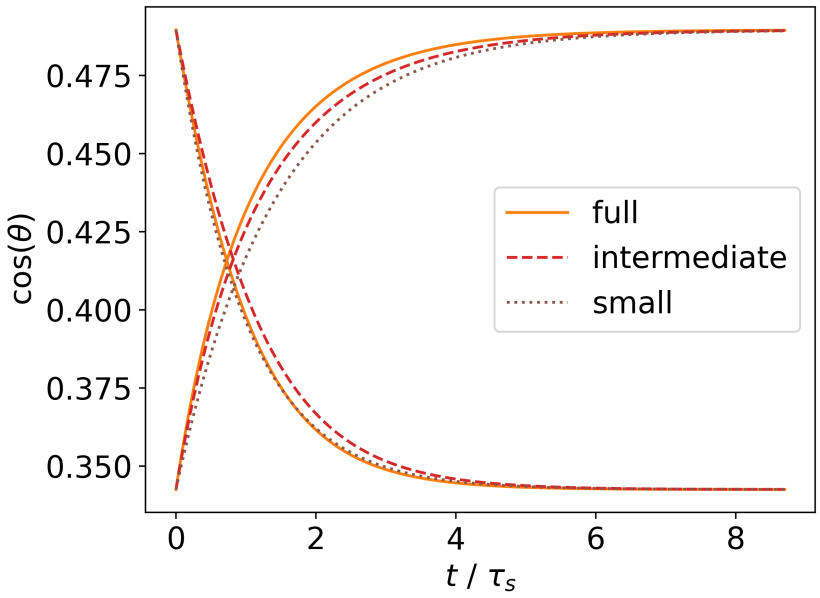

(b)

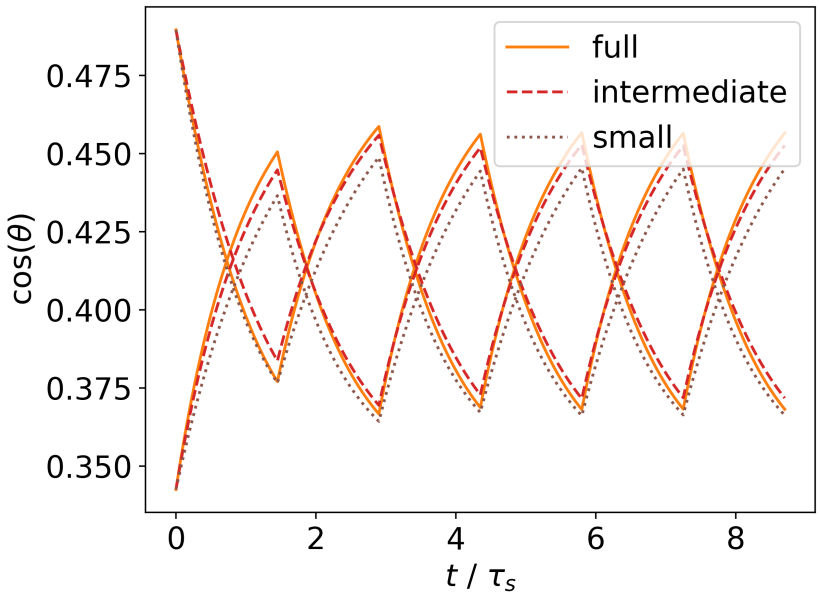

Figure 5.3: Evolution of $\cos(\theta)$ for the different approximations of the MKT for (a) a single switch and (b) periodic switching between $\epsilon_w = 0.632$ and $\epsilon_w = 0.671$. (full: Eq. (5.12), intermediate: Eq. (5.13); small: Eq. (5.14))

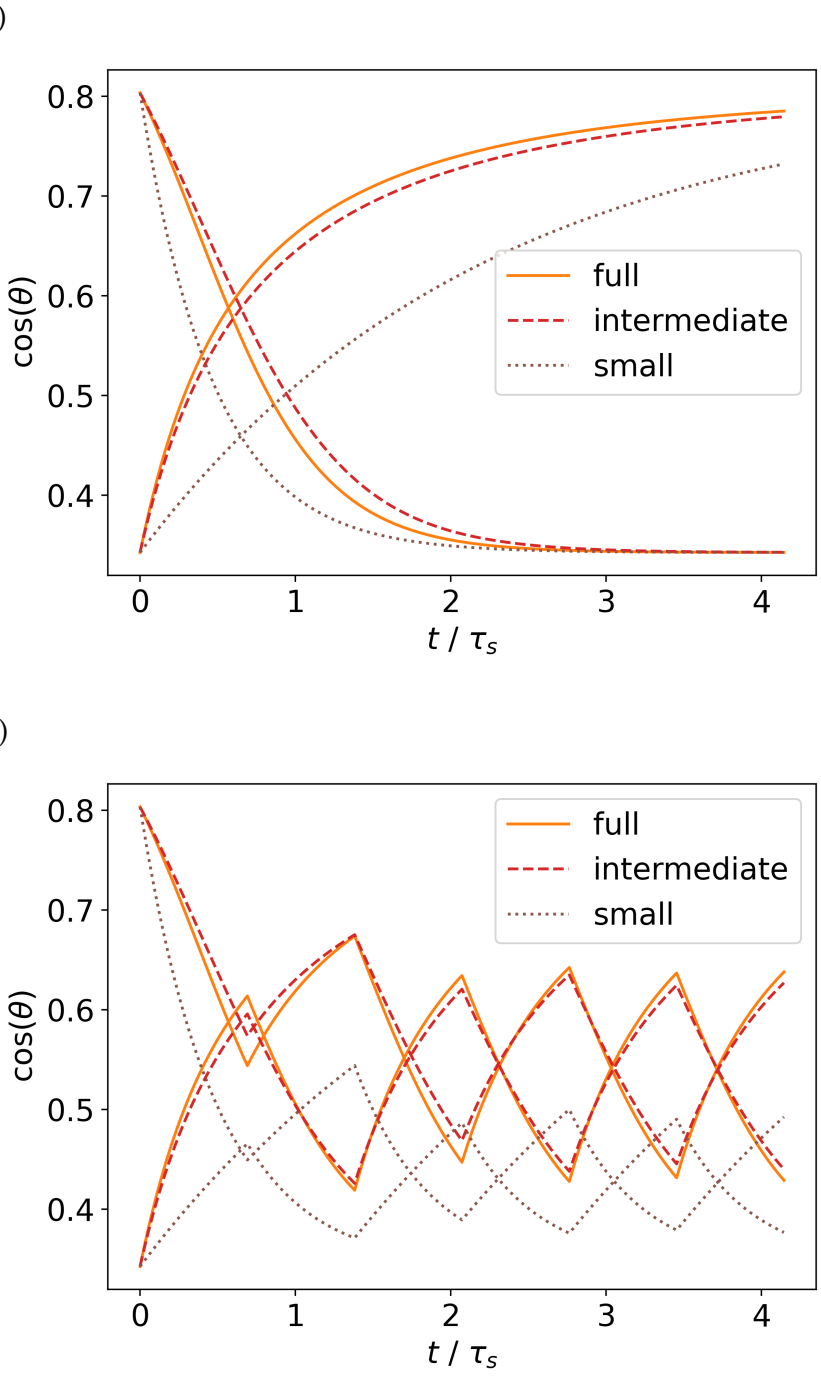

Figure 5.4: Evolution of $\cos(\theta)$ for the different approximations of the MKT for (a) a single switch and (b) periodic switching between $\epsilon_w = 0.632$ and $\epsilon_w = 0.762$. (full: Eq. (5.12), intermediate: Eq. (5.13), small: Eq. (5.14))

The normalization ensures the properties $y(t = 0) = 1$ and $y(t = \infty) = 0$. For small but finite differences of $x_0 - x_{eq}$ (as implied by a small wettability difference $\Delta\epsilon_w$), the expression can be expanded in $\epsilon(t)$. Taking into account terms until ϵ^2 this yields:

$$\begin{aligned} x(t) &= [x_{eq} + \varepsilon(t)[1 - \varepsilon(t) + \varepsilon(t)^2 + ...] \\ &\approx x_{eq} + (1 - x_{eq})(\varepsilon(t) - \varepsilon(t)^2) \end{aligned} \tag{5.22}$$

Consequently, the normalized function $y(t)$ can be written as

$$y(t) \approx \frac{1 - x_{eq}}{1 - x_0} \left[\exp(-k_3 t) - \frac{x_0 - x_{eq}}{1 - x_0} \exp(-2k_3 t) \right]. \tag{5.23}$$

up to second order.

5.2.2 *Analytic description of the periodic switching process*

In the limit of small wettability changes $x(t)$ is always close to x_{eq} so that the prefactor $1 - x(t)$ in Eq. (5.13) can be approximated as $1 - x_{eq}$, yielding

$$\frac{d}{dt} x(t) = k_3 (x_{eq} - x(t)), \tag{5.24}$$

with $k_3 = k_2(1 - x_{eq})$. Indeed, this is the same definition of k_3 as resulting from the exact calculation in Eq. (5.21) automatically. Again, the normalized version is considered so that Eq. (5.24) reads

$$\frac{d}{dt} y(t) = -k_{3,i} (y - a_i), \tag{5.25}$$

where $k_{3,i}$ and $a_i \in \{0, 1\}$ are the prefactor and the normalized equilibrium contact angle, respectively.

The wettability is switched periodically with period T. The switching is instantaneous between two wettabilities. Initially, at $t = 0$, the droplet is assumed to be equilibrated at the higher wettability (corresponding to the normalized contact angle $a = 1$). For the first half-period ($i = \downarrow$) the substrate is at the lower wettability $a_\downarrow = 0$. The subscript denotes that the wettability is switched towards the lower wettability. In the second half-period ($i = \uparrow$) the substrate is at the higher wettability $a_\uparrow = 1$. The schematic in Fig. 5.1 visualizes the switching procedure. After a straightforward but slightly tedious analysis (see Appendix B) the normalized cosine of the contact angle averaged over one period can be derived as

$$\langle y(n) \rangle = y_{plateau} \pm \exp\left(-K_3 (n + \frac{1}{2}) T/2 \right) \cdot \hat{y}_\pm \tag{5.26}$$

with $K_3 = k_{3,\downarrow} + k_{3,\uparrow}$. The quantity $\langle y(n) \rangle$ denotes the average of $y(t)$ between $t = nT$ and $t = (n + 1)T$. The $\pm$ distinguishes an initial higher

wettability (+) from an initial lower wettability (−). The plateau value $y_{plateau}$, obtained in the limit of an infinite number of switching cycles n, is given by

$$y_{plateau} = \frac{1}{2}\left\{ \frac{(1-\exp(-k_{3,\uparrow}T/2))(1-\exp(-k_{3,\downarrow}T/2)}{1-\exp(-K_3T/2)} \left(\frac{1}{k_{3,\downarrow}T/2} - \frac{1}{k_{3,\uparrow}T/2}\right) + 1 \right\}. \tag{5.27}$$

This expression is independent of the initial wettability. In the limit case for very fast switching, i.e. small T, Eq. (5.27) boils down to

$$y_{plateau} = \frac{k_{3,\uparrow}}{k_{3,\downarrow}+k_{3,\uparrow}} - \frac{k_{3,\uparrow}-k_{3,\downarrow}}{96(k3,\downarrow+k_{3,\uparrow})} k_{3,\downarrow}k_{3,\uparrow}T^2. \tag{5.28}$$

The amplitude $\hat{y}_\pm$ depends on the initial condition. Starting with the higher wettability, the amplitude $\hat{y}_+$ turns out to be

$$\begin{aligned} \hat{y}_+ = \exp(K_3T/4)&\frac{\exp(-k_{3,\uparrow}T/2) - \exp(-K_3T/2)}{1-\exp(-K_3T/2)} \\ \cdot &\left[\frac{1}{2k_{3,\downarrow}T/2} \cdot (1-\exp\left(-k_{3,\downarrow}T/2\right)) \right. \\ &\left. + \exp\left(-k_{3,\downarrow}T/2\right) \frac{1}{2k_{3,\uparrow}T/2} \left(1-\exp\left(-k_{3,\uparrow}T/2\right)\right) \right]. \end{aligned} \tag{5.29}$$

$\hat{y}_-$ can be obtained by exchanging $k_{3,\downarrow}$ with $k_{3,\uparrow}$. For the limit of very fast switching, i.e. $T \to 0$, this expression reduces to $\hat{y}_+ = (1 - y_{plateau})$ and $\hat{y}_- = y_{plateau}$, respectively. Although this calculation has been performed for small changes in the wettability, the range of applicability can be increased. This can be achieved by substituting $k_{3,i}$ by $\tilde{k}_{3,i} = k_1 \sin(\langle\theta\rangle)/g(\langle\theta\rangle)$, which is basically the prefactor of the original MKT Eq. (5.12) for an averaged contact angle θ. Defining $\langle\theta\rangle$ via $\cos\langle\theta\rangle = (1/2)(\cos\theta_{eq}(\epsilon_{HW}) + \cos\theta_{eq}(\epsilon_{LW}))$ is convenient as it is the average angle for large switching times T. Note that for $T \to 0$ the value of $y_{plateau}$ is not sensitive to this choice because it only depends on the ratio of the k_1-values. k_1 depends on the wettability of the substrate implicitly via the value of ζ.

5.2.3 *Properties of the relaxation process*

In this section, the analytical results from the previous sections are used to predict whether the evolution of $\cos(\theta)$ after a single instantaneous switch in wettability is stretched or compressed. The parameter β of the stretched exponential function from Eq. (5.6) is capable of indicating whether the deviation from an exponential evolution is compressed ($\beta > 1$) or stretched ($\beta < 1$).

For reference data from the MD and TF model the evolution of $\cos(\theta)$ is fit with the stretched exponential function shown in Eq. (5.6). The TF data and the corresponding fit functions are shown in Fig. 5.5. In Fig. 5.6 the MD data is shown along MKT results based on Eq. (5.12). The stretched exponential function is almost indistinguishable from the MKT results. Expect for the anticipated noise also the MD data is reproduced well by the stretched exponential function. Although the TF data is not perfectly described by the fit the quantitative differences are small. The resulting β-values for the MD simulations, for the TF analysis and for the MKT equations as shown in Figs. 5.5 and 5.6 are listed in Table 5.1. One consistently observes a stretched exponential behavior ($\beta < 1$) when increasing the wettability upon switching and a compressed exponential behavior ($\beta > 1$) in the opposite case.

Table 5.1: Values of β obtained from a fit with a stretched exponential function according to Eq. (5.6) to the data for a single switching event from ϵ_1 to ϵ_2 in MD, MKT and TF simulations.

ϵ_1	ϵ_2	β_{MD}	β_{MKT}	β_{TF}
0.632	0.762	0.87	0.73	0.68
0.762	0.632	1.68	1.42	2.05

The analytical expressions based on the MKT derived in Section 5.2.1 can help to determine whether this is a coincidence or a systematic observation. Starting from the definition of the n-th moment of the normalized relaxation function $y(t)$

$$\langle \tau^n \rangle = \frac{\int_0^\infty t^n \cdot y(t) \mathrm{d}t}{\int_0^\infty y(t)} \tag{5.30}$$

the quantity

$$\frac{\langle \tau^2 \rangle}{2\langle \tau \rangle^2} \tag{5.31}$$

which is equal to one for a purely exponential function $y(t)$, can be computed. If this quantity is greater than 1, it implies a compressed exponential function ($\beta > 1$) whereas in the opposite case it describes a stretched exponential function ($\beta < 1$).

Using the expression from Eq. (5.21) in Eq. (5.31) one gets

$$\frac{\langle \tau^2 \rangle}{2\langle \tau \rangle^2} = \frac{\left(1 - \frac{B}{8}\right)\left(1 - \frac{B}{2}\right)}{\left(1 - \frac{B}{4}\right)^2} = 1 - \frac{B}{8(1 - \frac{B}{4})^2}, \tag{5.32}$$

where $B = \frac{x_0 - x_{eq}}{1 - x_0}$. For switching from higher to lower wettability, $x_0 > x_{eq}$ holds, which implies $B > 0$. Consequently, the expression

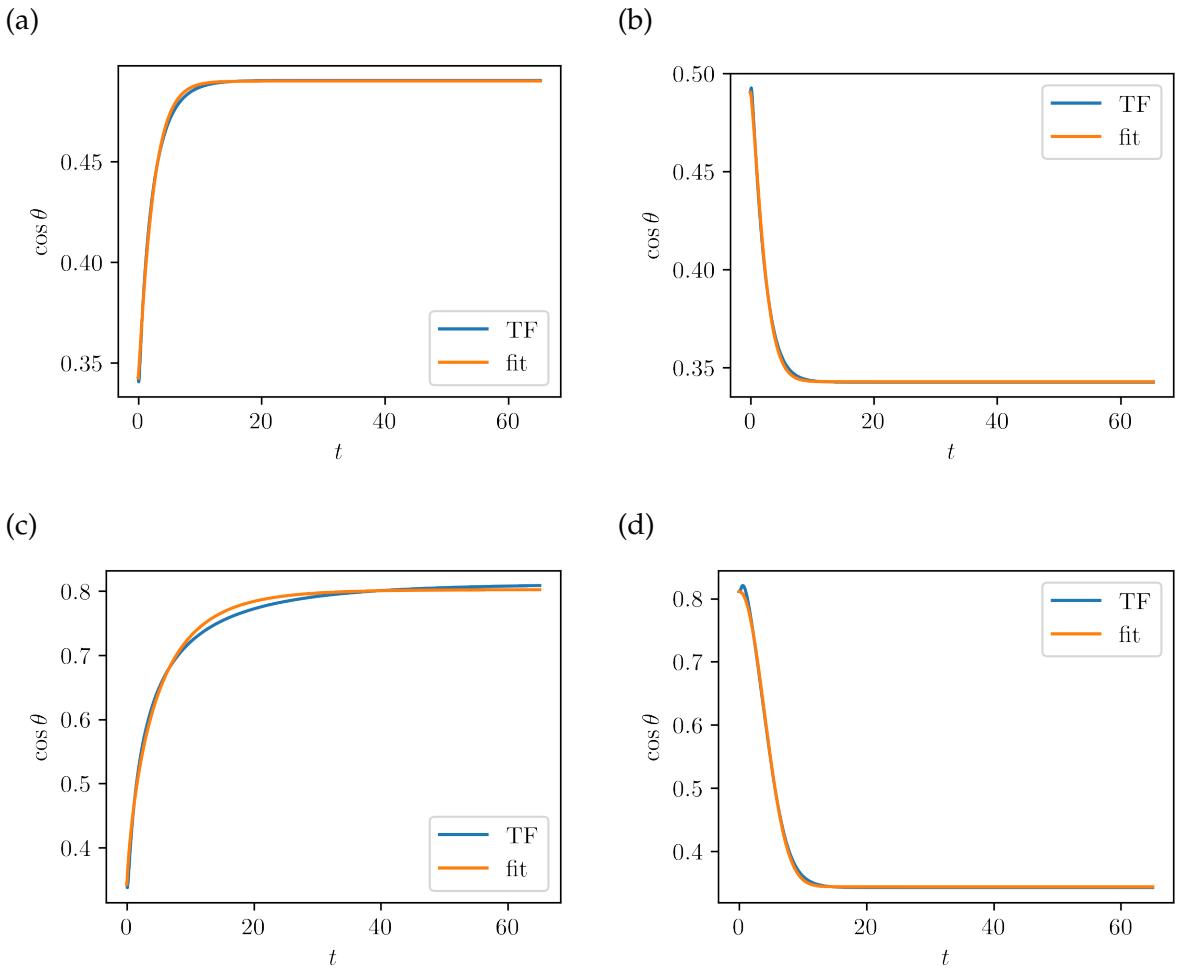

Figure 5.5: Relaxation of $\cos(\theta)$ after an instantaneous change in wettability in the TF model for the wettability values corresponding to different changes in interaction strengths $\epsilon_1 \rightarrow \epsilon_2$ in the MD model: (a) 0.632 $\rightarrow$ 0.671, b) 0.671 $\rightarrow$ 0.632, c) 0.632 $\rightarrow$ 0.0.762 and d) 0.762 $\rightarrow$ 0.632.

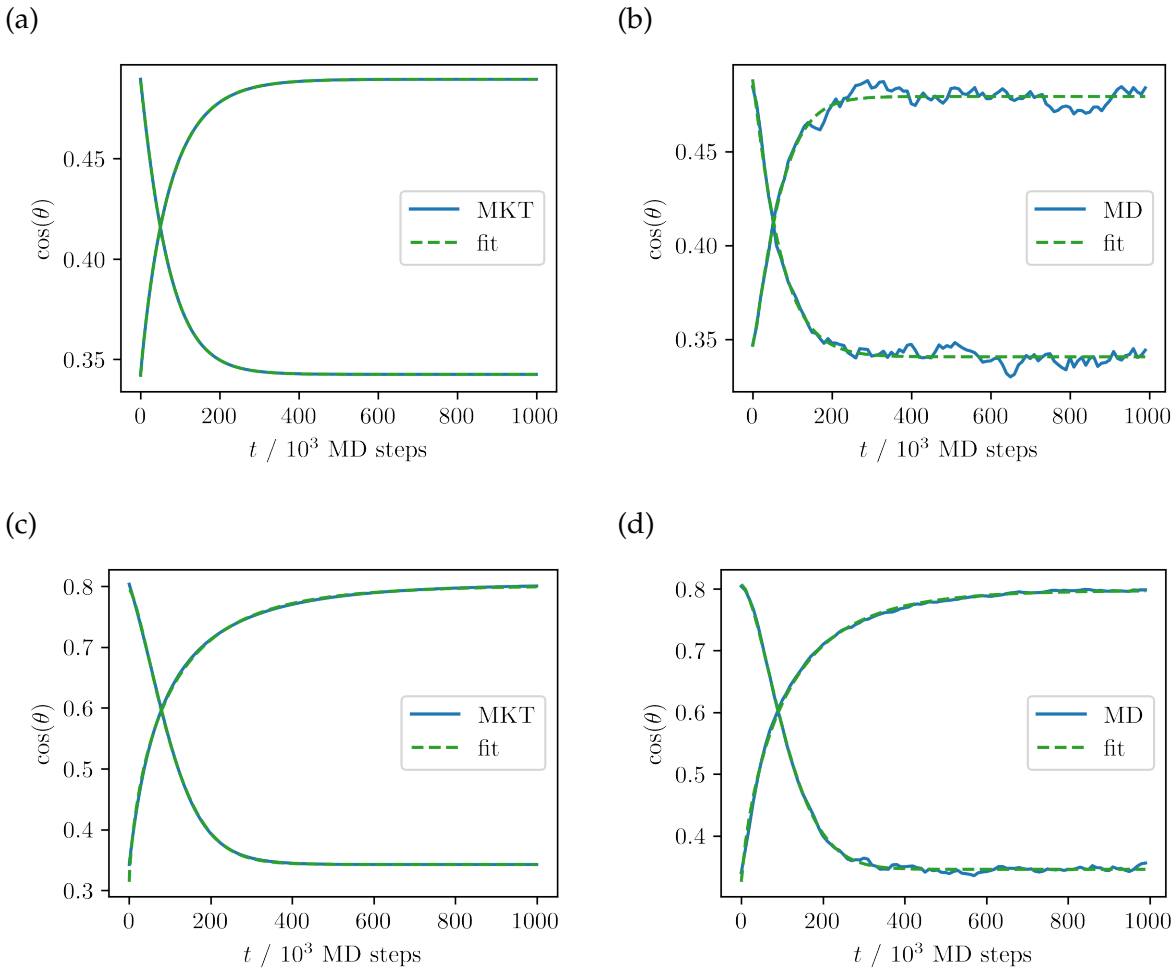

Figure 5.6: Relaxation of $\cos\theta$ after an instantaneous change in wettability in the MD and MKT model for the interaction strengths $\epsilon_1 \leftrightarrow \epsilon_2$: (a) $0.632 \leftrightarrow 0.671$ (MKT), (b) $0.632 \leftrightarrow 0.671$ (MD), (c) $0.632 \leftrightarrow 0.762$ (MKT) and (d) $0.632 \leftrightarrow 0.762$ (MD).

Table 5.2: Values of K_0, n and ζ_R directly calculated from MD simulations.

ϵ	K_0/τ^{-1}	n/σ^{-3}	ζ_R
0.447	$4.62 \cdot 10^{-4}$	0.57	$0.93 \cdot 10^3$
0.548	$3.81 \cdot 10^{-4}$	0.62	$1.23 \cdot 10^3$
0.632	$3.24 \cdot 10^{-4}$	0.66	$1.53 \cdot 10^3$
0.707	$2.76 \cdot 10^{-4}$	0.69	$1.88 \cdot 10^3$
0.742	$2.55 \cdot 10^{-4}$	0.70	$2.07 \cdot 10^3$
0.762	$2.44 \cdot 10^{-4}$	0.71	$2.19 \cdot 10^3$
0.809	$2.40 \cdot 10^{-4}$	0.71	$2.23 \cdot 10^3$
0.775	$2.17 \cdot 10^{-4}$	0.73	$2.51 \cdot 10^3$
0.837	$2.03 \cdot 10^{-4}$	0.74	$2.73 \cdot 10^3$

in Eq. (5.32) has to be smaller than 1 and finally β has to be greater than 1. Analogously $\beta < 1$ follows for the inverse switching direction. This is in accordance with the results from the MD and TF models, as shown in Table 5.1.

5.3 RELATION BETWEEN CONTACT LINE VELOCITY AND CONTACT ANGLE

The friction coefficient ζ appearing in the MKT can be directly computed from quantities calculated from MD simulations as shown by Ruijter, Blake and De Coninck[97] (further on denoted as 'ζ_R' with R for de Ruijter). It can be expressed as

$$\zeta_R = n k_b T / K_0 \lambda, \tag{5.33}$$

where n is the number of adsorption sites per unit area on a solid, K_0 is the equilibrium frequency for particle displacements parallel to the solid and λ is the characteristic length of the displacement. Here, K_0 is determined as the inverse of the time where half of the particles have moved between the first and the second liquid layer in z-direction. The characteristic length of the particle displacement is $\lambda = 1\,\sigma$ since this is the distance between the first two liquid layers over the substrate. The number of absorption sites per unit area n is taken to be the density of the first liquid layer. The measured values of K_0, n and the resulting value of ζ_R via Eq. (5.33) can be found in Table 5.2 for a wide range of ϵ_w values. As shown in Section 2.2.1, $\gamma = (0.477 \pm 0.005)\ \epsilon_f/\sigma^2$ was obtained from the MD simulations and completes the macroscopic quantities to apply the MKT. The resulting ratios ζ_R/γ are shown in Fig. 5.7 in dependence of the squared wetting energy ϵ_w^2 which to a good approximation displays a linear behavior.

Another option to determine ζ is to calculate the slope of a linear fit of the contact line velocity v_{cl} versus $\cos\theta(t)$ (denoted with ζ_{MD} and ζ_{TF} for the MD and the TF model respectively). This slope corresponds to the prefactor γ/ζ of Eq. (5.8) so that ζ_{MD} can be determined by dividing the interface tension by the slope of the fit. Therefore, a droplet was equilibrated on a substrate with a lower solid-liquid interaction ϵ_{LW} and was switched instantaneously to a higher solid-liquid interaction ϵ_{HW} or vice versa. During the relaxation process, the contact angle was measured to calculate $\cos\theta(t)$. As can be seen in Fig. 5.8 (a) the first few data points do not show a linear behavior of the contact line velocity in contrast to the behavior at later time steps which can be attributed to initial dead-time effects as shown later. This is particularly pronounced when switching from ϵ_{HW} to ϵ_{LW}. As a consequence, the first few data points for both switching directions cannot be used for the linear fit to determine ζ_{MD} as indicated by the solid line in the figure.

ζ_{MD} can be determined for multiple pairs of ϵ_{LW} and ϵ_{HW}. The resulting values are shown in Fig. 5.7 (a) where ζ_R/γ and ζ_{MD}/γ are plotted against ϵ_w^2. It shows that ζ increases with increasing ϵ_w since the energy barriers for particle jumps on the surface and thus the friction increases. Also, it emphasizes the applicability of the scheme to calculate ζ_R since the values of ζ_R and ζ_{MD} agree very well. Furthermore, it is notable that within the statistical uncertainties ζ_{MD} does not depend on the switching direction and just reflects the interaction of the droplet with the substrate close to the contact line. This is in accordance with the physical picture of the MKT approach. A deviation from this behavior can be seen for the values of ζ_{TF} plotted against ϵ_w^2 in Fig. 5.7 (b) where ζ_{TF} strongly depends on the switching direction especially for higher values of ϵ_w^2.
Figure 5.8 (b) shows the relation between the contact line velocity v_{cl} and the cosine of the contact angle $\cos(\theta)$ within the TF model for instantaneous switching. Comparable to the MD equivalent in Fig. 5.8 (a) the first data points deviate from a linear dependence of v_{cl} and $\cos(\theta)$ and the later data points can be approximated by a linear function. A slight curvature is notable and indicates more pronounced non-linear behavior. The visualization of the extracted ζ_{TF} values in Fig. 5.7 indicate a mostly linear relation between ζ_{TF} and ϵ_w^2 for smaller values of ϵ_w^2. For higher values of ϵ_w^2 the extracted ζ_{TF} value tends to depend more on the switching direction.
To check whether the MKT is also applicable to the case of periodic switching periodic switching was simulated by first equilibrating a droplet on a substrate with a constant interaction strength of ϵ_{LW} or ϵ_{HW}, respectively. Then, at time $t = 0$ the wettability of the substrate is periodically changed between ϵ_{LW} and ϵ_{HW} each $T/2$ time steps. Figure 5.9 (a) shows the result for such a periodically switched sub-

(a)

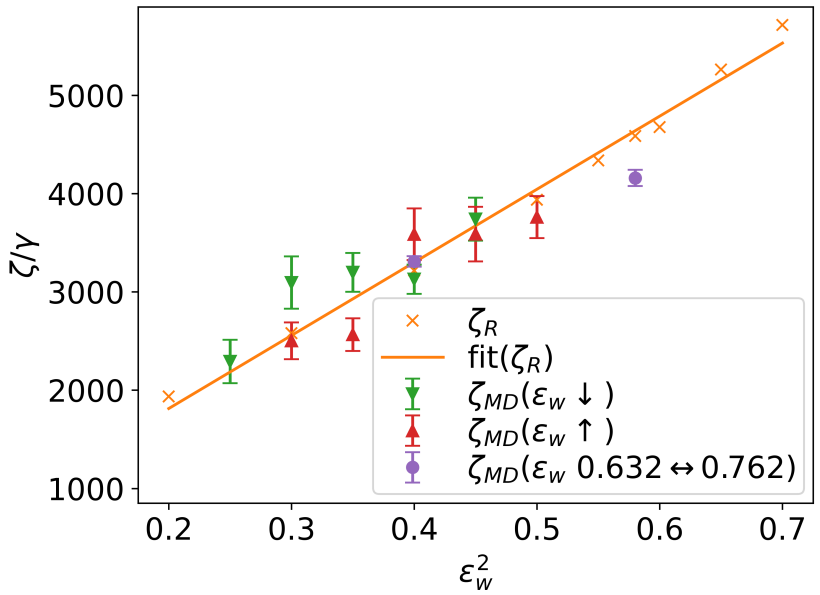

(b)

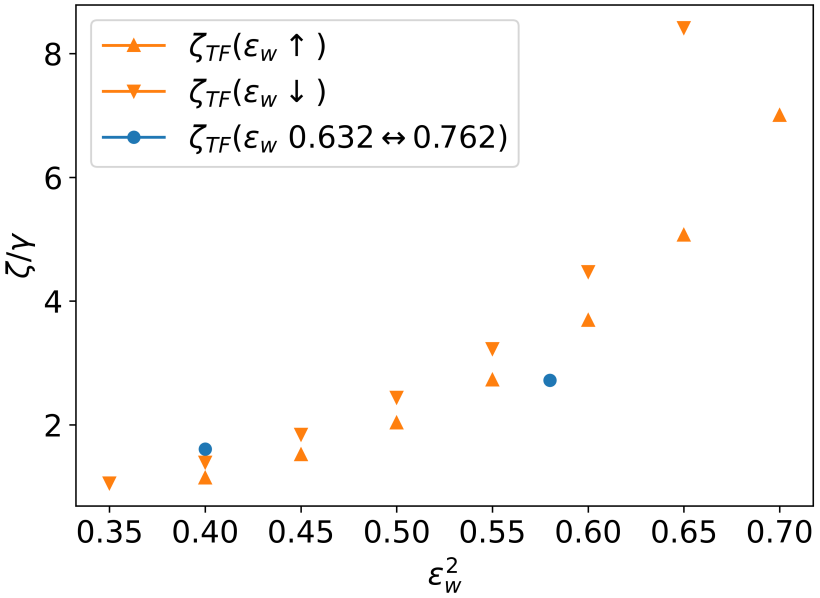

Figure 5.7: (a) Values of ζ_R and ζ_{MD} plotted against ϵ_w^2. The solid line is a linear fit through the values of ζ_R. ▲ and ▼ marks values of ζ_{MD} calculated from simulations where the wettability of the surface is changed by $\Delta\epsilon_w = 0.05$ from a higher wettability ▼ and from a lower wettability ▲, respectively. • marks values obtained from fits of Eq. (5.8) for switching between $\epsilon_w = 0.632$ and $\epsilon_w = 0.762$. The error bars show one standard deviation error. (b) ζ_{TF} plotted against ϵ_w^2 for TF simulations.

(a)

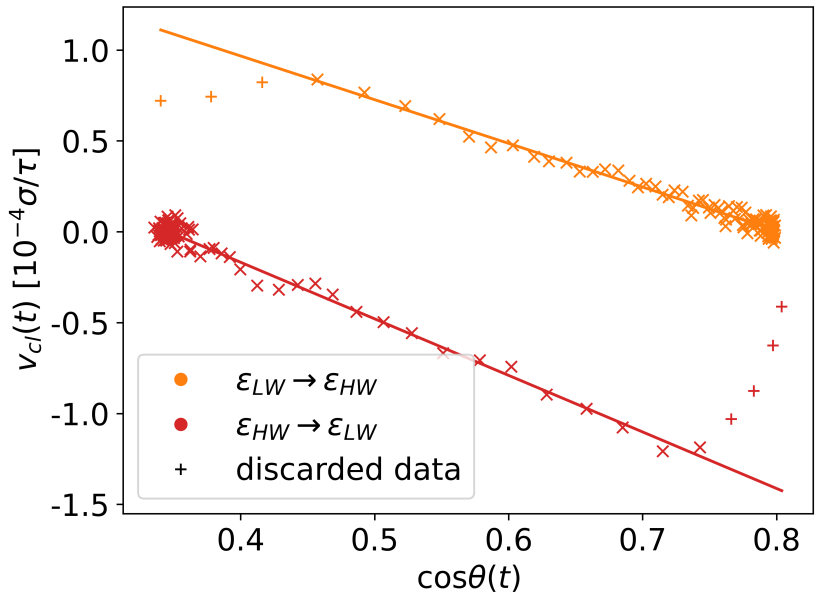

(b)

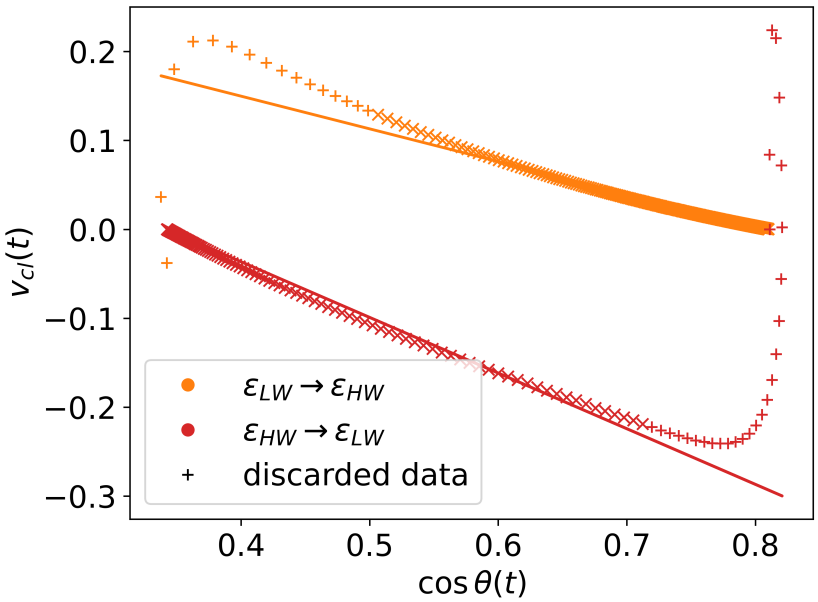

Figure 5.8: Velocity of the contact line v_{cl} plotted against $\cos\theta(t)$ for (a) the relaxation of a droplet on a surface with a wettability change from $\epsilon_{HW} = 0.762$ to $\epsilon_{LW} = 0.632$ and the reverse process in the MD model. A line is fitted to the data to compute ζ_{MD} from its slope according to the MKT theory. The first few data points (plus sign) were discarded for these fits. Data points are spaced equidistantly with $\Delta t = 10^4$ MD steps, (b) TF simulations corresponding to the MD results in (a) with $\Delta t = 0.1$.

(a)

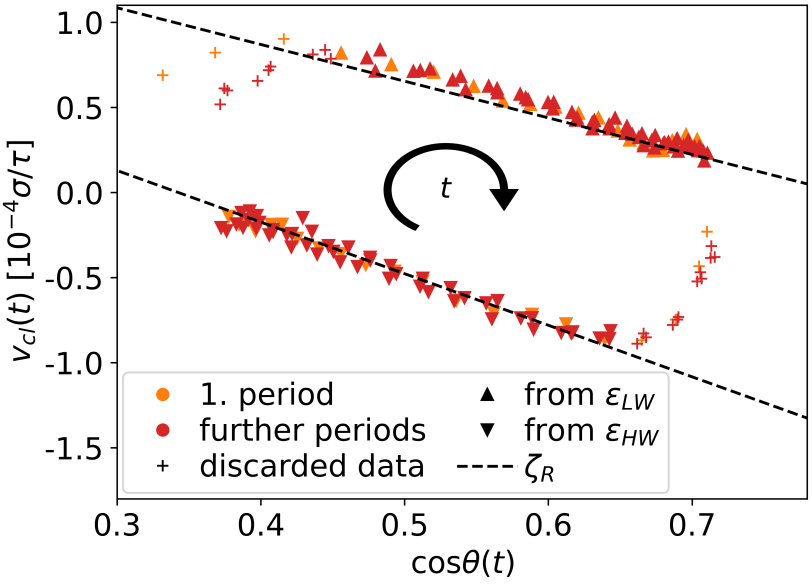

(b)

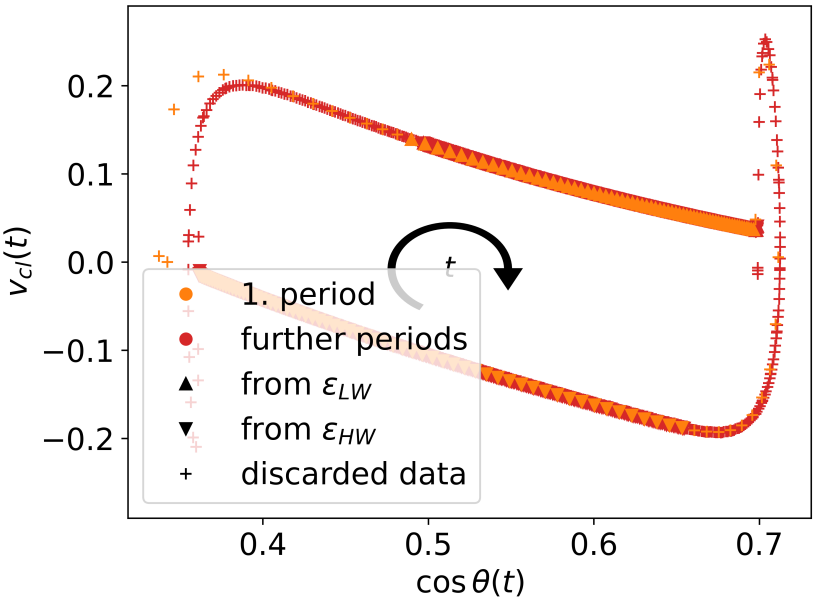

Figure 5.9: Velocity of the contact line v_{cl} plotted against $\cos\theta(t)$ for (a) a droplet on a surface with a periodically switched wettability from $\epsilon_{HW} = 0.762$ to $\epsilon_{LW} = 0.632$ with the initial droplet equilibrated on a surface with a wettability of ϵ_{LW} in the MD model. The switching period was $T = 2 \cdot 10^6$ MD steps. The data points are spaced equidistantly with $\Delta t = 10^4$ MD steps. The dashed lines are plots of Eq. (5.8) with values of ζ_R for wettabilities of ϵ_{HW} and ϵ_{LW}, respectively. (b) The TF equivalent of (a) with $T = 15.8$ and $\Delta t = 0.1$. Note that there is no noise in the TF model.

Table 5.3: Relaxation times τ_{rel} obtained from a fit of a stretched exponential to the values of $\cos(\theta)$ versus t for switching from ϵ_1 to ϵ_2 for MD and TF simulations. Additionally, relaxation times τ_{MKT} obtained from a fit of a stretched exponential to the values of $\cos(\theta)$ versus t for switching from ϵ_1 to ϵ_2 for MKT calculation with ζ_{MD}/γ and ζ_{TF}/γ as input parameters, respectively, are shown.

ϵ_1	ϵ_2	τ_{rel} (MD)	τ_{MKT} (MD)	τ_{rel} (TF)	τ_{MKT} (TF)
0.632	0.671	$6.84 \cdot 10^4$	$7.55 \cdot 10^4$	2.37	2.19
0.671	0.632	$6.84 \cdot 10^4$	$6.92 \cdot 10^4$	2.23	2.02
0.632	0.762	$12.02 \cdot 10^4$	$11.82 \cdot 10^4$	5.34	5.87
0.762	0.632	$11.33 \cdot 10^4$	$10.52 \cdot 10^4$	4.74	3.54

strate within the MD model. Linear fits of the data points after each change in wettability show comparable slopes to the single switch scenario in Fig. 5.8 (a). This holds for later switching cycles as well. Also, the dashed lines, which show Eq. (5.8) with values of ζ_R for the corresponding wettabilities, confirm again that the values of ζ_R and ζ_{MD} agree well. The same phenomena are seen for the TF data in Fig. 5.9 (b).

5.4 RELAXATION BEHAVIOR AFTER A SINGLE SWITCHING EVENT

Knowledge about the velocity of the contact line should contain the relevant information to predict the relaxation behavior of $\cos(\theta(t))$. This is first explicitly explored for a single switching event for different pairs of wettabilities. For this purpose $\cos(\theta(t))$ is determined after a single switching event and the resulting relaxation curve is fitted by a stretched exponential. The resulting relaxation times τ_{rel}, using Eq. (5.7), are listed in Table 5.3 both for the TF and the MD data. For comparison, the same procedure is applied to data obtained from the MKT according to Eq. (5.12). As input parameters the values of ζ_{MD}/γ and ζ_{TF}/γ shown in Fig. 5.7 are used. These relaxation times are denoted τ_{MKT} and they are also listed in Table 5.3. Indeed, one can find a reasonable agreement between both approaches while the times slightly depend on the switching direction.

For the wettability pair $\epsilon_{LW} = 0.632$ and $\epsilon_{HW} = 0.762$, the evolution of the MKT, TF and MD model are compared for both switching directions in Fig. 5.10. To compare these approaches the time scale is given in relation to the relaxation time τ_{rel} when switching from ϵ_{LW} to ϵ_{HW}. This special relaxation time is denoted τ_s. In this dimensionless representation, the MD and the TF data agree very well. For all subsequent analyses, the times will be expressed in terms of t/τ_s. Note that in Fig. 5.10 not only the time scales but also the degree of non-exponentially is comparable between the MD and TF approach. Indeed,

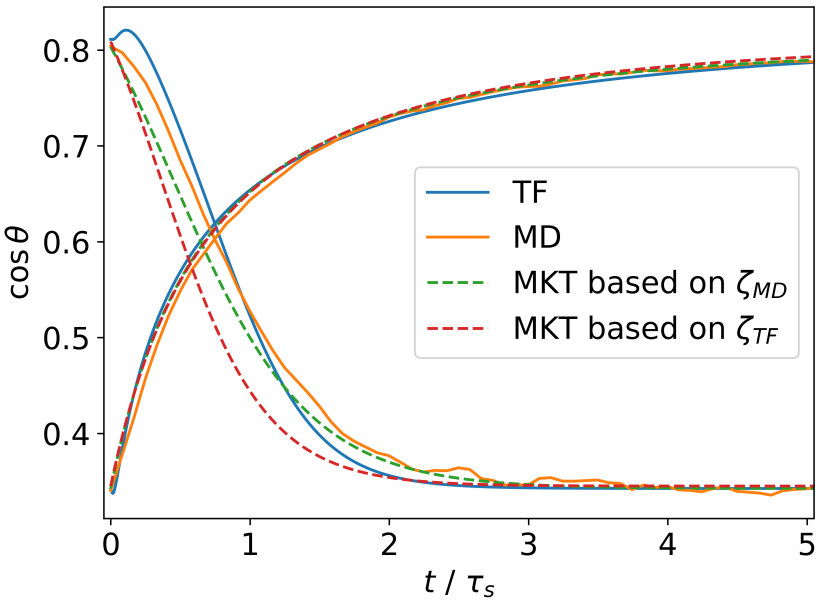

Figure 5.10: $\cos(\theta)$ obtained from MKT, TF and MD simulations plotted against t for a single switch. The corresponding values of ϵ_w are 0.632 and 0.762.

as discussed in Section 5.2.3 and qualitatively seen in Fig. 5.10, when switching to the state of lower wettability one observes a stretched exponential whereas in the opposite case a compressed exponential is seen. This can be fully rationalized by the properties of the analytical solution in Eq. (5.23) (see Section 5.2.3).

Furthermore, the MKT predictions obtained from the integration of Eq. (5.12) are included in Fig. 5.10. The MKT resembles the MD and TF values for switching remarkably well except for an offset. This offset of the MKT mirrors that initially v_{cl} does not depend linearly on $\cos(\theta)$ for reasons discussed below. However, if the MKT values were shifted by $\sim 0.2\ \tau_s$ which is approximately the time of the nonlinear behavior at the beginning of each switching event, the agreement with MKT would be quite good. This shows that MKT can reproduce MD and TF results but with much less computational effort, once this is accounted for. This behavior can be attributed to a dead-time effect. Directly after the switching, the droplet starts adapting to changes in the substrate's wettability in the contact region and this influences the contact angle obtained from the overall droplet properties. Naturally, this leads to differences between the MKT and the MD model as seen in Figs. 5.8 to 5.10, because the MKT assumes a circular shape and does not allow for the exact droplet shapes observed in the MD model. One might believe that the measurement of the contact angle is the reason for the deviations and a better measurement might make them disappear.

However, Fig. 5.9 confirms that the contact angle measurement is not responsible for the differences because the MKT prediction for $t = 0$ disagrees with the expected equilibrium values. For example in Fig. 5.8 (a) the MKT would predict $\cos(\theta(t = 0)) \sim 0.85$ instead of the expected initial equilibrium value ~ 0.80 as otherwise the final equilibrium state would be off. Thus, in total, the droplet reacts significantly slower than predicted by MKT. This effect is much weaker when switching from low to high wettability, as seen in Fig. 5.8 (a).

So far, the contact line has been determined from a circle fit to the droplet. In this sense, it can be regarded as an effective contact line. However, in particle-based simulations, it is possible also to determine the microscopic contact line. In particular, if the droplet shape is highly non-circular some deviations between the microscopic and effective contact line may be expected. To illustrate the differences, in Fig. 5.11 the velocities of the effective and the microscopic contact line are compared as a function of simulation time. Indeed, this initial non-monotonous velocity behavior of the effective contact line is not reproduced by the microscopic contact line and a monotonous behavior is observed. To compensate for this initial difference, for intermediate times $t \sim \tau_s$ the microscopic contact line is slower than the effective contact line. Closer to the new equilibrium position, where the shape is nearly circular, the velocities agree. As also seen in Fig. 5.11 the nature of the deviations for short times can be explicitly seen when plotting the droplet shape and the resulting circle fit for different initial times. As already expected from Fig. 5.7 the deviations between both contact lines are higher for the transition from high to low wettability.

The strong differences between the microscopic and the effective contact angle and their respective different time dependence for the switching from high to low wettability have a very natural explanation: after the switching process, the microscopic contact line moves towards the center of the droplet whereas the remaining part of the droplet hardly changes. This explains why the microscopically defined velocity is quite large whereas the effective contact line hardly moves. However, for the further advancement of the microscopic contact line towards the center of the droplet the whole droplet has to rearrange. In this regime the effective contact line moves faster, reflecting the rearrangement of the whole droplet. Closer to the final equilibrium configuration both definitions of the contact line yield very similar results. To conclude, the deviations from the MKT behavior are only partly caused by the application of a circular fit to the droplet profiles but to a large extent reflect the presence of a kind of *dead time* in the MD simulations during which the droplet hardly changes its shape except for localized transport close to the contact line.

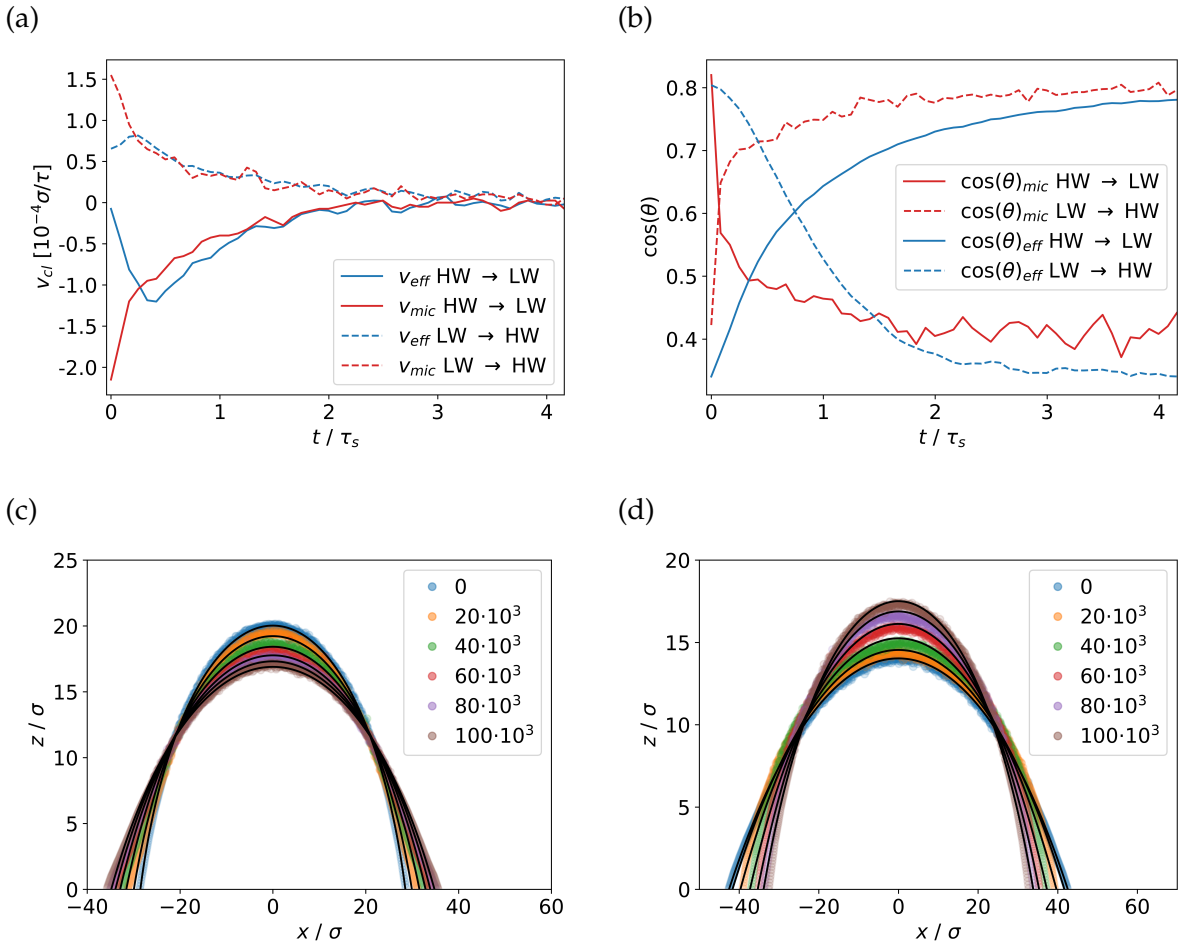

Figure 5.11: (a) Microscopic contact line velocity v_{mic} compared to the effective contact line velocity v_{eff} extracted from circular fits for different switching directions. (b) Cosine of the contact angle obtained by a fit through the positions of the liquid-vapor interface at $z = 0\ \sigma$ and $z = 2\ \sigma$ $\cos(\theta)_{mic}$ versus t compared to the contact angle obtained from a circular fit $\cos(\theta)_{eff}$ (c) Droplet profiles compared to circular fits for switching from $\epsilon_{LW} = 0.632$ to $\epsilon_{HW} = 0.762$ and (d) droplet profiles compared to circular fits for switching from $\epsilon_{HW} = 0.762$ to $\epsilon_{LW} = 0.632$.

5.5 PERIODIC SWITCHING

A periodic switching procedure yields an oscillating state around a plateau value of $\cos(\theta)_{plateau}$ after an initial relaxation. This is shown for MD simulations in Fig. 5.12 (a) and TF simulations in Fig. 5.12 (b) where the wettability of the surface is switched with a period T which is approximately 50% larger than the respective τ_s values. In Fig. 5.12 (a) the MD simulation data is accompanied by MKT results. The agreement is good except for a slight offset towards the high wettability state. The triangles in Fig. 5.12 (a) and (b) mark the average value of $\cos(\theta)$ during the individual switching period denoted as $\cos(\theta)_{MA}$. Similar simulations to the ones shown in Fig. 5.12 (a) and (b) have been repeated for different switching periods as shown in Fig. 5.12 (c) and (d). There, only $\cos(\theta)_{MA}$ is shown. In Fig. 5.12 (e) and (f) the results for a smaller difference in wettability representing a smaller change in contact angle are shown. The analytical prediction based on the MKT for small contact angle differences in the case of very fast switching added in Fig. 5.12 (e) agrees well with the actual MD data.

Now, the different properties of $\cos(\theta)_{MA}$ as seen in Fig. 5.12 (c)-(f) are analyzed individually. The properties of interest are the plateau value, the relaxation time and the amplitude as a function of the switching time T.
Plateau values: The plateau values of $\cos(\theta)_{MA}$ in dependence of the period T are shown in Fig. 5.13 for the two wettability differences used before. The lack of noise in the TF model leads to a convergence of $\cos(\theta)_{MA}$ so that the plateau value can be determined trivially. In the MD model, an average over some cycles is necessary to reduce noise. Such a procedure is mandatory because the observed relations as shown in Fig. 5.13 are relatively small compared to the evolution of $\cos(\theta)_{MA}$[1]. Numerical MKT results based on Eq. (5.12) as well as analytical results according to Eq. (5.27) are shown along the MD and TF results in Fig. 5.13. Since the relaxation times (see Table 5.3) are nearly identical for both switching directions, the overall dependence of $\cos(\theta)_{plateau}$ on the period T is low as predicted by Eq. (5.28). In the limit of large T, the plateau value just corresponds to the average of the two equilibrium values of $\cos(\theta)$.

The subsequent discussions are restricted to Fig. 5.13 (a) because there the statistical uncertainties of the MD are sufficiently small. Qualitatively all modeling approaches predict an increased plateau value for an increasing switching period. According to the analytical expression

1 Note the scaling of the y-axis in Fig. 5.12, $\cos(\theta)$ for droplets equilibrated at the corresponding high and low wettabilities is (a) ~ 0.34 and ~ 0.80 and (b) ~ 0.34 and ~ 0.49.

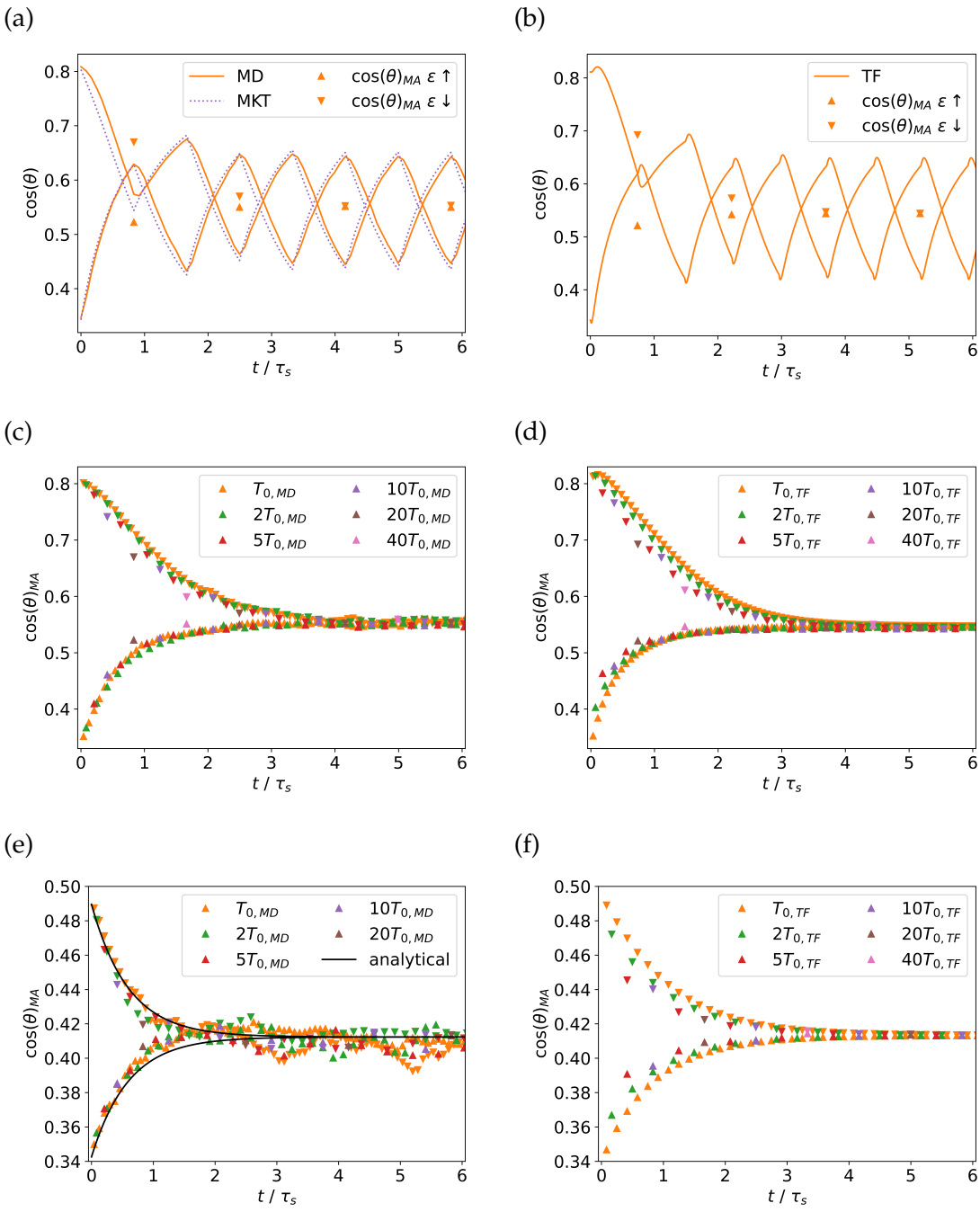

Figure 5.12: (a) The solid line shows the cosine of the contact angle $\cos(\theta)$ plotted against t for a switching period of $T = 1.524\tau_s$. The triangles mark the average cosine of the contact angle over one period $\cos(\theta)_{MA}$ and the dashed line shows the results obtained from the MKT. (b) Corresponding results in the TF model for a switching period of $T = 1.478\tau_s$. (c) and (e) $\cos(\theta)_{MA}$ for different periods from 1 to 40 $T_{0,MD}$, where $T_{0,MD} = 7.62 \cdot 10^{-2}\tau_s$ while periodically switching the surface between ϵ_{LW} and ϵ_{HW}. (d) and (f) TF simulations with corresponding wettability parameters, where $T_{0,TF} = 7.39 \cdot 10^{-2}\tau_s$. In (c) and (d) the chosen wettabilities are $\epsilon_{LW} = 0.632$, $\epsilon_{HW} = 0.762$ whereas in (e) and (f) the corresponding values read $\epsilon_{LW} = 0.632$, $\epsilon_{HW} = 0.671$. In (e) the MKT prediction for the limit of fast switching has been added.

(a)

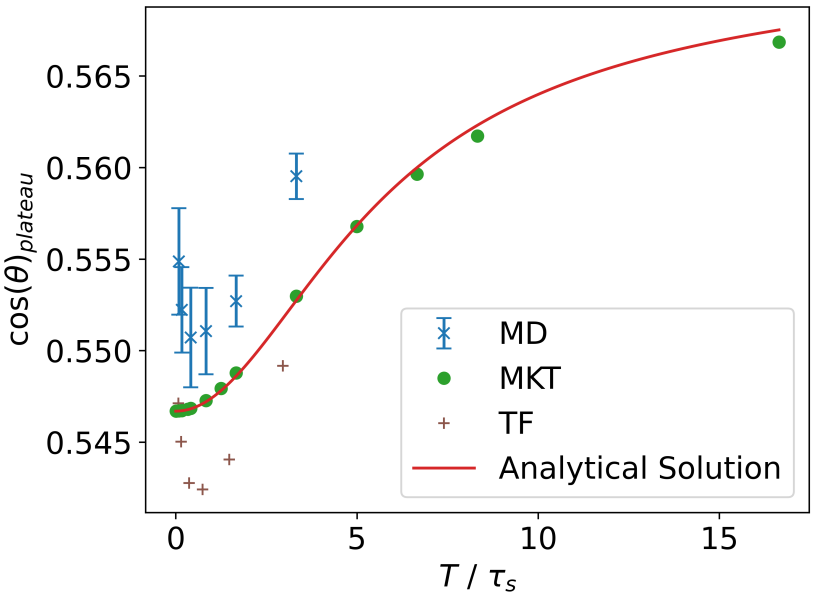

(b)

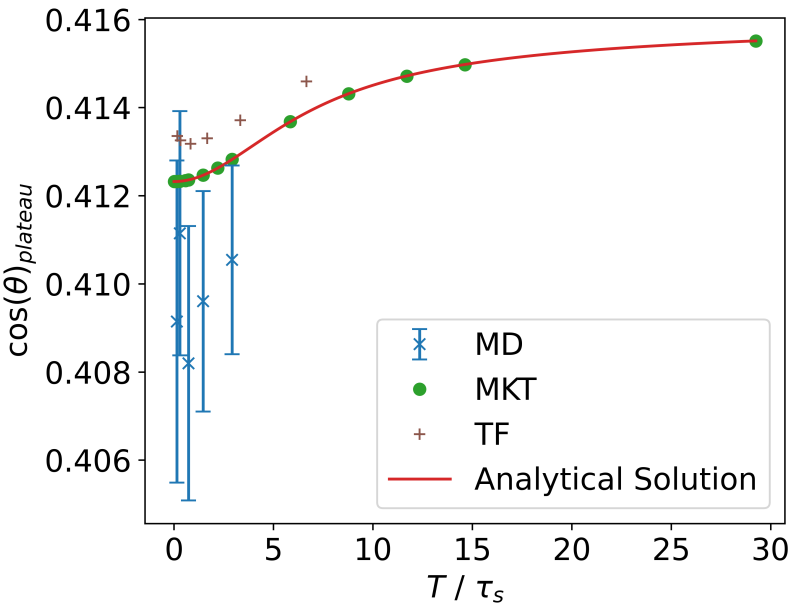

Figure 5.13: (a) $\cos(\theta)_{plateau}$ obtained from MD, MKT, TF and from the analytical expression in Eq. (5.27) plotted against T for switching between (a) $\epsilon_{LW} = 0.632$ and $\epsilon_{HW} = 0.762$ and (b) $\epsilon_{LW} = 0.632$ and $\epsilon_{HW} = 0.671$.

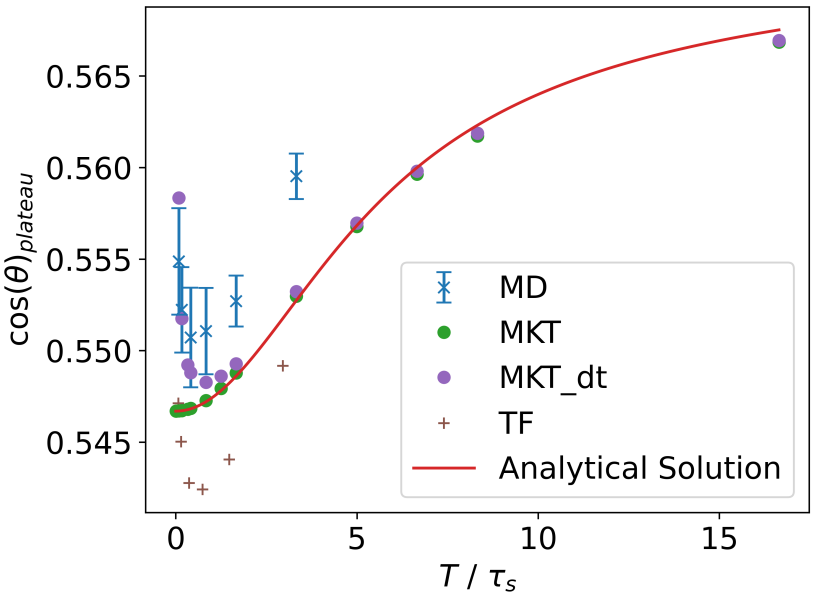

Figure 5.14: Reproduction of Fig. 5.13 with the addition of a numerical MKT result with an artificial dead-time effect. The dead-time effect was realized by setting $\gamma/\zeta = 0$ for the first 1500 time steps when switching towards the higher wettability. For the inverse switching direction, $\gamma/\zeta = 0$ was set for the first 1125 time steps after each switching event. The number of time steps was gauged based on the data points deviating from the linear fits in Fig. 5.8. A systematic procedure to determine the dead time quantitatively could not be found.

Eq. (5.28) the relation is quadratic initially and flattens when approaching the limit $T \to \infty$. For switching periods $T/\tau_s \leq 0.6$, a discrepancy between TF and MD model on one hand and the numerical MKT approach as well as the analytical expression Eq. (5.27) is notable. The TF and the MD models do not predict a monotonous increase in the plateau value. Instead, they predict a local minimum of the plateau value. Quantitatively the agreements in Fig. 5.13 are off by $\mathcal{O}(10^{-3})$, which is very low considering the fundamental differences between the models. Note that $k_{3,i}$ was substituted by $\tilde{k}_{3,i}$ to compensate for the large wettability difference. Otherwise, the prediction of Eq. (5.28) had deviated from the numerical MKT solution.

To check the hypothesis that the difference in the MKT-based solutions is due to the dead-time effect additional numerical MKT solutions were performed where $\gamma/\zeta = 0$ was set for the first few time steps after each switching event. The result is shown in Fig. 5.14. Indeed, a minimum can be seen. This effect can be also understood from the analytical expression. In the limit of fast switching $y_{plateau} = \frac{k_{3,\uparrow}}{k_{3,\downarrow}+k_{3,\uparrow}}$ holds. Due to the dead-time effect, which is particularly pronounced for the

transition from high to low wettability, the value $k_{3,\downarrow}$ would need to be substituted by an effective relaxation rate which is smaller because of the initial presence of the dead-time effect. This effect becomes more prominent for very short switching times. As a consequence, $y_{plateau}$ increases when T becomes very small.

Relaxation times: To obtain relaxation times for the MD and TF simulations as well as for the numerical solution of the MKT approach (Eq. (5.12)) stretched exponentials were fitted to the data and the respective time scales were then calculated with Eq. (5.7). Importantly, during a very broad range of different switching periods, there is hardly any variation of the relaxation times, neither for MKT nor for the MD and TF data, respectively, as can be seen in Fig. 5.15. Furthermore, one observes that the relaxation times for the initial transitions to higher and lower wettabilities, respectively, become closer to each other if the two wettabilities are closer to each other. Indeed, this is fully compatible with the analytical solution in Eq. (5.26) for the limit of small wettability changes. There, the relaxation time does not depend on the time scale of the switching period and is identical for both initial switching directions. Note that the results from MD simulations for smaller changes in wettability exhibit relatively high noise, which renders the fitting procedure unreliable as can be seen especially from the outlier in Fig. 5.15 (c).

Amplitudes: The analytical solution given in Eq. (5.29) overlaps very well with the results from the MD and MKT simulations as shown in Fig. 5.16. Both results show that the amplitude decreases with T. The minor deviations between analytical and MD as well as TF solutions can be attributed to two things. First, the TF and MD data exhibit a small dip before it increases when the effective wettability is higher than the initial wettability. This cannot be grasped by a stretched exponential function and is much more pronounced in the TF model. Second, the underlying approximation of small differences in the contact angle of the analytical solution becomes notable. However, deviations between MKT and the analytical solution vanish for decreasing contact angle difference.

5.6 CONCLUSION

In this chapter, the wetting dynamics of a droplet on a periodically switched surface were characterized by particle-based MD and mesoscopic TF simulations. Through the mapping of the respective energy scales, the equilibrium behavior can be mapped. Via additional rescaling of the respective spatial and temporal scales, also the non-equilibrium behavior of both approaches can be compared in di-

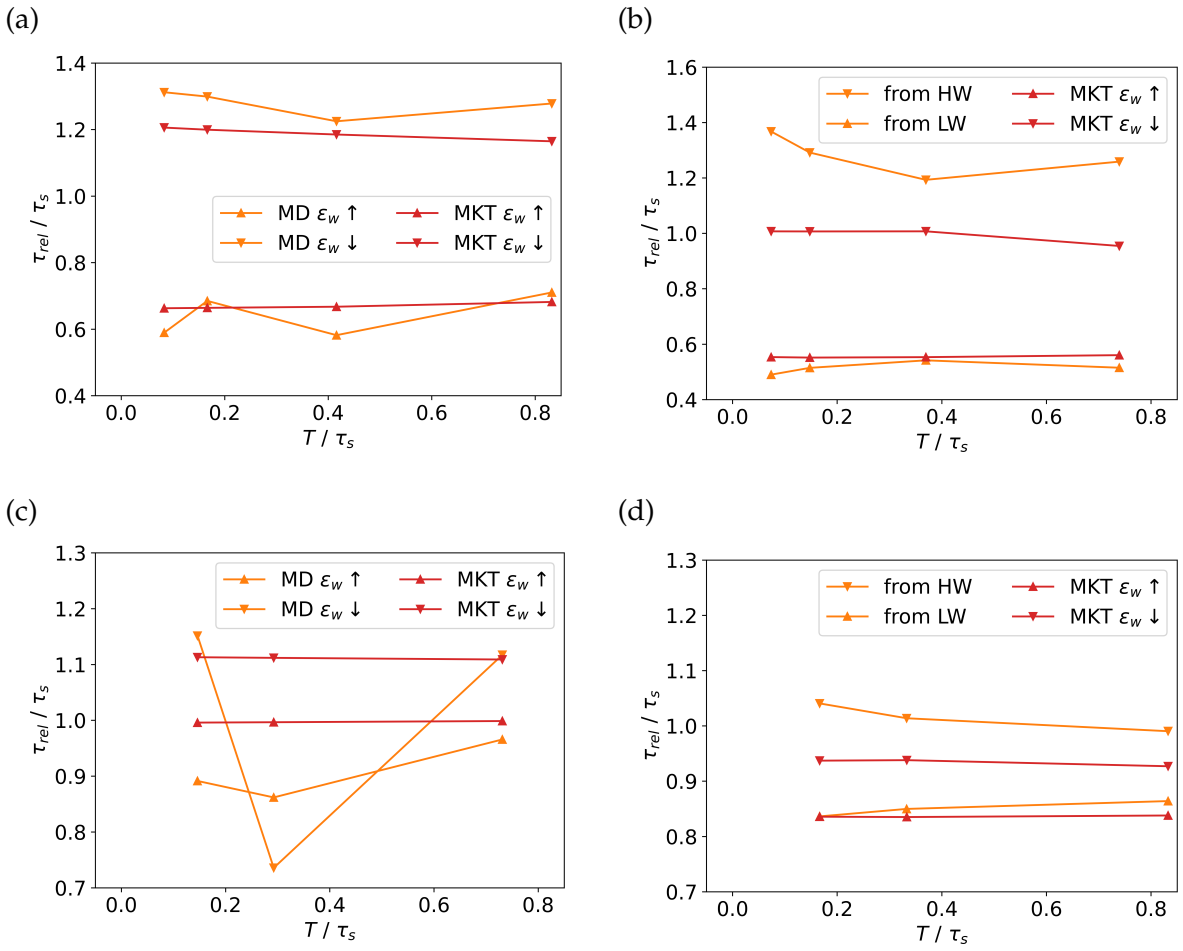

Figure 5.15: (a) and (b) Relaxation times τ_{rel} resulting from stretched exponential fits to $\cos(\theta)_{MA}$ versus t from MD and TF data respectively for switching between $\epsilon_w = 0.632$ and $\epsilon_w = 0.762$. (c) and (d) τ_{rel} resulting from stretched exponential fits to MD and TF data respectively for switching between $\epsilon_w = 0.632$ and $\epsilon_w = 0.671$. Note that the fitting procedure is complicated by noise in the results from MD simulations for smaller changes in wettability which leads to the outlier in (c).

(a)

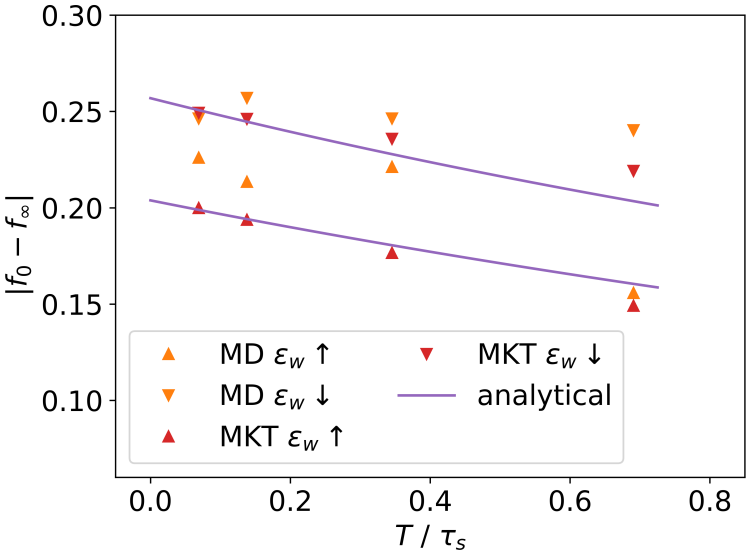

(b)

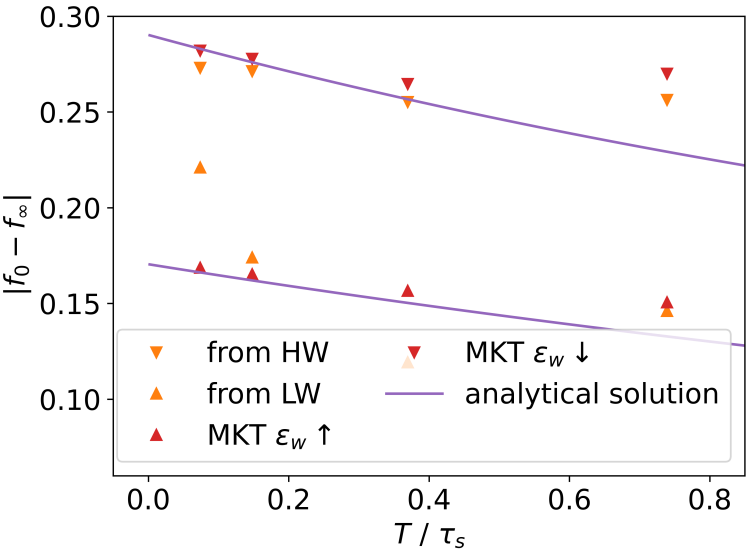

Figure 5.16: (a) and (b) amplitudes resulting from stretched exponential fits to MD and TF data for $\cos(\theta)_{MA}$ respectively for switching between $\epsilon_w = 0.632$ and $\epsilon_w = 0.762$. The analytical result stems from Eq. (5.29).

mensionless units. Indeed, both approaches display a very similar relaxation behavior when analyzing the response to a single switch or a periodically switched substrate. Important additional insight could be gained by interpreting the results within the molecular kinetic theory of wetting (MKT). This was realized on different levels.

(1) The assumption of the MKT, namely the presence of a driving force for the contact line dynamics which is proportional to the difference of the cosine of the contact angle to its equilibrium value, was explicitly checked. This was fulfilled for a large range of contact angles and allowed for the definition of a friction term translating the driving force into the dynamics of the contact line. Only for times directly after a switching event, the contact angle hardly changed due to additional reorganization of the droplet shape. To a good approximation, this can be described as a kind of dead time.

(2) The time evolution of the contact angle was formulated based on the MKT approach, taking into account the preservation of the droplet volume. The input for the single model parameter of that approach (apart from the equilibrium properties) was taken from (1). For this comparison, it turned out to be very helpful to average the relaxation behavior over single switching periods and to analyze the time evolution of these averaged values. After careful comparison of different features of this time evolution (long-time stationary behavior, i.e. plateau value, relaxation time and amplitude of relaxation) the results from MKT turned out to be very close to those obtained from MD and TF simulations. Beyond the conceptual insight gained from this comparison, the MKT approach may substitute MD or TF simulations for some applications as it is orders of magnitude more efficient with respect to simulation time and might naturally be easily generalized to more complex switching patterns. Finally, this detailed comparison also allowed to identify the impact of the initial dead time of the droplet relaxation. Beyond the slight modification of the plateau value of the contact angle, the initial behavior gives rise to a non-monotonous dependence of the plateau value of the contact angle when approaching very short switching periods.

(3) Analytical solutions of the MKT equations for the general case of periodic switching could be obtained. The approximations were particularly uncritical when the change in contact angle between both states was not too large. Indeed, some of the numerically seen features such as the independence of the relaxation time on the switching period on the specific deviations from exponential relaxation could be reproduced analytically.

(4) Using the scheme from Ruijter, Blake and De Coninck[97] additionally, the required MKT parameters could be extracted directly from the analysis of separate MD simulations. This underlines that the microscopic mechanisms, proposed in the MKT close to the contact line, capture the essential processes of the wetting dynamics of the droplet in the MD simulations.

6

SUMMARY AND OUTLOOK

In this thesis, the dynamics of simple liquids on temporally switchable and spatially pre-structured substrates substrates have been studied theoretically. For that purpose, the mesoscopic TF model was applied in combination with the microscopic MD model. In some cases, accompanying analytical results based on the MKT could be derived. The TF model results were obtained numerically using the finite element method (see Section 3.1). For the microscopic modeling, the Lennard-Jones potential with a cutoff radius and the dissipative particle dynamics thermostat were employed. In addition, a method for the continuation of periodic orbits that exist only due to external forcing has been presented in Section 3.3. This allows systematic combing of the parameter space for all PDEs that exhibit such periodic orbits, i. e. this method is not restricted to the TF model used for the proof of concept.

Multiscale approaches in general have already demonstrated in many fields that they are able to strongly contribute to the understanding of phenomena from different perspectives and drastically reduce computation times. In the field of fluid dynamics, many multiscale approaches have been successfully applied. In this thesis, various multiscale approaches have been developed and applied in the field of switchable and pre-structured substrates. The presented test cases for these approaches are small (only a few droplets) and the topologies are simple. A reasonable next step is to apply the approach presented here to substrates with arbitrary pre-structuring, which can then also be switchable. Such manipulation of fluid structures can be useful in the context of lab-on-a-chip systems.

In chapter Chapter 4, an approach was presented to allow quantitative comparisons between an MD and a TF model. Until now, comparisons have mostly been on a qualitative basis. However, for hybrid modeling, quantitative comparability is inherently necessary. Several hybrid approaches are conceivable: On the one hand, one could model certain subregions (e.g. the contact region of a droplet) at the microscopic level, while the rest is simulated with a more coarse-grained model that is computationally cheaper (see [12] for an example of such an approach). Second, in situations with a combined fast and slow dynamics, the combination of models may decrease computation times significantly as the slow dynamics can be described sufficiently accurately with a more abstract model. For instance, for semiconductor

laser systems, such an approach could reduce the computational effort by up to two orders of magnitude [13]. The successful quantitative comparisons between MD and TF model in the case of droplet spreading and coalescence are a necessary requirement to establish a hybrid approach based on these models.

In chapter Chapter 5, the mapping method for the wettability parameters from the previous chapter was used again. In this chapter, periodic switching on a homogeneous substrate was investigated. The analysis confirmed that the TF model and the MD model are suitable for a multiscale description of simple liquids on switchable substrates. Even further, the rather involved modeling could largely be substituted by the rather basic MKT approach based on a driving force proportional to the difference of the contact angle to its equilibrium value. For small wettability differences, i. e. small equilibrium contact angle differences between the states switched between, analytical expressions could additionally support the reduced description based on the aforementioned driving force. Essential differences between the MKT and the MD and TF modeling approach could be reduced by introducing a so-called dead time. However, no systematic way was found to quantify the dead time.

The agreement between TF and MD model was consistently good. Nevertheless, differences could be found. By design, the MD model contains noise. This can be included in the TF model by adding a noise term (for example see [65]). However, the disjoining pressure and the mobility are the more relevant quantities for the agreement of the models. For the disjoining pressure, there are already methods available to extract it [58–61, 109–112]. These techniques promise to improve the TF model. It is not clear though how these extracted disjoining pressures influence the dynamics. Similar techniques to extract the mobility have not been developed yet. However, the results from this thesis can be regarded as a first step towards that goal, e. g., the mapping approach in Chapter 4 might be helpful to test the extracted mobilities.

The mapping methodology between the models is not explicitly tailored to the MD model and the TF model. For example, one could combine MD simulations with the boundary element method to describe larger contact angles. However, contact angles beyond 90° require adjustments, since the height profile can no longer be expressed as a single-valued function. However, it should be possible to define a function that, based on the density, provides a measure with the necessary properties as described in Section 4.2.

Especially for the fast switching in Chapter 5 scenarios were simulated which are not physically realizable according to the current state of

research. In particular, multiple switching of the wettability is not yet possible in the time scale of the droplet relaxation. Experimental comparisons in already realizable scales would strengthen the predictive power for the not-yet-realizable range.

The comparisons between the microscopic MD model and the mesoscopic TF model clearly showed the limits of the TF model. Most notable is the smoothened contact region owing to the lubrication approximation and the restriction to smaller contact angles. However, it has also been confirmed (even though it has not been studied systematically) that the lubrication approximation can be applied in a wider range than one might expect. Similarly, for gravity-driven flow over steep topologies, it could be observed by comparison to the full Navier-Stokes equation that the lubrication approximation holds better than expected [124]. All in all, this thesis can be regarded as another example that supports the consensus that the lubrication approximation is applicable in a wide range of regimes making it a good candidate for the multiscale modeling of liquid droplets.

APPENDIX

A

IMPROVING REPRODUCIBILITY

According to a Nature survey, more than 70% of researchers have tried and failed to reproduce another scientist's experiments and more than half have failed to reproduce their own experiments [125]. Reproducibility is not only an issue concerning experiments. Instead of humidity and temperature the relevant variables for reproducible research based on numerical methods are program version and environment variables. Here, I describe specific techniques used during this thesis to improve the reproducibility of the presented results. Disclaimer: This is by far not a best-practice approach. The purpose is to give ideas to improve reproducibility step by step.

Often simulation software evolves alongside a research project and it might happen that you cannot reproduce initial results with the "final" version of the software. For reproducible software development, there is no way around version control software like GIT. Version control software helps to pinpoint the exact program version for simulations intended for publication. Conveniently, the last commit and whether there are uncommitted files can be automatically logged to the output folder of a simulation with the commands `git status` and `git log -1`.

All the thin-film model simulations have been performed using the library OOMPH-LIB, which is written in C++ and expects driver code in C++. For researchers not familiar with programming in general C++ is quite a hurdle to take and the essential changes between simulations were often buried rather deep in the source code. To solve these issues I used BOOST.PYTHON to compile the C++ source code as a Python library, which can then be easily accessed from Python. An example of a Python script that first equilibrates a droplet with wettability ρ_1, switches the substrate to ρ_2 to simulate the adaption to the new wettability is shown in listing A.1.

Listing A.1: Simple wrapper python script using a library compiled from OOMPH-LIB source code. It imports the code shown in listing A.4.

```
#!/usr/bin/python3
import libprestructured_1Dtfe as TFElib
from scan_basics import *
RHO1 = -0.5
RHO2 = 1.5
T = 100
problem = init_problem(rho = RHO1, switching_period = sp)
problem.integrate_until_steady()
problem.set_elements_to_equilibrated()
problem.rho = RHO2
problem.integrate_for_time(T)
finalfolder = "demonstration"
tidy_up(problem, finalfolder)
```

In `scan_basics.py` some helper functions, which do not change frequently are bundled, e. g. `init_problem()`, a wrapper for the problem constructor which also saves all variables accessible to Python to an easily accessible JSON file format. `tidy_up()` gives the output folder its final name, logs the GIT output as mentioned before, copies the simulation script to the output folder and sets the data to read-only to prevent accidental changes to the data. A condensed version of the script `scan_basics.py` is shown in listing A.4. A full version can be found in the Zenodo Tutorial [79].
The listing A.2 demonstrates a simple parameter scan in ρ. The code was used for the parameter scan to determine the relation between the wettability ρ and the rFWHM as shown in Fig. 4.4 b).

Listing A.2: Wrapper python script used for a parameter scan in the wettability ρ. It imports the code shown in listing A.4.

```
#!/usr/bin/python3
import libprestructured_1Dtfe as TFElib
from scan_basics import *
dLAMBDA = 0.05
LAMBDA_MAX = 1.
LAMBDA = -0.9 #aka rhoLW
while (LAMBDA < LAMBDA_MAX):
    problem = init_problem(RHO = LAMBDA)
    problem.integrate_until_steady()
    tidy_up(problem, "rho_scan_{:+.2f}".format(LAMBDA))
    LAMBDA += dLAMBDA
```

Additionally BOOST.PYTHON gives direct and easy access to high-level Python modules, which would have required linking the C++ code against another library. Listing A.3 is an example using the interpolation functionality provided by the NUMPY library to interpolate a function with an arbitrary discretization to the mesh's discretization.

Listing A.3: Code snippet to set initial condition from a Python script using the interpolation function `interp()` provided by NumPy. The seamless integration and interaction with C++ variables and objects in Python are also demonstrated.

```
# Use linear interpolation to set the height profile to the
    values of new_h at the positions x
def set_initial_condition_from_values(problem, x, new_h):
    mesh = problem.mesh_pt()
    for n in range(0, mesh.nnode()):
        node = mesh.node_pt(n)
        xpos = node.x(0)
        new_h_val = np.interp(xpos, x, new_h)
        node.set_value(0, new_h_val)
```

Without Boost.Python you had to link against a C++ library providing this functionality or write the code yourself. Both alternatives take much more time which is not worth it because setting the initial condition is not performance critical as it is used only once per simulation run in most cases.

Listing A.4: Condensed version of the script SCAN_BASICS.PY used for all the OOMPH-LIB simulations.

```
#!/usr/bin/python3
import numpy as np
import shutil
import os
import libprestructured_1Dtfe as TFElib
import json
import inspect

def init_problem(RHO):
    os.mkdir("out")
    inhomogenity = "homogeneous"
    problem = TFElib.My1DProblem(4096, 15.)
    problem.rho = RHO
    problem.set_initial_drop()
    problem.assign_initial_values_impulsive()
    problem.doc_solution()
    all_params_to_json(problem)
    return problem

def create_dict_from_problem(problem):
    members = inspect.getmembers(problem)
    new_dir = {}
    for element in members:
        if (isinstance(element[1],str) or isinstance(element
            [1],int) or \
            isinstance(element[1],float)) and (not '__' in
                element[0]):
            new_dir[element[0]] = element[1]
    return new_dir

def all_params_to_json(problem):
    output_dict = create_dict_from_problem(problem)
    TXT_to_file = json.dumps(output_dict)
    with open('out/params.json', 'w') as f:
        f.write(TXT_to_file)

def tidy_up(problem, finalfolder):
    output_directory = problem.doc_info.directory
    shutil.copy("run_parameter_scan.py", output_directory +
        "/run_parameter_scan.py")
    shutil.copy("scan_basics.py", output_directory + "/
        scan_basics.py")
    os.system("chmod a-w -R " + output_directory)
    shutil.move(output_directory, finalfolder)
```

B

ANALYTICAL CALCULATION OF WETTING PROPERTIES FOR PERIODIC SWITCHING

For a single switch, the derivation of the analytical solutions is presented in Section 5.2.1. Based on those results analytical expressions for periodic switching are derived in the following using the normalized quantities $y(t) = (x(t) - x_{eq})/(x_0 - x_{eq})$, where x_0 and x_{eq} correspond to the initial $\cos(\theta_0)$ and the final equilibrium $\cos(\theta_{eq})$ respectively. The central equation in the derivation is

$$\frac{d}{dt}y(t) = -k_{3,i}(y - a_i) \tag{B.1}$$

with a contact angle independent $k_{3,i}$ where i denotes the prefactor k_3 for an increasing ($\uparrow$) or decreasing ($\downarrow$) wettability. Its general solution for a given initial condition $y(t = 0)$ reads

$$y(t) = a_i(1 - \exp(-k_{3,i}t)) + y(t = 0)\exp(-k_{3,i}t) \tag{B.2}$$

as derived before (see Eq. (5.21)). Here, the assumption is that before the first switching event, the system is at equilibrium in the state of higher wettability. Then, in the first part of the switching period ($t \in [0, T/2)$) the substrate has the lower wettability $a_\downarrow = 0$ and in the second half the substrate has the higher wettability $a_\uparrow = 1$ ($t \in [T/2, T)$). The switching period is denoted as T. Thus, for the first half of the first switching period, one obtains

$$y(t) = y(0)\exp(-k_{3,\downarrow}t). \tag{B.3}$$

In the second half of the first switching period

$$y(t) = (1 - \exp(-k_{3,\uparrow}t)) + y(0)\exp(-k_{3,\downarrow}T/2)\exp(-k_{3,\uparrow}T/2) \tag{B.4}$$

holds, which makes use of the relation Eq. (B.3). The average over the first half period is thus given by

$$\langle y_1 \rangle = y(0)\frac{1}{k_{3,\downarrow}T/2}\left(1 - \exp\left(-k_{3,\downarrow}T/2\right)\right) \tag{B.5}$$

and that over the second half period as

$$\begin{aligned}\langle y_2 \rangle =& 1 - \frac{1 - \exp(-k_{3,\uparrow}T/2)}{k_{3,\uparrow}T/2} + y(0)\exp(-k_{3,\downarrow}T/2)\frac{1}{k_{3,\uparrow}T/2}(1 - \exp\left(-k_{3,\uparrow}T/2\right)) \\ =& 1 - \frac{(1 - \exp\left(-k_{3,\uparrow}T/2\right))}{k_{3,\uparrow}T/2}(1 - y(0)\exp(-k_{3,\downarrow}T/2)).\end{aligned} \tag{B.6}$$

The average over both time intervals finally reads

$$\begin{aligned}\langle y(0)\rangle =&\frac{1}{2} - \frac{1-\exp\left(-k_{3,\uparrow}T/2\right)}{2k_{3,\uparrow}T/2} + y(0)\left[\frac{1}{2k_{3,\downarrow}T/2}(1-\exp\left(-k_{3,\downarrow}T/2\right))\right.\\ &\left.+\exp\left(-k_{3,\downarrow}T/2\right)\frac{1}{2k_{3,\uparrow}T/2}(1-\exp\left(-k_{3,\uparrow}T/2\right))\right].\end{aligned} \tag{B.7}$$

Naturally, the previous procedure can be extended to describe the evolution during the n-th period. To get a general expression $\langle y(n)\rangle$ an explicit expression for the corresponding evolution $y(t)$ for $t \in [nT,(n+1)T)$ is needed. The expression in Eq. (B.4) can generalized to calculate the value $y(t = n\cdot T)$ from its value at $t = (n-1)\cdot T$. This gives

$$y(t = n\cdot T)) = C + Dy(t = (n-1)\cdot T) \tag{B.8}$$

with $C = (1-\exp\left(-k_{3,\uparrow}T/2\right))$ and $D = \exp\left(-k_{3,\downarrow}T/2\right)\exp\left(-k_{3,\uparrow}T/2\right)$. This recursive relation has a straightforward solution which reads (setting $y(0) = 1$)

$$\begin{aligned}y(t = n\cdot T) &= C(1+D+D^2+\ldots+D^{n-1}) + D^n = C\frac{1-D^n}{1-D} + D^n\\ &= \frac{1-\exp\left(-k_{3,\uparrow}T/2\right)}{1-\exp(-K_3T/2)}(1-\exp\left(-K_3nT/2\right)) + \exp\left(-K_3nT/2\right)\end{aligned} \tag{B.9}$$

This can be used to express the average value over the n-th period as

$$\begin{aligned}\langle y(n)\rangle =&\frac{1}{2} - \frac{1-\exp\left(-k_{3,\uparrow}T/2\right)}{2k_{3,\uparrow}T/2}\\ &+\left[\frac{1-\exp\left(-k_{3,\uparrow}T/2\right)}{1-\exp(-K_3T/2)}(1-\exp\left(-K_3nT/2\right)) + \exp\left(-K_3nT/2\right)\right]\\ &\cdot\left[\frac{1}{2k_{3,\downarrow}T/2}(1-\exp\left(-k_{3,\downarrow}T/2\right))\right.\\ &\left.+\exp\left(-k_{3,\downarrow}T/2\right)\frac{1}{2k_{3,\uparrow}T/2}(1-\exp\left(-k_{3,\uparrow}T/2\right))\right].\end{aligned} \tag{B.10}$$

In the long-time limit, one finds the plateau value

$$\begin{aligned}
\lim_{n\to\infty} y(t = n\cdot T) &= \frac{1}{2}\Bigg\{1 + \frac{1-\exp\left(-k_{3,\uparrow}T/2\right)}{1-\exp(-K_3T/2)}\frac{1}{k_{3,\downarrow}T/2}(1-\exp\left(-k_{3,\downarrow}T/2\right)) \\
&\quad - \frac{1-\exp\left(-k_{3,\uparrow}T/2\right)}{k_{3,\uparrow}T/2}\left(1 - \frac{1-\exp\left(-k_{3,\uparrow}T/2\right)}{1-\exp(-K_3T/2)}\exp\left(-k_{3,\downarrow}T/2\right)\right)\Bigg\} \\
&= \frac{1}{2}\Bigg\{1 + \frac{1-\exp\left(-k_{3,\uparrow}T/2\right)}{1-\exp(-K_3T/2)}\frac{1}{k_{3,\downarrow}T/2}(1-\exp\left(-k_{3,\downarrow}T/2\right)) \\
&\quad - \frac{1-\exp\left(-k_{3,\uparrow}T/2\right)}{k_{3,\uparrow}T/2}\frac{1-\exp\left(-k_{3,\downarrow}T/2\right)}{1-\exp(-K_3T/2)}\Bigg\} \\
&= \frac{1}{2}\Bigg\{1 + \frac{(1-\exp\left(-k_{3,\uparrow}T/2\right))(1-\exp\left(-k_{3,\downarrow}T/2\right)}{1-\exp(-K_3T/2)} \\
&\quad \cdot\left(\frac{1}{k_{3,\downarrow}T/2} - \frac{1}{k_{3,\uparrow}T/2}\right)\Bigg\} \equiv y_{plateau}.
\end{aligned} \tag{B.11}$$

For very fast switching this boils down to

$$y_{plateau} = \frac{k_{3,\uparrow}}{K_3} - \frac{k_{3,\uparrow}-k_{3,\downarrow}}{24K_3}k_{3,\downarrow}k_{3,\uparrow}(T/2)^2. \tag{B.12}$$

The general equation for $y(n)$ can be rewritten with $y_{plateau}$

$$\begin{aligned}
\langle y(n)\rangle &= y_{plateau} + \exp(-K_3nT/2)\left(1 - \frac{1-\exp\left(-k_{3,\uparrow}T/2\right)}{1-\exp(-K_3T/2)}\right) \\
&\quad \cdot\left[\frac{1}{2k_{3,\downarrow}T/2}(1-\exp\left(-k_{3,\downarrow}T/2\right)) + \exp\left(-k_{3,\downarrow}T/2\right)\frac{1}{2k_{3,\uparrow}T/2}(1-\exp\left(-k_{3,\uparrow}T/2\right))\right] \\
&\equiv y_{plateau} + \exp\left(-K(n+\frac{1}{2})T/2\right)\cdot\hat{y}_+
\end{aligned} \tag{B.13}$$

with

$$\begin{aligned}
\hat{y}_+ &= y\exp\left(\frac{K_3T}{4}\right)\frac{\exp\left(-k_{3,\uparrow}T/2\right) - \exp(-K_3T/2)}{1-\exp(-K_3T/2)} \\
&\quad \cdot\left[\frac{1}{k_{3,\downarrow}T}(1-\exp\left(-k_{3,\downarrow}T/2\right)) + \exp\left(-k_{3,\downarrow}T/2\right)\frac{1}{k_{3,\uparrow}T}(1-\exp\left(-k_{3,\uparrow}T/2\right))\right].
\end{aligned} \tag{B.14}$$

When starting from the state with lower wettability the calculation can be done analogously. For the average value, one ends up with

$$\langle y(n)\rangle = y_{plateau} - \exp\left(-K(n+\frac{1}{2})T/2\right)\cdot\hat{y}_-. \tag{B.15}$$

$\hat{y}_-$ is identical to $\hat{y}_+$ after exchange of $k_{3,\downarrow}$ with $k_{3,\uparrow}$.
For $k_{3,\downarrow} = k_{3,\uparrow} = k_3$ these expressions simplify to

$$\begin{aligned} y(n) &= \frac{1}{2} + \exp\left(-k_3(2n+1)T/2\right)\frac{1-\exp(-k_3T/2)}{1-\exp(-2k_3T/2)}\frac{1}{2k_3T/2} \\ &\quad + (1-\exp(-k_3T/2))(1+\exp(-k_3T/2)) \\ &= \frac{1}{2} + \exp(-k_3(2n+1)T/2)\frac{1}{2k_3T/2}(1-\exp(-k_3T/2)). \end{aligned} \tag{B.16}$$

BIBLIOGRAPHY

[1] O. Darrigol. *Worlds of flow: a history of hydrodynamics from the Bernoullis to Prandtl*. Oxford University Press, 2005. DOI: 10.1017\&S0022112006003764 (cit. on p. 1).

[2] C. Staddon. *Managing Europe's water resources: twenty-first century challenges*. Routledge, 2016. DOI: 10.4324/9781315593548 (cit. on p. 1).

[3] M. Bestehorn. *Hydrodynamik und Strukturbildung: Mit einer kurzen Einführung in die Kontinuumsmechanik*. Springer-Verlag, 2006. DOI: 10.1007/3-540-33797-0 (cit. on p. 1).

[4] L. Landau and E. Lifshitz. *Fluid mechanics: course of theoretical physics*. Pergamon Press, 1987. DOI: 10.1016/C2013-0-03799-1 (cit. on p. 1).

[5] J. Shalf. "The future of computing beyond Moore's law." In: *Philosophical Transactions of the Royal Society A* 378.2166 (2020), p. 20190061. DOI: 10.1098/rsta.2019.0061 (cit. on p. 1).

[6] B. J. Alder and T. E. Wainwright. "Studies in molecular dynamics. i. general method." In: *The Journal of Chemical Physics* 31.2 (1959), pp. 459–466. DOI: 10.1063/1.1730376 (cit. on p. 1).

[7] D. Frenkel, B. Smit and M. A. Ratner. *Understanding molecular simulation: from algorithms to applications*. Vol. 2. Academic press San Diego, 1996. DOI: 10.1063/1.881812 (cit. on p. 1).

[8] S. Chen and G. D. Doolen. "Lattice Boltzmann method for fluid flows." In: *Annual Review of Fluid Mechanics* 30.1 (1998), pp. 329–364. DOI: 10.1146/annurev.fluid.30.1.329 (cit. on p. 1).

[9] X. He and L.-S. Luo. "Theory of the lattice Boltzmann method: from the Boltzmann equation to the lattice Boltzmann equation." In: *Phys. Rev. E* 56 (6 1997), pp. 6811–6817. DOI: 10.1103/PhysRevE.56.6811 (cit. on p. 1).

[10] T. Hansson, C. Oostenbrink and W. F. van Gunsteren. "Molecular dynamics simulations." In: *Current opinion in structural biology* 12.2 (2002), pp. 190–196. DOI: 10.1016/S0959-440X(02)00308-1 (cit. on p. 1).

[11] C. C. Battaile. "The kinetic Monte Carlo method: foundation, implementation, and application." In: *Computer Methods in Applied Mechanics and Engineering* 197.41-42 (2008), pp. 3386–3398. DOI: 10.1016/j.cma.2008.03.010 (cit. on p. 1).

[12] H. F. Wu, K. A. Fichthorn and A. Borhan. "An atomistic-continuum hybrid scheme for numerical simulation of droplet spreading on a solid surface." In: *Heat and Mass Transfer* 50.3 (2014), pp. 351–361. DOI: 10.1007/s00231-013-1270-4 (cit. on pp. 2, 32, 87).

[13] C. Schelte, J. Javaloyes and S. V. Gurevich. "Functional mapping for passively mode-locked semiconductor lasers." In: *Optics Letters* 43.11 (2018), pp. 2535–2538. DOI: 10.1364/OL.43.002535 (cit. on pp. 2, 88).

[14] M. K. Chaudhury and G. M. Whitesides. "How to make water run uphill." In: *Science* 256.5063 (1992), pp. 1539–1541. DOI: 10.1126/science.256.5063.1539 (cit. on p. 2).

[15] K. Ichimura, S.-K. Oh and M. Nakagawa. "Light-driven motion of liquids on a photoresponsive surface." In: *Science* 288.5471 (2000), pp. 1624–1626. DOI: 10.1126/science.288.5471.1624 (cit. on pp. 2, 31).

[16] K. Ishihara, A. Okazaki, N. Negishi, I. Shinohara, T. Okano, K. Kataoka and Y. Sakurai. "Photo-induced change in wettability and binding ability of azoaromatic polymers." In: *Journal of Applied Polymer Science* 27.1 (1982), pp. 239–245. DOI: 10.1002/app.1982.070270125 (cit. on pp. 3, 31, 55).

[17] R. Rosario, D. Gust, M. Hayes, F. Jahnke, J. Springer and A. A. . Garcia. "Photon-modulated wettability changes on spiropyran-coated surfaces." In: *Langmuir* 18.21 (2002), pp. 8062–8069. DOI: 10.1021/la025963l (cit. on pp. 3, 31, 55).

[18] F. Zhu, S. Tan, M. K. Dhinakaran, J. Cheng and H. Li. "The light-driven macroscopic directional motion of a water droplet on an azobenzene-calix[4]arene modified surface." In: *Chem. Commun.* 56 (74 2020), pp. 10922–10925. DOI: 10.1039/D0CC00519C (cit. on pp. 3, 31).

[19] W. Jiang, G. Wang, Y. He, X. Wang, Y. An, Y. Song and L. Jiang. "Photo-switched wettability on an electrostatic self-assembly azobenzene monolayer." In: *Chem. Commun.* (28 2005), pp. 3550–3552. DOI: 10.1039/B504479K (cit. on pp. 3, 31).

[20] J. Groten, C. Bunte and J. Rühe. "Light-induced switching of surfaces at wetting transitions through photoisomerization of polymer monolayers." In: *Langmuir* 28.42 (2012). PMID: 22967018, pp. 15038–15046. DOI: 10.1021/la302764k (cit. on pp. 3, 31, 55).

[21] C. Honnigfort, R. A. Campbell, J. Droste, P. Gutfreund, M. R. Hansen, B. J. Ravoo and B. Braunschweig. "Unexpected monolayer-to-bilayer transition of arylazopyrazole surfactants facilitates superior photo-control of fluid interfaces and colloids." In:

Chemical science 11.8 (2020), pp. 2085–2092. DOI: doi.org/10.1039/C9SC05490A (cit. on p. 3).

[22] C. Honnigfort, L. Topp, N. García Rey, A. Heuer and B. Braunschweig. "Dynamic wetting of photoresponsive arylazopyrazole monolayers is controlled by the molecular kinetics of the monolayer." In: *Journal of the American Chemical Society* 144.9 (2022), pp. 4026–4038. DOI: 10.1021/jacs.1c12832 (cit. on p. 3).

[23] R. Wang, K. Hashimoto, A. Fujishima, M. Chikuni, E. Kojima, A. Kitamura, M. Shimohigoshi and T. Watanabe. "Light-induced amphiphilic surfaces." In: *Nature* 388.6641 (1997), pp. 431–432. DOI: 10.1038/41233 (cit. on pp. 3 sq., 31, 55).

[24] X. Feng, J. Zhai and L. Jiang. "The fabrication and switchable superhydrophobicity of TiO_2 nanorod films." In: *Angewandte Chemie International Edition* 44.32 (2005), pp. 5115–5118. DOI: https://doi.org/10.1002/anie.200501337 (cit. on pp. 3, 31, 55).

[25] R.-D. Sun, A. Nakajima, A. Fujishima, T. Watanabe and K. Hashimoto. "Photoinduced surface wettability conversion of zno and TiO_2 thin films." In: *The Journal of Physical Chemistry B* 105.10 (2001), pp. 1984–1990. DOI: 10.1021/jp002525j (cit. on pp. 3, 31, 55).

[26] M. Stieneker, L. Topp, S. V. Gurevich and A. Heuer. "Multiscale perspective on wetting on switchable substrates: mapping between microscopic and mesoscopic models." In: *Phys. Rev. Fluids* 8 (1 2023), p. 013902. DOI: 10.1103/PhysRevFluids.8.013902 (cit. on pp. 4, 12).

[27] T. Blake and J. Haynes. "Kinetics of liquidliquid displacement." In: *Journal of Colloid and Interface Science* 30.3 (1969), pp. 421–423. DOI: 10.1016/0021-9797(69)90411-1 (cit. on pp. 5, 55, 58).

[28] C. Honisch, T.-S. Lin, A. Heuer, U. Thiele and S. V. Gurevich. "Instabilities of layers of deposited molecules on chemically stripe patterned substrates: ridges versus drops." In: *Langmuir* 31.38 (2015), pp. 10618–10631. DOI: 10.1021/acs.langmuir.5b02407 (cit. on pp. 7–10, 12, 33, 53).

[29] W. Tewes, O. Buller, A. Heuer, U. Thiele and S. V. Gurevich. "Comparing kinetic Monte Carlo and thin-film modeling of transversal instabilities of ridges on patterned substrates." In: *The Journal of Chemical Physics* 146.9 (2017), p. 094704. DOI: 10.1063/1.4977739 (cit. on pp. 7–10, 32, 53).

[30] A. Oron, S. H. Davis and S. G. Bankoff. "Long-scale evolution of thin liquid films." In: *Reviews of Modern Physics* 69.3 (1997), pp. 931–980. DOI: 10.1103/RevModPhys.69.931 (cit. on pp. 7 sq., 11, 32, 40).

[31] S. Engelnkemper. "Nichtlineare Analyse physikochemisch getriebener Entnetzung - Statik und Dynamik." PhD thesis. Westfälische Wilhelms-Universität Münster, 2017 (cit. on pp. 7, 9, 13).

[32] U. Thiele. "Recent advances in and future challenges for mesoscopic hydrodynamic modelling of complex wetting." In: *Colloids and Surfaces A: Physicochemical and Engineering Aspects* 553 (2018), pp. 487–495. DOI: 10.1016/j.colsurfa.2018.05.049 (cit. on pp. 7, 10 sqq.).

[33] X. Xu, U. Thiele and T. Qian. "A variational approach to thin film hydrodynamics of binary mixtures." In: *Journal of Physics: Condensed Matter* 27 (2015), p. 085005. DOI: 10.1088/0953-8984/27/8/085005 (cit. on p. 7).

[34] D. Bonn, J. Eggers, J. Indekeu, J. Meunier and E. Rolley. "Wetting and spreading." In: *Reviews of Modern Physics* 81 (2 2009), pp. 739–805. DOI: 10.1103/RevModPhys.81.739 (cit. on pp. 7 sqq., 32 sq., 35, 40).

[35] U. Thiele. "Patterned deposition at moving contact lines." In: *Advances in colloid and interface science* 206 (2014), pp. 399–413. DOI: 10.1016/j.cis.2013.11.002 (cit. on p. 7).

[36] V. S. Mitlin. "Dewetting of solid surface: analogy with spinodal decomposition." In: *Journal of Colloid and Interface Science* 156.2 (1993), pp. 491–497. DOI: https://doi.org/10.1006/jcis.1993.1142 (cit. on p. 7).

[37] B. Derjaguin and M. Kussakov. "An experimental investigation of polymolecular solvate (adsorbed) films as applied to the development of a mathematical theory of the stability of colloids." In: *Progress in Surface Science* 40.1-4 (1992), pp. 26–45. DOI: 10.1016/0079-6816(92)90031-C (cit. on p. 8).

[38] B. Derjaguin. "Ultramikrometrische Untersuchungen der Solvathüllen und des "elementaren" Quellungsaktes." In: *Progress in Surface Science* 40.1-4 (1992), pp. 16–21. DOI: 10.1016/0079-6816(92)90028-G (cit. on p. 8).

[39] B. Derjaguin. "Untersuchungen des Spaltdruckes dünner Filme, deren Entwicklung, Ergebnisse und zu lösende aktuelle Probleme." In: *Colloid and Polymer Science* 253.6 (1975), pp. 492–499. DOI: 10.1007/BF01491828 (cit. on p. 8).

[40] J. N. Israelachvili. *Intermolecular and surface forces*. Academic press, 2011. DOI: 10.1016/C2011-0-05119-0 (cit. on p. 8).

[41] F. L. Leite, C. C. Bueno, A. L. Da Róz, E. C. Ziemath and O. N. Oliveira. "Theoretical models for surface forces and adhesion and their measurement using atomic force microscopy." In: *International Journal of Molecular Sciences* 13.10 (2012), pp. 12773–12856. DOI: 10.3390/ijms131012773 (cit. on p. 8).

[42] A. Oron and S. G. Bankoff. "Dynamics of a condensing liquid film under conjoining/disjoining pressures." In: *Physics of Fluids* 13.5 (2001), pp. 1107–1117. DOI: 10.1063/1.1355022 (cit. on p. 8).

[43] L. M. Pismen and U. Thiele. "Asymptotic theory for a moving droplet driven by a wettability gradient." In: *Physics of Fluids* 18.4 (2006), p. 042104. DOI: 10.1063/1.2191015 (cit. on p. 8).

[44] V. S. Mitlin and N. V. Petviashvili. "Nonlinear dynamics of dewetting: kinetically stable structures." In: *Physics Letters A* 192.5-6 (1994), pp. 323–326. DOI: 10.1016/0375-9601(94)90213-5 (cit. on p. 8).

[45] K. Kargupta and A. Sharma. "Creation of ordered patterns by dewetting of thin films on homogeneous and heterogeneous substrates." In: *Journal of colloid and interface science* 245.1 (2002), pp. 99–115. DOI: 10.1006/jcis.2001.7860 (cit. on p. 8).

[46] U. Thiele and E. Knobloch. "On the depinning of a driven drop on a heterogeneous substrate." In: *New Journal of Physics* 8.12 (2006), p. 313. DOI: 10.1088/1367-2630/8/12/313 (cit. on pp. 8 sq.).

[47] M. Wilczek, J. Zhu, L. Chi, U. Thiele and S. V. Gurevich. "Dip-coating with prestructured substrates: transfer of simple liquids and Langmuir-Blodgett monolayers." In: *J. Phys. Condens. Matter* 29.1 (2016), p. 014002. DOI: 10.1088/0953-8984/29/1/014002 (cit. on pp. 8, 10).

[48] U. Thiele and S. Hartmann. "Gradient dynamics model for drops spreading on polymer brushes." In: *The European Physical Journal Special Topics* 229.10 (2020), pp. 1819–1832. DOI: 10.1140/epjst/e2020-900231-2 (cit. on p. 8).

[49] C. Huh and L. E. Scriven. "Hydrodynamic model of steady movement of a solid/liquid/fluid contact line." In: *Journal of colloid and interface science* 35.1 (1971), pp. 85–101. DOI: 10.1016/0021-9797(71)90188-3 (cit. on p. 9).

[50] H. P. Kavehpour, B. Ovryn and G. H. McKinley. "Microscopic and macroscopic structure of the precursor layer in spreading viscous drops." In: *Physical review letters* 91.19 (2003), p. 196104. DOI: 10.1103/PhysRevLett.91.196104 (cit. on p. 9).

[51] R. Bruinsma. "Slow spreading of polymer melts." In: *Macromolecules* 23.1 (1990), pp. 276–280. DOI: 10.1021/ma00203a047 (cit. on p. 9).

[52] P. Bahadur, P. S. Yadav, K. Chaurasia, A. Leh and R. Tadmor. "Chasing drops: following escaper and pursuer drop couple system." In: *Journal of colloid and interface science* 332.2 (2009), pp. 455–460. DOI: 10.1016/j.jcis.2008.12.050 (cit. on p. 9).

[53] F. Heslot, N. Fraysse and A. Cazabat. "Molecular layering in the spreading of wetting liquid drops." In: *Nature* 338.6217 (1989), pp. 640–642. DOI: 10.1038/338640a0 (cit. on p. 9).

[54] K. B. Glasner and T. P. Witelski. "Coarsening dynamics of dewetting films." In: *Physical review E* 67.1 (2003), p. 016302. DOI: 10.1103/PhysRevE.67.016302 (cit. on p. 9).

[55] R. Konnur, K. Kargupta and A. Sharma. "Instability and morphology of thin liquid films on chemically heterogeneous substrates." In: *Physical Review Letters* 84.5 (2000), p. 931. DOI: 10.1103/PhysRevLett.84.931 (cit. on pp. 9 sq.).

[56] S. Mechkov, M. Rauscher and S. Dietrich. "Stability of liquid ridges on chemical micro-and nanostripes." In: *Physical Review E* 77.6 (2008), p. 061605. DOI: 10.1103/PhysRevE.77.061605 (cit. on p. 10).

[57] S. Engelnkemper, S. V. Gurevich, H. Uecker, D. Wetzel and U. Thiele. "Continuation for thin film hydrodynamics and related scalar problems." In: *Computational modelling of bifurcations and instabilities in fluid dynamics*. Springer, 2019, pp. 459–501. DOI: 10.1007/978-3-319-91494-7_13 (cit. on pp. 10, 17).

[58] N. Tretyakov, M. Müller, D. Todorova and U. Thiele. "Parameter passing between molecular dynamics and continuum models for droplets on solid substrates: the static case." In: *The Journal of Chemical Physics* 138.6 (2013), p. 064905. DOI: 10.1063/1.4790581 (cit. on pp. 10, 35, 53, 88).

[59] A. P. Hughes, U. Thiele and A. J. Archer. "Liquid drops on a surface: using density functional theory to calculate the binding potential and drop profiles and comparing with results from mesoscopic modelling." In: *The Journal of Chemical Physics* 142.7 (2015), p. 074702. DOI: 10.1063/1.4907732 (cit. on pp. 10, 35, 53, 88).

[60] A. P. Hughes, U. Thiele and A. J. Archer. "Influence of the fluid structure on the binding potential: comparing liquid drop profiles from density functional theory with results from mesoscopic theory." In: *The Journal of Chemical Physics* 146.6 (2017), p. 064705. DOI: 10.1063/1.4974832 (cit. on pp. 10, 35, 53, 88).

[61] O. Buller, W. Tewes, A. J. Archer, A. Heuer, U. Thiele and S. V. Gurevich. "Nudged elastic band calculation of the binding potential for liquids at interfaces." In: *The Journal of Chemical Physics* 147.2 (2017), p. 024701. DOI: 10.1063/1.4990702 (cit. on pp. 10, 35, 53, 88).

[62] A. Münch, B. Wagner and T. P. Witelski. "Lubrication models with small to large slip lengths." In: *Journal of Engineering Mathematics* 53.3-4 (2005), pp. 359–383. DOI: 10.1007/s10665-005-9020-3 (cit. on p. 11).

[63] H. Yin, D. N. Sibley, U. Thiele, A. J. Archer et al. "Films, layers, and droplets: the effect of near-wall fluid structure on spreading dynamics." In: *Physical Review E* 95.2 (2017), p. 023104. DOI: 10.1103/PhysRevE.95.023104 (cit. on p. 12).

[64] N. Savva and S. Kalliadasis. "Dynamics of moving contact lines: a comparison between slip and precursor film models." In: *EPL (Europhysics Letters)* 94.6 (2011), p. 64004. DOI: 10.1209/0295-5075/94/64004 (cit. on p. 12).

[65] B. Davidovitch, E. Moro and H. A. Stone. "Spreading of viscous fluid drops on a solid substrate assisted by thermal fluctuations." In: *Physical review letters* 95.24 (2005), p. 244505. DOI: 10.1103/PhysRevLett.95.244505 (cit. on pp. 12, 33 sq., 88).

[66] R. Fetzer, M. Rauscher, R. Seemann, K. Jacobs and K. Mecke. "Thermal noise influences fluid flow in thin films during spinodal dewetting." In: *Physical Review Letters* 99.11 (2007), p. 114503. DOI: 10.1103/PhysRevLett.99.114503 (cit. on p. 12).

[67] G. Grün, K. Mecke and M. Rauscher. "Thin-film flow influenced by thermal noise." In: *Journal of Statistical Physics* 122.6 (2006), pp. 1261–1291. DOI: 10.1007/s10955-006-9028-8 (cit. on p. 12).

[68] J. A. Anderson, J. Glaser and S. C. Glotzer. "HOOMD-blue: a Python package for high-performance molecular dynamics and hard particle Monte Carlo simulations." In: *Computational Materials Science* 173 (2020), p. 109363. DOI: 10.1016/j.commatsci.2019.109363 (cit. on p. 14).

[69] P. J. Hoogerbrugge and J. M. V. A. Koelman. "Simulating microscopic hydrodynamic phenomena with dissipative particle dynamics." In: *Europhysics Letters (EPL)* 19.3 (1992), pp. 155–160. DOI: 10.1209/0295-5075/19/3/001 (cit. on p. 14).

[70] C. L. Phillips, J. A. Anderson and S. C. Glotzer. "Pseudo-random number generation for Brownian dynamics and dissipative particle dynamics simulations on GPU devices." In: *Journal of Computational Physics* 230.19 (2011), pp. 7191–7201. DOI: https://doi.org/10.1016/j.jcp.2011.05.021 (cit. on p. 14).

[71] T. Ingebrigtsen and S. Toxvaerd. "Contact angles of Lennard-Jones liquids and droplets on planar surfaces." In: *The Journal of Physical Chemistry C* 111.24 (2007), pp. 8518–8523. DOI: 10.1021/jp0676235 (cit. on pp. 14, 16, 56).

[72] J. H. Weijs, A. Marchand, B. Andreotti, D. Lohse and J. H. Snoeijer. "Origin of line tension for a Lennard-Jones nanodroplet." In: *Physics of Fluids* 23.2 (2011), p. 022001. DOI: 10.1063/1.3546008 (cit. on pp. 14, 56).

[73] M. Kanduč. "Going beyond the standard line tension: size-dependent contact angles of water nanodroplets." In: *The Journal of Chemical Physics* 147.17 (2017), p. 174701. DOI: 10.1063/1.4990741 (cit. on pp. 14, 56).

[74] J. Walton, D. Tildesley, J. Rowlinson and J. Henderson. "The pressure tensor at the planar surface of a liquid." In: *Molecular Physics* 48.6 (1983), pp. 1357–1368. DOI: 10.1080/00268978300100971 (cit. on p. 16).

[75] M. S. Green. "Markoff random processes and the statistical mechanics of time-dependent phenomena. ii. irreversible processes in fluids." In: *The Journal of Chemical Physics* 22.3 (1954), pp. 398–413. DOI: 10.1063/1.1740082 (cit. on p. 16).

[76] R. Kubo. "Statistical-mechanical theory of irreversible processes. i. general theory and simple applications to magnetic and conduction problems." In: *Journal of the Physical Society of Japan* 12.6 (1957), pp. 570–586. DOI: 10.1143/JPSJ.12.570 (cit. on p. 16).

[77] V. G. Baidakov, S. P. Protsenko and Z. R. Kozlova. "Metastable Lennard-Jones fluids. i. shear viscosity." In: *The Journal of Chemical Physics* 137.16 (2012), p. 164507. DOI: 10.1063/1.4758806 (cit. on p. 16).

[78] M. Heil and A. L. Hazel. "oomph-lib - an object-oriented multiphysics finite-element library." In: *Fluid-Structure Interaction*. Ed. by H.-J. Bungartz and M. Schäfer. Berlin, Heidelberg: Springer Berlin Heidelberg, 2006, pp. 19–49. DOI: 10.1007/3-540-34596-5_2 (cit. on pp. 17, 25, 27).

[79] J. Suer, M. Stieneker, S. Gurevich and S. Hartmann. *Implementation of the thin-film equation on prestructured, switchable substrates using the oomph-lib library*. 2022. DOI: 10.5281/zenodo.5821537 (cit. on pp. 17, 94).

[80] J. Grawitter and H. Stark. "Steering droplets on substrates using moving steps in wettability." In: *Soft Matter* 17.9 (2021), pp. 2454–2467. DOI: 10.1039/D0SM02082F (cit. on pp. 17, 31 sq., 53).

[81] H. Uecker, D. Wetzel and J. Rademacher. "Pde2path - a MATLAB package for continuation and bifurcation in 2d elliptic systems." In: *Numerical Mathematics: Theory, Methods and Applications* 7 (2014), pp. 56–106. DOI: 10.4208/nmtma.2014.1231nm (cit. on p. 17).

[82] L. Ophaus, E. Knobloch, S. V. Gurevich and U. Thiele. "Two-dimensional localized states in an active phase-field-crystal model." In: *Phys. Rev. E* 103 (3 2021), p. 032601. DOI: 10.1103/PhysRevE.103.032601 (cit. on p. 17).

[83] T. Frohoff-Hülsmann, J. Wrembel and U. Thiele. "Suppression of coarsening and emergence of oscillatory behavior in a Cahn-Hilliard model with nonvariational coupling." In: *Phys. Rev. E* 103 (4 2021), p. 042602. DOI: 10.1103/PhysRevE.103.042602 (cit. on p. 17).

[84] P.-M. T. Ly, U. Thiele, L. Chi and S. V. Gurevich. "Effects of time-periodic forcing in a Cahn-Hilliard model for Langmuir-Blodgett transfer." In: *Phys. Rev. E* 99 (6 2019), p. 062212. DOI: 10.1103/PhysRevE.99.062212 (cit. on p. 17).

[85] M. Stieneker and S. V. Gurevich. *Periodic orbit continuation in systems with external periodic forcing using pde2path*. 2022. DOI: 10.5281/zenodo.7071447 (cit. on pp. 17, 27, 30).

[86] MATLAB. *MATLAB version 9.10.0.1613233 (r2021a)*. Natick, Massachusetts: The MathWorks Inc., 2021 (cit. on p. 17).

[87] M. Stieneker, S. Hartmann and S. Gurevich. *An oomph-lib interface to access pde2path problem structs*. 2021. DOI: 10.5281/zenodo.5810147 (cit. on p. 17).

[88] B. Klein. *FEM: Grundlagen und Anwendungen der Finite-Element-Methode im Maschinen- und Fahrzeugbau*. Springer, 2010. DOI: 10.1007/978-3-322-91910-6 (cit. on p. 18).

[89] A. Logg, K.-A. Mardal and G. Wells. *Automated solution of differential equations by the finite element method: the FEniCS book*. Vol. 84. Springer Science & Business Media, 2012. DOI: 10.1007/978-3-642-23099-8 (cit. on p. 18).

[90] E. B. Becker, G. F. Carey and J. T. Oden. *Finite elements: an introduction*. Vol. 1. Prentice Hall, 1981. DOI: 10.1115/1.3162562 (cit. on p. 18).

[91] W. Hackbusch. *Theorie und Numerik elliptischer Differentialgleichungen*. Springer, 1986. DOI: 10.1007/978-3-322-99946-7 (cit. on pp. 18 sq., 23, 25 sq.).

[92] D. Braess. *Finite Elemente - Theorie, schnelle Löser und Anwendungen in der Elastizitätstheorie*. Springer Berlin Heidelberg, 2007. DOI: 10.1007/978-3-662-07233-2 (cit. on pp. 18 sq., 22, 24, 26).

[93] J. P. Boyd. *Chebyshev and Fourier spectral methods*. Courier Corporation, 2001 (cit. on pp. 18 sq., 21 sq.).

[94] K. W. Morton and D. F. Mayers. *Numerical solution of partial differential equations: an introduction*. Cambridge university press, 2005. DOI: 10.1017/CBO9780511812248 (cit. on p. 22).

[95] T. M. Squires and S. R. Quake. "Microfluidics: fluid physics at the nanoliter scale." In: *Rev. Mod. Phys.* 77 (3 2005), pp. 977–1026. DOI: 10.1103/RevModPhys.77.977 (cit. on p. 32).

[96] M. P. Allen and D. J. Tildesley. *Computer simulation of liquids: second edition*. 2nd ed. Oxford: Oxford University Press, 2017, p. 640. DOI: 10.1093/oso/9780198803195.001.0001 (cit. on p. 32).

[97] M. J. de Ruijter, T. D. Blake and J. De Coninck. "Dynamic wetting studied by molecular modeling simulations of droplet spreading." In: *Langmuir* 15.22 (1999), pp. 7836–7847. DOI: 10.1021/la990171l (cit. on pp. 32, 55, 68, 85).

[98] J. Roy Choudhuri and P. Nath. "Wetting transition of a nanodrop on switchable hydrophilic-hydrophobic surfaces." In: *Surfaces and Interfaces* 21 (2020), p. 100628. DOI: 10.1016/j.surfin.2020.100628 (cit. on p. 32).

[99] U. Thiele. "Thin film evolution equations from (evaporating) dewetting liquid layers to epitaxial growth." In: *Journal of Physics: Condensed Matter* 22.8 (2010), p. 084019. DOI: 10.1088/0953-8984/22/8/084019 (cit. on p. 32).

[100] J. Zhang, M. K. Borg and J. M. Reese. "Multiscale simulation of dynamic wetting." In: *International Journal of Heat and Mass Transfer* 115 (2017), pp. 886–896. DOI: 10.1016/j.ijheatmasstransfer.2017.07.034 (cit. on p. 32).

[101] N. G. Hadjiconstantinou. "Combining atomistic and continuum simulations of contact-line motion." In: *Phys. Rev. E* 59 (2 1999), pp. 2475–2478. DOI: 10.1103/PhysRevE.59.2475 (cit. on p. 32).

[102] S. Seabold and J. Perktold. "statsmodels: econometric and statistical modeling with Python." In: *9th Python in Science Conference*. 2010. DOI: 10.25080/majora-92bf1922-011 (cit. on p. 34).

[103] D. E. Sullivan. "Surface tension and contact angle of a liquid–solid interface." In: *The Journal of Chemical Physics* 74.4 (1981), pp. 2604–2615. DOI: 10.1063/1.441333 (cit. on p. 35).

[104] R. Pandit, M. Schick and M. Wortis. "Systematics of multilayer adsorption phenomena on attractive substrates." In: *Phys. Rev. B* 26 (9 1982), pp. 5112–5140. DOI: 10.1103/PhysRevB.26.5112 (cit. on p. 35).

[105] E. H. Hauge and M. Schick. "Continuous and first-order wetting transition from the van der Waals theory of fluids." In: *Phys. Rev. B* 27 (7 1983), pp. 4288–4301. DOI: 10.1103/PhysRevB.27.4288 (cit. on p. 35).

[106] S. Dietrich and M. Schick. "Critical wetting of surfaces in systems with long-range forces." In: *Phys. Rev. B* 31 (7 1985), pp. 4718–4720. DOI: 10.1103/PhysRevB.31.4718 (cit. on p. 35).

[107] S. Dietrich and M. Schick. "Order of wetting transitions." In: *Phys. Rev. B* 33 (7 1986), pp. 4952–4968. DOI: 10.1103/PhysRevB.33.4952 (cit. on p. 35).

[108] N. Kubochkin and T. Gambaryan-Roisman. "Wetting at nanoscale: effect of surface forces and droplet size." In: *Phys. Rev. Fluids* 6 (9 2021), p. 093603. DOI: 10.1103/PhysRevFluids.6.093603 (cit. on pp. 35, 57).

[109] M. Müller and L. G. MacDowell. "Wetting of polymer liquids: Monte Carlo simulations and self-consistent field calculations." In: *Journal of Physics: Condensed Matter* 15.19 (2003), R609–R653. DOI: 10.1088/0953-8984/15/19/201 (cit. on pp. 53, 88).

[110] V. P. Carey and A. P. Wemhoff. "Disjoining pressure effects in ultra-thin liquid films in micropassages—comparison of thermodynamic theory with predictions of molecular dynamics simulations." In: *Journal of Heat Transfer* 128.12 (2006), pp. 1276–1284. DOI: 10.1115/1.2349504 (cit. on pp. 53, 88).

[111] L. MacDowell. "Computer simulation of interface potentials: towards a first principle description of complex interfaces?" In: *The European Physical Journal Special Topics* 197.1 (2011), pp. 131–145. DOI: 10.1140/epjst/e2011-01447-6 (cit. on pp. 53, 88).

[112] D. N. Sibley, P. Llombart, E. G. Noya, A. J. Archer and L. G. MacDowell. "How ice grows from premelting films and water droplets." In: *Nature communications* 12.239 (2021), pp. 1–11. DOI: 10.1038/s41467-020-20318-6 (cit. on pp. 53, 88).

[113] V. Samsonov. "On computer simulation of droplet spreading." In: *Current opinion in colloid & interface science* 16.4 (2011), pp. 303–309. DOI: 10.1016/j.cocis.2011.03.004 (cit. on p. 55).

[114] M. Voué and J. De Coninck. "Spreading and wetting at the microscopic scale: recent developments and perspectives." In: *Acta materialia* 48.18-19 (2000), pp. 4405–4417. DOI: 10.1016/S1359-6454(00)00227-5 (cit. on p. 55).

[115] R. Vellingiri, N. Savva and S. Kalliadasis. "Droplet spreading on chemically heterogeneous substrates." In: *Phys. Rev. E* 84 (3 2011), p. 036305. DOI: 10.1103/PhysRevE.84.036305 (cit. on p. 55).

[116] A. Clarke, T. Blake, K. Carruthers and A. Woodward. "Spreading and imbibition of liquid droplets on porous surfaces." In: *Langmuir* 18.8 (2002), pp. 2980–2984. DOI: 10.1021/la0117810 (cit. on p. 55).

[117] J. Eggers, J. R. Lister and H. A. Stone. "Coalescence of liquid drops." In: *Journal of Fluid Mechanics* 401 (1999), pp. 293–310. DOI: 10.1017/S002211209900662X (cit. on p. 55).

[118] Y. Liao and D. Lucas. "A literature review on mechanisms and models for the coalescence process of fluid particles." In: *Chemical Engineering Science* 65.10 (2010), pp. 2851–2864. DOI: 10.1016/j.ces.2010.02.020 (cit. on p. 55).

[119] D. Seveno, A. Vaillant, R. Rioboo, H. Adão, J. Conti and J. De Coninck. "Dynamics of wetting revisited." In: *Langmuir* 25.22 (2009). PMID: 19845346, pp. 13034–13044. DOI: 10.1021/la901125a (cit. on p. 55).

[120] D. Duvivier, T. D. Blake and J. De Coninck. "Toward a predictive theory of wetting dynamics." In: *Langmuir* 29.32 (2013). PMID: 23844877, pp. 10132–10140. DOI: 10.1021/la4017917 (cit. on p. 55).

[121] Y. Rotenberg, L. Boruvka and A. Neumann. "Determination of surface tension and contact angle from the shapes of axisymmetric fluid interfaces." In: *Journal of Colloid and Interface Science* 93.1 (1983), pp. 169–183. DOI: 10.1016/0021-9797(83)90396-X (cit. on p. 57).

[122] D. Kwok and A. Neumann. "Contact angle measurement and contact angle interpretation." In: *Advances in Colloid and Interface Science* 81.3 (1999), pp. 167–249. DOI: 10.1016/S0001-8686(98)00087-6 (cit. on p. 57).

[123] P. Petrov and I. Petrov. "A combined molecular-hydrodynamic approach to wetting kinetics." In: *Langmuir* 8.7 (1992), pp. 1762–1767. DOI: 10.1021/la00043a013 (cit. on p. 58).

[124] P. Gaskell, P. Jimack, M. Sellier, H. Thompson and M. Wilson. "Gravity-driven flow of continuous thin liquid films on non-porous substrates with topography." In: *Journal of Fluid Mechanics* 509 (2004), pp. 253–280. DOI: 10.1017/S0022112004009425 (cit. on p. 89).

[125] M. Baker. "1500 scientists lift the lid on reproducibility." In: *Nature* 533.26 (2016), pp. 353–66. DOI: 10.1038/533452a (cit. on p. 93).